

Light-Shining-through-a-Wall

Searching for Axion-Like Particles with
the OSQAR and ALPS II experiment

Dissertation

zur Erlangung des Grades
„Doktor der Naturwissenschaften“



JOHANNES GUTENBERG
UNIVERSITÄT MAINZ

Fachbereich Physik, Mathematik und Informatik

Christoph Weinsheimer
geboren in Mainz

Mainz im August 2017

1. **Berichterstatter:** [REDACTED]
2. **Berichterstatter:** [REDACTED]

Tag der Verteidigung: 08. Dez. 2017

Ich versichere, dass ich die vorliegende Arbeit selbstständig verfasst und keine anderen als die angegebenen Quellen und Hilfsmittel benutzt, sowie Zitate kenntlich gemacht habe.

Mainz, 2017

Dipl. Phys. Christoph Weinsheimer
ETAP
Institut für Physik
Staudingerweg 7
Johannes Gutenberg-Universität
D-55099 Mainz
weinshec@students.uni-mainz.de

Zusammenfassung

Die Existenz Axion-ähnlicher Teilchen (ALPs) wird von zahlreichen Erweiterungen des Standard Modells der Teilchenphysik vorhergesagt. Abhängig von den exakten Eigenschaften dieser Teilchen, können sie dazu beitragen bisher ungelöste Fragen der Physik zu beantworten, wie etwa die des Wesens Dunkler Materie oder den ungeklärten Kühlungsmechanismen stellarer Systeme. Aufgrund ihrer sehr seltenen Interaktion und ihrer geringen Masse könnten sich ALPs bisher der experimentellen Beobachtung entzogen haben.

Die vorliegende Arbeit beschreibt die Suche nach ALPs mit dem OSQAR und ALPS II Experiment, die beide mithilfe des Light-Shining-through-a-Wall Prinzips eine Modell unabhängige Suche nach ALPs ermöglichen und dabei große Bereiche des Parameter-Raumes untersuchen können. Als Ergebnis konnten keine Hinweise auf ALPs mit den OSQAR Experiment beobachtet werden, weshalb entsprechende Ausschlussgrenzen auf die ALP-Photon Kopplungskonstante

$$g_{a\gamma\gamma}^{\text{scalar}} < 3.2 \cdot 10^{-8} \text{ GeV}^{-1} \quad g_{a\gamma\gamma}^{\text{pseudos.}} < 3.5 \cdot 10^{-8} \text{ GeV}^{-1}$$

für skalare bzw. pseudoskalare ALPs mit Massen kleiner als $2 \cdot 10^{-4}$ eV abgeleitet wurden. Dieses Ergebnis stellt zur Zeit die stärksten Ausschlussgrenzen laborbasierter ALP-Suchen dar. Darüberhinaus präsentiert diese Arbeit die Beiträge zum ALPS II Experiment, welches sich derzeit im Aufbau befindet. Dazu gehört die Entwicklung einer effizienten optischen Schnittstelle zwischen Detektor und Experiment, eines performanten Datennahme- und Kontroll-Systems, sowie die Implementierung von Analyse und Simulations-Software.

Abstract

The existence of Axion-Like Particles (ALPs) is predicted by many extensions the Standard Model of particle physics. Depending on their particular properties, these particles might contribute to several so far unresolved questions of physics, such as the nature of dark matter or the anomalous cooling processes observed in stellar systems. Being both very weakly interacting and ultra light, ALPs might have evaded experimental observation so far.

This thesis describes the search for ALPs with the OSQAR and ALPS II experiment, both implementing the Light-Shining-through-a-Wall technique allowing for a generic model independent search probing a large range of the ALP parameter space. As a result, no evidence of ALPs has been observed with the OSQAR experiment, hence the following exclusion limits on the ALP-photon coupling were derived

$$g_{a\gamma\gamma}^{\text{scalar}} < 3.2 \cdot 10^{-8} \text{ GeV}^{-1} \quad g_{a\gamma\gamma}^{\text{pseudos.}} < 3.5 \cdot 10^{-8} \text{ GeV}^{-1}$$

for scalar and pseudoscalar ALPs of masses below $2 \cdot 10^{-4}$ eV. These limits represent the most the stringent laboratory based constraints today. Further this work presents the contributions to the ALPS II experiment being currently commissioned. This includes the development of an efficient optical coupling of the detector to the experiment, a performant data acquisition and control system, and finally an extensible data analysis and simulation framework.

Contents

I	Introduction	1
1	Theory of hidden-sector lightweights	3
1.1	Standard Model of particle physics	4
1.2	Axions and Axion-Like Particles	9
2	Experimental searches	11
2.1	The Light Shining through a Wall principle	12
2.2	Helioscopes	14
2.3	Vacuum Magnetic Birefringence searches	15
2.4	Haloscopes	16
2.5	Astrophysical observations	16
2.6	LSW type compared to others	17
2.7	The ALPlot	18
3	Overview of this work	19
II	OSQAR Experiment	21
4	Description of the OSQAR experiment	23
4.1	Magnet system	23
4.2	Laser and photon detector	25
4.3	Data taking and preparation	25
5	Searching for ALPs with OSQAR	27
5.1	Data processing	27
5.2	Setting ALP exclusion limits	32
6	Results and prospects	37
III	ALPS II Experiment	39
7	From ALPS I to ALPS II	41
7.1	General overview	41
7.2	Transition Edge Sensor	47

8	Signal photon coupling	53
8.1	Gaussian beam theory	53
8.2	Beam parameter measurement and the Knife-Edge method	56
8.3	Free-Space-To-Fiber-Coupling setup	61
8.4	Performance and stability	64
9	Implementing a slow control and DAQ system	65
9.1	A slow control system for ALPS II	65
9.2	Fast DAQ system for the ALPS detector	77
10	The FAST framework	85
10.1	Spectrum tools	86
10.2	Simulation	89
10.3	Analysis	93
11	Results and prospects	103
IV	Summary	105
12	Conclusion and outlook	107
	Appendix	111
A	Heterodyne detection	111
B	DS18B20 calibration coefficients	112
C	Finite differences	113
D	DFT reference sample code	115
E	Peakfinding noise reference	116
	Acronyms	120
	List of Figures	123
	List of Tables	124
	Bibliography	125

To ██████████

Part I

Introduction

1

Theory of hidden-sector lightweights

I like to imagine that God has a giant computer-controlled factory, which takes Lagrangians as input and delivers the universe they represent as output. [...] occasionally it returns an error message: “this Lagrangian does not describe a possible universe; please check for syntax errors or incorrect signs”

DAVID GRIFFITHS

The goal of elementary particle physics is to describe the universe and all its content at the most fundamental level. Exploring nature’s irreducible ingredients and combining those in a holistic description of their dynamics and interactions has led to one of the most successful and best understood theories in physics — the Standard Model (SM) of particle physics. However, despite all achievements, there are clear indications that the SM is not yet complete, therefore demanding Beyond Standard Model (BSM) extensions.

This chapter gives a brief introduction to the basic principles of the SM starting with a phenomenological overview in Sec. 1.1.1 and a more detailed description in Sec. 1.1.2 using the framework of Quantum Field Theories (QFTs) and the mathematical beauty of symmetries. Section 1.1.3 then illustrates some of the mentioned shortcomings of the SM before Sec. 1.2 introduces a particularly neat BSM extension, laying the theoretical ground for this thesis.

If not explicitly indicated otherwise, the system of *natural units* ($\hbar = c = 1$) is used here and throughout this thesis, conventionally quoting masses and energies in terms of eV.

1.1 | Standard Model of particle physics

The SM is the theory of all elementary particles and their interactions. It distinguishes *fermions*, the constituents of matter, from *bosons* mediating the interactions between them. Although today we know about four of these, namely the electromagnetic, the weak, the strong and the gravitational interaction, the SM incorporates only the first three of them. However, beginning with the unification of the electromagnetic and weak interactions by Glashow, Weinberg and Salam [1, 2, 3] at the beginning of the second half of the last century, the SM started its triumphal march towards one of the most successful theories of modern physics.

1.1.1 | Overview

The classification of elementary particles into fermions and bosons mentioned above is founded on their spin quantum number — while fermions carry half-integer valued spin, bosons carry integer spin numbers. The group of fermions can be further divided into quarks and leptons, each of them coming in three generations. The first generation of leptons contains the *electron* (e) and the *electron neutrino* (ν_e), whereas the first quark generation is comprised of the *up* (u) and *down* (d) quark. The second and third generations respectively embody heavier siblings of these particles. There is the *charm* (c) and *strange* (s) quark as well as the *top* (t) and *bottom* (b) quark with the former being the heaviest elementary particle known today with a mass of $m_t = (173.2 \pm 0.51 \pm 0.71) \text{ GeV}$ [4]. While on the lepton side one finds the *muon* (μ) and the *muon neutrino* (ν_μ) next to the *tau* (τ) and the *tau neutrino* (ν_τ). In contrast to the huge mass of top quark the neutrinos mark the opposite side of the mass scale at less than a few eV [4]. However, all fermion masses are free parameters of the SM and need to be determined by means of experimental measurements.

For the interaction mediators, there is the massless and electrically neutral *photon* (γ), coupling to particles which carry electrical charge — for instance the electron, muon and tau lepton carry charge -1 and the quarks carry $+2/3$ for up-type and $-1/3$ charge for down-type quarks¹ — hence it's the mediator of the *electromagnetic interaction*.

The electrically neutral Z boson and the two charged W^\pm bosons denote the mediators of the *weak interaction*. While being comparatively heavy, $m_W = (80.385 \pm 0.015) \text{ GeV}$ and $m_Z = (91.1876 \pm 0.0021) \text{ GeV}$ [4], the weak force, as the name already suggests, is very short ranged and manifests itself, among others, in the radioactive β -decay. Analog to the concept of electrical charge, all SM fermions carry an additional *weak charge* to which the W and Z bosons couple. Whilst processes including the former involve changing the type and charge of a fermion², the latter behaves somewhat similar to the photon, when energies are high enough. In fact, as will be shown later, the weak and electromagnetic interactions are just two faces of the same underlying theory referred to as the *electroweak interaction*.

The fourth particle in the set of the mediators is the *gluon* (g) being the mediator of the strong interaction. Electrically neutral and massless it couples to fermions carrying so-called *color charge*, which are the quarks. Actually, the gluon itself also features color charge resulting in

¹up-type: up, charm, top; down-type: down, strange, bottom

²see e.g. β -decay

the gluon coupling to itself. As color charged particles form composite states known as *hadrons*, the group of quarks and gluons is named *partons* [5] in this context. The gluon self-coupling and the fact that the corresponding coupling constant of the strong interaction α_s increases with distance has a serious consequence in contrast to all other fundamental interactions. That is, only color-neutral bound states (hadrons) of quarks and gluons can exist, which is referred to as *confinement* [6].

1.1.2 | Gauge theories in the Standard Model

From a mathematical point of view, the Standard Model is a relativistic QFT with a *Lagrange density*, or short *Lagrangian*, \mathcal{L}_{SM} being the central object determining the dynamics and interactions of the full system. It is a scalar function of the quantum fields and their first order derivatives, allowing to find the system's equations of motion by the principle of stationary action. The concept of symmetries hereby plays a crucial role.

First of all, being a relativistic theory, it is required to be invariant under Poincaré transformations, i.e. the action does not change if space-time is translated, rotated or boosted [7]. More technically, the Poincaré group is the non-abelian Lie-group of transformations that leave the distance $ds^2 = g_{\mu\nu} dx^\mu dx^\nu$ between two points in space-time unchanged. Hereby $g_{\mu\nu}$ denotes the metric tensor of the Minkowski space. Requiring this symmetry ensures the conservation of, e.g. energy and momentum as described by Noether's theorem [8].

Another important aspect of symmetry groups, and Lie groups in particular, is their application in gauge theories [9]. The demand on local gauge invariance of the Lagrangian implies the existence of vector fields which not only cancel out the additional terms introduced by the local gauge transformation of the fermion fields and thus lead to local gauge invariance, but also add interaction terms depicting their coupling to the matter fields [10, 11]. In fact, one can identify these vector fields with the bosons of the particle interactions, which is why they are often dubbed *gauge bosons*.

The gauge group of the Standard Model is the combined group $\text{SU}(3)_C \times \text{SU}(2)_L \times \text{U}(1)_Y$ introducing the vector bosons listed in Table 1.1 below.

Table 1.1: Gauge groups of the Standard Model and the according vector bosons.

Gauge Group	Generators	Vector Field	Coupling
$\text{SU}(3)_C$	λ^a	G_μ^a	g_3
$\text{SU}(2)_L$	τ^j	W_μ^j	g_2
$\text{U}(1)_Y$	Y_W	B_μ	g_1

The subgroup $\text{SU}(3)_C$ represents the gauge group of Quantum Chromodynamics (QCD) (strong interaction), hence the index for color (C). It is generated by eight traceless hermitian 3×3 matrices λ^a known as the Gell-Mann matrices. The accordingly introduced vector bosons G_μ^a correspond to the eight gluons of different color charge.

The combined group of $\text{SU}(2)_L \times \text{U}(1)_Y$ is the gauge group of the *electroweak interaction*, i.e. the unified theory of electromagnetic and weak interactions. Here $\text{SU}(2)_L$ represents the

weak isospin with the subscript L reminding that only particles of left-handed chirality couple to the gauge bosons W_μ^a . The three according generators τ^j are commonly known as the Pauli matrices. The remaining $U(1)_Y$ is the symmetry of the *weak hypercharge* Y_W involving particles of both chiralities. However, the $(3 + 1)$ vector bosons of the combined group $SU(2)_L \times U(1)_Y$ cannot simply be identified with the mediator particles observed in nature, i.e. the photon, W^\pm and Z bosons. The reason is that gauge theories in general require the introduced vector bosons to be massless, as a non-vanishing mass term would spoil local gauge invariance again. As a matter of fact, this seems incompatible with the observed W^\pm and Z bosons at first, since they turn out to be quite heavy (see Sec. 1.1.1). The piece missing here is the concept of *spontaneous symmetry breaking* introducing the Higgs-Field which will be shown hereinafter.

The Standard Model Lagrangian so far contains the terms for the matter fields, their interactions with the gauge bosons, as well as the kinetic terms for the latter.

$$\mathcal{L}_{\text{SM}} \supset \mathcal{L}_{\text{matter}} + \mathcal{L}_{\text{gauge}} \quad (1.1)$$

$$\mathcal{L}_{\text{matter}} = \bar{L}_i i \not{D} L_i + \bar{Q}_i i \not{D} Q_i + \bar{e}_i i \not{D} e_i + \bar{u}_i i \not{D} u_i + \bar{d}_i i \not{D} d_i \quad (1.2)$$

$$\mathcal{L}_{\text{gauge}} = -\frac{1}{4} G_a^{\mu\nu} G_{\mu\nu}^a - \frac{1}{4} W_j^{\mu\nu} W_{\mu\nu}^j - \frac{1}{4} B^{\mu\nu} B_{\mu\nu} \quad (1.3)$$

The *matter* part (1.2) contains the kinetic and interaction terms for the left-handed lepton ($L_i \equiv (\nu_{iL} \ e_{iL})^T$) and quark ($Q_i \equiv (u_{iL} \ d_{iL})^T$) doublets, the right-handed electron singlets ($e_i \equiv e_{iR}$) and the right-handed up- ($u_i \equiv u_{iR}$) and down-type ($d_i \equiv d_{iR}$) singlets, where the index i runs over the three fermion generations. The couplings to the gauge vector bosons is encoded in the covariant derivative D_μ , contracted with the Dirac gamma matrices ($\not{D} := \gamma^\mu D_\mu$):

$$D_\mu = \partial_\mu + i g_3 \frac{\lambda^a}{2} G_\mu^a + i g_2 \frac{\tau^j}{2} W_\mu^j + i g_1 \frac{Y_W}{2} B_\mu \quad (1.4)$$

The *gauge* part (1.3) contains the *free field* strength tensors of the gauge bosons defined as

$$G_{\mu\nu}^a := \partial_\mu G_\nu^a - \partial_\nu G_\mu^a - g_3 f^{abc} G_\mu^b G_\nu^c \quad (1.5)$$

$$W_{\mu\nu}^j := \partial_\mu W_\nu^j - \partial_\nu W_\mu^j - g_2 \varepsilon^{jkl} W_\mu^k W_\nu^l \quad (1.6)$$

$$B_{\mu\nu} := \partial_\mu B_\nu - \partial_\nu B_\mu \quad (1.7)$$

where f^{abc} and ε^{jkl} denote the structure constants of the corresponding Lie-Algebra. As mentioned above, it is not possible to introduce mass terms explicitly here, neither for the vector bosons nor for the fermions, as they would spoil the gauge invariance of the Lagrangian [12].

A solution to this apparent contradiction is what is commonly known as *spontaneous symmetry breaking*. Following the Brout-Englert-Higgs mechanism [13, 14, 15], the idea is to introduce a new complex scalar field ϕ of $SU(2)_L$ and introduce an additional term to the Lagrangian

$$\mathcal{L}_{\text{Higgs}} = (D_\mu \phi)^\dagger (D^\mu \phi) + \mu^2 \phi^\dagger \phi - \lambda (\phi^\dagger \phi)^2 \quad \text{with: } \phi = \begin{pmatrix} \phi^+ \\ \phi^0 \end{pmatrix} \quad (1.8)$$

with $\mu^2, \lambda > 0$. The interesting parts here are the last two terms corresponding to the potential $V(\phi) = -\mu^2 \phi^\dagger \phi + \lambda (\phi^\dagger \phi)^2$. This potential has its minimum not located at $\phi = 0$, but rather

features an infinite set of minima located on a circle following $\phi^\dagger \phi = \mu^2/2\lambda$. This results in a non-vanishing Vacuum Expectation Value (VEV) $\langle \phi \rangle$ spontaneously breaking the $SU(2)_L \times U(1)_Y$ symmetries. Conveniently choosing a particular gauge where

$$\langle \phi \rangle = \frac{1}{\sqrt{2}} \begin{pmatrix} 0 \\ v \end{pmatrix} \quad \text{with: } v = \sqrt{\frac{\mu^2}{\lambda}} \quad (1.9)$$

and expanding ϕ around v

$$\phi = \begin{pmatrix} 0 \\ (v + h(x))/\sqrt{2} \end{pmatrix} \quad (1.10)$$

results in an additional neutral real scalar field $h(x)$, i.e. the Higgs-Boson, but more importantly in bilinear terms for the gauge bosons W_μ^j and B_μ yielding their masses. The observable mass-eigenstates then emerge from the original gauge bosons by rotation

$$\begin{pmatrix} A_\mu \\ Z_\mu \end{pmatrix} = \begin{pmatrix} \cos \theta_W & \sin \theta_W \\ -\sin \theta_W & \cos \theta_W \end{pmatrix} \begin{pmatrix} B_\mu \\ W_\mu^3 \end{pmatrix} \quad W_\mu^\pm = \frac{1}{\sqrt{2}} (W_\mu^1 \mp W_\mu^2) \quad (1.11)$$

with θ_W denoting the *weak mixing angle*:

$$\sin \theta_W = \frac{g_1}{\sqrt{g_1^2 + g_2^2}} \quad \cos \theta_W = \frac{g_2}{\sqrt{g_1^2 + g_2^2}} \quad (1.12)$$

The masses of these states then result in

$$m_A = 0 \quad m_Z = \frac{v}{2} \sqrt{g_1^2 + g_2^2} \quad m_W = \frac{g_2}{2} v \quad (1.13)$$

which can be identified with massless photon and the massive Z and W^\pm bosons of the electroweak interaction.

Not only the gauge vector bosons acquire their mass through couplings to the Higgs field, but also the SM fermions. The interaction involved here is denoted as *Yukawa* coupling, which will not be discussed in detail. The full Standard Model Lagrangian then reads

$$\mathcal{L}_{\text{SM}} = \mathcal{L}_{\text{matter}} + \mathcal{L}_{\text{gauge}} + \mathcal{L}_{\text{Higgs}} + \mathcal{L}_{\text{Yukawa}} \quad (1.14)$$

including all the contributions discussed above.

1.1.3 | Physics beyond the Standard Model

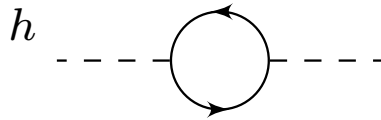
Despite the fact, that the Standard Model is clearly one of the most successful and comprehensive theories in physics, there are however indications that it is not complete and at some point needs to be replaced by a more general theory. In that sense, extensions to the SM are commonly referred to as BSM theories. This section briefly lists a few selected topics, that might hint to such BSM physics.

Inclusion of gravity: The SM does not include gravity as the last missing of the fundamental forces observed in nature. Introducing gravity to the SM by naively adding a corresponding quantum field, i.e. the *graviton*, seems not compatible with the well-established theory of general relativity [16].

Dark Matter and Dark Energy: From cosmology it is apparent that our universe cannot be made exclusively out of ordinary baryonic matter as described by the Standard Model. Classical observations bearing evidence for the existence of *Dark Matter* (DM)³ are the measurement of galaxy rotation curves [17] and the effect of gravitational lensing [18]. Latest measurements of the power spectrum of the *cosmic microwave background* [19] reveal the actual composition of our universe and indicate that its content is only 4.8 % ordinary matter and 25.8 % dark matter. The remaining 69 % are provided by dark energy, a hypothesized form of energy accounting for the accelerated expansion of the universe [20].

Baryon-Asymmetry: The SM features no mechanism to explain the huge imbalance between matter and anti-matter observed in the universe [21]. Since both of them should have been produced in equal amounts during the Big Bang, it is not clear, why today we live in a *matter-dominated* universe.

Hierarchy Problem: With the experimental discovery of the Higgs Boson [22, 23] in 2012, it became clear that the Higgs mass $m_H = (125.09 \pm 0.24) \text{ GeV}$ is much smaller than the Planck scale of $M_p = 2 \cdot 10^{18} \text{ GeV}$ where gravitational effects start to play a role. However, quantum loop corrections to the Higgs mass-squared parameter



tend to push the Higgs mass up to these high energies if not canceled out by delicately fine-tuning these corrections. This is what is commonly referred to as the *Hierarchy Problem* of the Standard Model [24, 25, 26].

Strong CP-Problem: When investigating the vacuum structure of QCD, 't Hooft [27, 28] found that there is an additional (angular) parameter θ not appearing in the original Lagrangian (see Sec. 1.1.2) that leads to an extra term violating CP-symmetry, i.e. the invariance under the combined application of charge conjugation (C) and parity transformation (P):

$$\mathcal{L}_\theta = \theta \frac{g_3^2}{32\pi^2} G_a^{\mu\nu} \tilde{G}_{\mu\nu}^a \quad (1.15)$$

However, measurements indicate that CP actually *is* a symmetry of QCD realized in nature, as seen for example in the vanishing electric dipole moment of the neutron [29]. Although θ in general could take any value of the interval $[-\pi, +\pi]$, observations like this in contrast force it to be $|\theta| \leq 10^{-9}$ [30, 31]. As this seems to be very unnatural⁴, it is known as the *strong CP-Problem* [33].

³denoted *dark* since not interacting electromagnetically and thus being *invisible*

⁴for *Naturalness* see also [32]

There are plenty of BSM extensions aiming to solve (some of) the shortcomings mentioned above, with popular representatives being Supersymmetry (SUSY) [34, 35] or Randall-Sundrum-Models [36] just to name a few. In the next section a particularly beautiful solution to the last item of the above listed, i.e. the Strong CP-Problem, will be presented.

1.2 | Axions and Axion-Like Particles

There is no apparent reason why the CP-symmetry should not be broken in QCD interactions, which is why several attempts in finding a more natural explanation have been made. The probably most compelling solution has been proposed by Peccei and Quinn postulating a new global $U(1)_{\text{PQ}}$ chiral symmetry of the SM, that is spontaneously broken [33, 37]. Following Goldstone's theorem [38], the breaking of such symmetry gives rise to a (pseudo) Nambu-Goldstone boson⁵, in this context commonly named the *Axion* [40, 41]. Denoting f_a the Axion decay constant, i.e. the symmetry breaking scale of the $U(1)_{\text{PQ}}$, the modified total Lagrangian then reads

$$\mathcal{L} = \mathcal{L}_{\text{SM}} + \theta \frac{g_3^2}{32\pi^2} G_a^{\mu\nu} \tilde{G}_{\mu\nu}^a - \frac{1}{2} \partial_\mu a \partial^\mu a + \xi \frac{a}{f_a} \frac{g_3^2}{32\pi^2} G_a^{\mu\nu} \tilde{G}_{\mu\nu}^a + \mathcal{L}_{\text{int}} \quad (1.16)$$

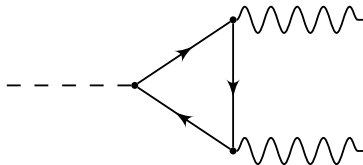
Here, a refers to the Axion field and \mathcal{L}_{int} encodes the interaction terms associated with it. The last but one term represents an effective potential of the Axion field having its minimum at $\langle a \rangle = -\theta f_a / \xi$. At this minimum it is easy to see that the term cancels out the CP-violating θ term, thus naturally restores CP-symmetry in QCD.

However, this *original* Axion model assumed f_a to be in the order of the electroweak scale v_F and has soon been found to be incompatible with experimental observations [42]. After that, *invisible*-Axion models have been proposed, commonly introducing additional scalar fields that are charged under $U(1)_{\text{PQ}}$, best known the DFSZ [43] and the KSVZ [44] model⁶, allowing for much higher values of $f_a \gg v_F$, hence resulting in the Axion being very light.

In all of these models, the Axion mass m_a can be expressed as a function of f_a

$$m_a = \frac{\sqrt{z}}{1+z} \frac{f_\pi m_\pi}{f_a} \approx 1 \mu\text{eV} \left(\frac{10^{10} \text{ GeV}}{f_a} \right) \quad (1.17)$$

where f_π is the pion decay constant, m_π its mass and z further denotes the ratio of light quark masses $z = m_u/m_d = 0.38\text{--}0.58$ [4]. Inherent to all Axion models is the effective coupling to two photons, which is exploited in most experimental searches (cf. Cha. 2):



$$\mathcal{L}_{a\gamma\gamma} = c_\gamma \frac{\alpha}{2\pi f_a} \epsilon_{\mu\nu\rho\sigma} F^{\mu\nu} F^{\rho\sigma} \quad (1.18)$$

$$= \frac{g_{a\gamma\gamma}}{4} F_{\mu\nu} \tilde{F}^{\mu\nu} \quad (1.19)$$

⁵The non-trivial QCD vacuum structure [39] causes the $U(1)_{\text{PQ}}$ to be explicitly broken, which is why the Axion acquires mass and thus is a *pseudo*-Nambu-Goldstone boson.

⁶named after the authors: Dine-Fischler-Srednicki-Zhitnisky and Kim-Shifman-Vainshtein-Zakharov

Here c_γ is a model dependent constant of $\mathcal{O}(1)$, $F_{\mu\nu}$ the electromagnetic field strength tensor and $\tilde{F}^{\mu\nu}$ its dual. As a result, the Axion-photon coupling constant $g_{a\gamma\gamma}$ is inversely proportional to the symmetry breaking scale ($g_{a\gamma\gamma} \propto 1/f_a$) of the $U(1)_{\text{PQ}}$ Symmetry. It follows, since $f_a \gg v_F$, that Axions are very weakly coupled. Further, from (1.17) and (1.19), a constraining relation between the Axion mass m_a and the photon coupling constant $g_{a\gamma\gamma}$ is apparent, resulting in the yellow band shown in Figure 2.5, where the width of this bands accounts for the various model specific details, e.g. the particular value of c_γ .

Axion-Like Particles

Theories aiming to extend the Standard Model frequently introduce new symmetries. If those symmetries are global and spontaneously broken, new Nambu-Goldstone bosons or pseudo-Nambu-Goldstone bosons⁷ emerge. As this is a quite generic mechanism, these lightweight weakly coupled particles are commonly referred to as Axion-Like Particles (ALPs) [45]. Like in the Axion case, ALPs typically couple to two photons. For ALPs transforming like pseudoscalars (ps) the corresponding interaction Lagrangian reads

$$\mathcal{L}_{\phi\gamma\gamma}^{\text{ps}} \propto g_{\phi\gamma\gamma} \epsilon_{\mu\nu\rho\sigma} F^{\mu\nu} F^{\rho\sigma} \phi \propto g_{\phi\gamma\gamma} \mathbf{E} \cdot \mathbf{B} \phi \quad (1.20)$$

while in the scalar case it is

$$\mathcal{L}_{\phi\gamma\gamma}^{\text{s}} \propto g_{\phi\gamma\gamma} F_{\mu\nu} F^{\mu\nu} \phi \propto g_{\phi\gamma\gamma} (\mathbf{E}^2 - \mathbf{B}^2) \phi \quad (1.21)$$

In both cases the coupling constant is inverse proportional to the mass of the ALP. Further, the last terms in (1.20) and (1.21) have been expressed in terms of electric and magnetic fields, which is beneficial when discussing experimental searches in the following.

⁷in case of approximate symmetries or explicit symmetry breaking

2

Experimental searches

There is a theory which states that if ever anyone discovers exactly what the Universe is for and why it is here, it will instantly disappear and be replaced by something even more bizarre and inexplicable. There is another theory which states that this has already happened.

DOUGLAS ADAMS

The potential existence of Axions and Axion-Like Particles is theoretically well motivated not only from the naturalness in the SM point of view, but also in the context of BSM extensions. However, up to this day, no such new particle could have been detected in any experimental search. Even so, as has been demonstrated in Section 1.2, the hypothetical candidates are extremely weakly coupled, as such, they might have escaped any attempt to see them in experiments.

In this chapter, the various concepts of experimental searches, both past and ongoing, will be presented. Thereby a larger focus will be set on Light Shining through a Wall (LSW) experiments, as they will be the main topic throughout the rest of this thesis. For the sake of simplicity, the term ALP will be used for both scalar- and pseudoscalar particle including the (QCD-) Axion if not stated explicitly otherwise¹.

Section 2.1 will start off with the description of the LSW concept and therefor provide the basis for all following chapters in this thesis. Subsequently in Sections 2.2–2.5 complementary ways of searching for ALPs and inferring their properties will be presented. In Section 2.6 the LSW type of ALP searches is contrasted to the other presented approaches before the closing Section 2.7 then summarizes all resulting exclusion limits in a single plot and introduces the ALPlot web application designed to easily create such exclusion plots.

¹There is no commonly accepted naming convention, but most authors tend to use the term *Axion* for the pseudoscalar particle which solves the strong CP-Problem, while the term *ALP* is used for any other (pseudo-) scalar particle originating from an additional broken global symmetry.

2.1 | The Light Shining through a Wall principle

The generic feature inherent to all ALP models is the effective di-photon vertex as introduced in Sec. 1.2. Depending on the parity, the corresponding interaction Lagrangian reads either Eq. (1.21) for scalar or Eq. (1.20) for pseudoscalar ALPs. In both cases, this can be interpreted as the conversion of an ALP into a photon in the presence of an external magnetic field known as *Primakoff-Effect* [46, 47, 48] (see Fig. 2.1a). Note that there is only one *real* photon involved here, as the one provided by the magnetic field is only virtual².

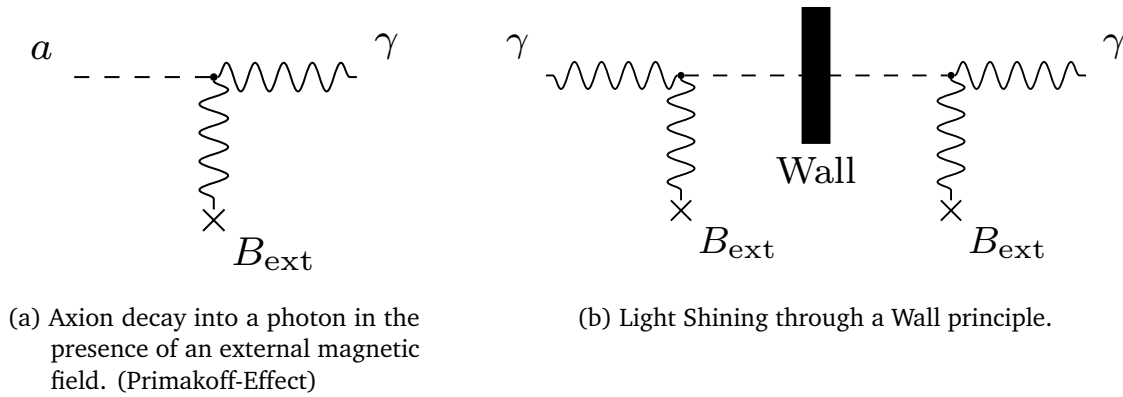


Figure 2.1: Relevant Feynman diagrams for LSW experiments.

The property, that makes scalar ALPs experimentally distinguishable from pseudoscalar ones is the angle between the polarization vector of the (real) photon \mathbf{e}_γ and the vector of the external magnetic field \mathbf{B}_{ext}

$$\text{pseudoscalar} \iff \mathbf{e}_\gamma \parallel \mathbf{B}_{\text{ext}} \quad (\text{parallel}) \quad (2.1)$$

$$\text{scalar} \iff \mathbf{e}_\gamma \perp \mathbf{B}_{\text{ext}} \quad (\text{orthogonal}) \quad (2.2)$$

LSW experiments exploit the Primakoff-Effect twofold (see Fig. 2.1b). The basic idea is to shine high-power laser light through a strong magnetic field onto a fully opaque wall. The laser photons in the B -field convert into ALPs, which then, due to their vanishing interaction with ordinary matter, traverse the wall unobstructed before they see another B -field on the opposite side again, where they decay back into detectable photons. Since the photons from the B -field are only virtual, the real photon in the final state has the same properties, e.g. wavelength and polarization, as the original incoming photon. However, the probability for a single photon-ALP conversion on either side of the wall scales with the square of the coupling constant $P_{a \leftrightarrow \gamma} \propto g_{a\gamma\gamma}^2$, hence this full process ($\gamma \rightarrow a \rightarrow \gamma$) is even more unlikely.

Assuming the laser being linearly polarized and propagating in z -direction, the probability

²In general this process is also allowed for the ALP decaying into two *real* photons in the final state. However, due to $f_a \gg v_F$ and thus $g_{a\gamma\gamma}$ being very small, the spontaneous decay lifetime of this process greatly exceeds the lifetime of the universe [49].

for a single conversion is given by [50]

$$P_{a\leftrightarrow\gamma} = \frac{1}{4} \frac{E_\gamma}{\sqrt{E_\gamma^2 - m_a^2}} g_{a\gamma\gamma}^2 (BL)^2 |F(qL)|^2 \quad (2.3)$$

where E_γ denotes the energy of the laser photon, L the extent of the magnetic field B , and $q = nE_\gamma - \sqrt{E_\gamma^2 - m_a^2}$ the momentum transfer to the magnetic field. The quantity $F(qL)$ is a form factor term depending on the spatial variation $f(x)$ of the magnetic field $\mathbf{B} = \hat{\mathbf{e}}_z B f(x)$ and is given by

$$|F(qL)| := \left| \frac{1}{L} \int_0^L dx f(x) e^{iqx} \right| = \underbrace{\left| \frac{2}{qL} \sin\left(\frac{qL}{2}\right) \right|}_{\text{homogeneous}} \quad (2.4)$$

The last expression in (2.4) is only valid if one assumes a continuous homogeneous magnetic field, i.e. $f(x) \approx 1$, over the full length.

Inserting values of proper scale into (2.3) and (2.4) reveals that the probability for a single photon / ALP conversion is quite small, i.e. is only in the order of $\mathcal{O}(10^{-27})$ assuming a 10 m magnetic field of 10 T and $g_{a\gamma\gamma}$ to be of order $\mathcal{O}(10^{-10} \text{ GeV}^{-1})$. For the purpose of enhancing the sensitivity of LSW experiments, it is apparent from Eq. (2.3) that the product BL is the most striking parameter to improve on, as it scales the conversion probability quadratically. However, this is usually also the most cost-intensive option. Alternatively or in addition, the sensitivity can be further improved by the use of matched Fabry-Perot cavities on either side of the wall as proposed by [51, 52]. The resulting effect is intuitive to understand on the laser side of the wall, in the following denoted *production side*, where the injected photons coherently form a standing wave effectively increasing the *circulating power* within the magnetic field. Given the power buildup β_{PC} of the cavity, i.e. the ratio of circulating to injected power P_0 , the Axion power leaving the Production Cavity (PC) reads $\beta_{\text{PC}} P_0 P_{a\leftrightarrow\gamma}$. However, when placing another Fabry-Perot cavity behind the wall, i.e. on the *regeneration side*, making its eigenmode an extension of the first cavity (see Fig. 2.2), it can be shown that also the ALP-photon reconversion probability is coherently enhanced by the power buildup factor of the Regeneration Cavity (RC). In this case,

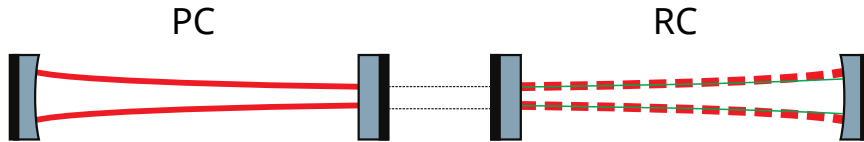


Figure 2.2: Eigenmodes of the Production Cavity (PC) and Regeneration Cavity (RC) for the resonantly enhanced ALP-photon conversion. Taken from [53].

when the RC is locked to the PC, the power of reconverted photons on the regeneration side is given by $\beta_{\text{PC}} \beta_{\text{RC}} P_0 (P_{a\leftrightarrow\gamma})^2$. Thus in summary, employing this scheme increases the sensitivity on the ALP-photon coupling constant $g_{a\gamma\gamma}$ by a factor of $(\beta_{\text{PC}} \beta_{\text{RC}})^{1/4}$.

Including the photon detection efficiency ε and the dark count background rate \dot{n}_b , the sensitivity of an LSW experiment implementing Fabry-Perot cavities for resonantly enhanced

ALP / photon conversion scales like [54]

$$S(g_{a\gamma\gamma}) \propto \left(\frac{1}{BL}\right) \left(\frac{E_\gamma}{P_0}\right)^{\frac{1}{4}} \left(\frac{1}{\beta_{PC}\beta_{RC}}\right)^{\frac{1}{4}} \left(\frac{1}{\varepsilon}\right)^{\frac{1}{4}} \left(\frac{\dot{n}_b}{t}\right)^{\frac{1}{8}} \quad (2.5)$$

where P_0 denotes the laser output power and t the measurement time. As is apparent, the most crucial parameter when aiming for a high sensitivity on $g_{a\gamma\gamma}$ is the product of magnetic field and length BL , but also the power buildups can contribute a large factor as high finesse cavities with $\mathcal{O}(\beta_{PC}\beta_{RC}) = 10^{10}$ seem feasible [53].

Both experiments that will be discussed in the thesis, i.e. OSQAR (see Part II) and ALPS II (see Part III) are of LSW type, whereas only the latter one implements Fabry-Perot cavities. Before this work, the most sensitive experiment exploiting the LSW design was ALPS I [55] (see also Cha. 7), with its results shown in Fig. 2.5.

2.2 | Helioscopes

A somewhat similar type of experiment to search for ALPs are *helioscopes*. Here, an opaque wall is also used to shield a magnetic field from incident light where within ALPs decay into photons via the Primakoff-Effect and are subsequently recognized by photon detectors. In contrast to LSW type experiments however, helioscopes utilize the sun as natural source of ALPs instead producing them in laboratory.

The hot thermal plasma within stars like the sun gives rise to perpetual fluctuations of electrical and magnetic fields thus allowing for the production of ALPs by means of the Primakoff effect³. Once produced, the ALPs leave their solar cradle unobstructed as their mean free path is much larger than the sun's extent. The resulting energy spectrum of the solar ALP flux on Earth can be derived given the temperature, density and chemical composition as described by solar models. Thereby it is important to account for screening effects of the solar plasma, as otherwise the rate of ALP emission is easily overestimated by up to two order of magnitude [56]. Further, recoil effects are assumed to be negligible, thus an ALP created has the same energy as the initial photon. The resulting energy spectrum, integrated over the full solar disc is plotted in Figure 2.3 for the case assuming $g_{a\gamma\gamma} = 1 \cdot 10^{-10} \text{ GeV}^{-1}$. The distribution peaks at a few keV, hence the reconverted photons are in the X-ray regime and thus are well accessible by available detector technologies.

The latest and most sensitive implementation of an ALP helioscope is the CERN Axion Solar Telescope (CAST) located in Geneva, using a refurbished LHC dipole prototype magnet of 9.26 m length with a homogeneous magnetic field of about 9 T. The magnet is mounted on an altazimuth mount⁴ allowing to track the sun for about 1.5 h each during sunset and sunrise. This is possible as both sides of the magnet are equipped with X-ray detectors, i.e. a mixture of CCDs [58] and Mircomegas [59]. The achieved exclusion limits are shown in Figure 2.5 and represent the most stringent limits achieved in a laboratory based experiment, though they inherit some amount of model dependence [57, 60]. The rapid loss of sensitivity in Fig. 2.5 at

³cf. Eqs. (1.20), (1.21) and Fig. 2.1a

⁴a two-axis mount supporting rotations about a vertical and a horizontal axis

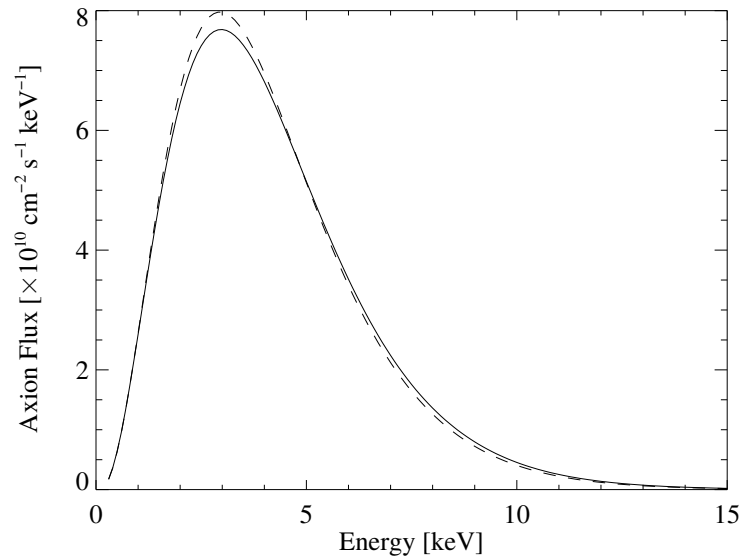


Figure 2.3: Solar ALP flux assuming a coupling constant of $g_{a\gamma\gamma} = 1 \cdot 10^{-10} \text{ GeV}^{-1}$ calculated using a modern solar model from 2004 (solid) and an older model from 1982 (solid). [57]

high masses accounts for the incompatibility of the solar ALP flux model as shown above with other observations like helioseismology and ultimately the suns lifetime itself.

2.3 | Vacuum Magnetic Birefringence searches

Vacuum Magnetic Birefringence (VMB) is an effect predicted in the framework of Quantum Electrodynamics (QED) already described in 1936 by Euler and Heisenberg [61]. Fermion loop corrections induce dichroism and birefringence of the vacuum when permeated by a strong magnetic field. Unfortunately both effects are quite small, which is why until today neither of those could have been observed experimentally. Nevertheless, VMB searches are of particular interest for BSM physics, as ALPs would also induce these non-linear effects due to the coupling to two photons. Hence, the absent observation of magnetic vacuum birefringence and dichroism allows to set model independent limits on the ALP parameter space [62, 63]. The experiment closest to demonstrate VMB and thus the most sensitive to Axion-Like Particles is called PVLAS⁵ and is located in Italy. The measurement principle is depicted in Figure 2.4.

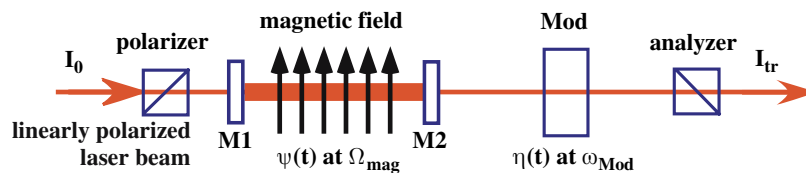


Figure 2.4: Principle of heterodyne detection of small birefringence and dichroism signals. (Adapted from [64, 65])

⁵Polarizzazione del Vuoto con LASer

A linear polarized laser beam is sent through a strong magnetic field where birefringence / dichroism is imprinted by virtual / real ALP production. Like in LSW setups (see Sec. 2.1), a Fabry-Perot cavity is used in order to make the photons pass the magnetic field multiple times, thus enhancing the sensitivity. Further, a heterodyne detection scheme is used, realized by making the magnetic field slowly rotating around the beam axis with angular frequency Ω_{mag} , while using an optical modulator to imprint an artificial time dependent ellipticity with frequency ω_{mod} . This way, the desired signal appears as sidebands to this frequency at $\omega_{\text{Mod}} \pm 2\Omega_{\text{mag}}$ which has major advantages in terms of noise reduction and sensitivity compared to a naive static detection scheme.

The latest constraints on the ALP parameter space from PVLAS are shown in Figure 2.5 and have been extracted from ellipticity measurements [66].

2.4 | Haloscopes

In Section 1.1.3 it was already presented that our universe consists in major parts of Dark Matter, that exposes only feeble (if at all) interaction with ordinary matter as described by the SM. Most of this DM is expected to be *cold*, i.e. non-relativistic, since otherwise it would have smoothed out the universe from initial density fluctuations not allowing for galaxies to form. One of the first observational hints to the existence of DM were the rotation curves of galaxies indicating that the galaxies we observe are embedded in DM halos. Measurements of these curves for our home galaxy estimate the local density of the Cold Dark Matter (CDM) halo at the location of the solar system to be $\rho_{\text{CDM}} = 0.45 \text{ GeV cm}^{-3}$ [67]. A viable candidate for CDM is the Axion [68, 69, 70] and *haloscopes* are constructed to search for them while earth is moving through the galactic halo.

Haloscopes utilize electromagnetic microwave cavities permeated by a strong magnetic field to search for Axions. Flying through the galactic CDM halo, an Axion entering the cavity resonantly converts into an electromagnetic wave, if its mass and kinetic energy matches the resonance frequency of the cavity $\nu = (m_a/2\pi)(1 + \mathcal{O}(10^{-6}))$ [4], thus producing an electromagnetic signal. Steel rods inside the cavity are used to slightly tune its resonance frequency, yet only allowing to cover a narrow range of Axion mass.

The Axion Dark Matter Experiment (ADMX) located at the University of Washington provided the most stringent exclusion limits on Axions achieved by haloscopes so far [71]. Using a 1 m high cavity with 0.5 m diameter placed in a 7.6 T magnetic field, ADMX was able to exclude Axions in the mass range of $1.9 \mu\text{eV}$ to $3.3 \mu\text{eV}$ for densities of $\rho_a \geq 0.45 \text{ GeV cm}^{-3}$ for the KSVZ⁶ case and $\rho_a \geq 3 \text{ GeV cm}^{-3}$ for the DFSZ case [72]. The excluded region in the ALP parameter space is shown in Figure 2.5.

2.5 | Astrophysical observations

Non laboratory based searches and observations are also used to narrow the allowed ALP properties. However, sometimes these observations can even hint to ALPs favoring a particular region

⁶cf. Section 1.2

in parameter space.

A popular example in the former sense is the observation of supernova SN1987A. During the core collapse phase, myriad ALPs would have been produced through the Primakoff-Effect (see Fig. 2.1a) and have subsequently been converted to γ -ray photons in interstellar magnetic fields⁷. Therefor the absence of γ -rays in coincidence with the neutrino flux emitted by the supernova allows to set a exclusion limits on the ALP-photon coupling. The observation of SN1987A excluded ALPs with a coupling constant $g_{a\gamma\gamma} < 5.3 \cdot 10^{-12} \text{ GeV}^{-1}$ for masses m_a below $4.4 \cdot 10^{-10} \text{ eV}$ [73, 74, 75].

The interstellar magnetic fields, mentioned above, inherit a second observable effect involving photons on the TeV scale originating from extragalactic γ -ray sources. These photons are expected to undergo electron-positron pair production $\gamma + \gamma \rightarrow e^+e^-$ with low energy photons of the Extragalactic Background Light (EBL), resulting in an effective attenuation of the TeV photon flux. However, there are indications, that the universe is more transparent to TeV photons than expected [76] with a possible explanation being the conversion of these photons into ALPs within interstellar magnetic fields. ALPs would thereafter cover long distances before being converted back to TeV photons being observed on earth. However, as this mechanism clearly depends on initial assumptions of the EBL, the situation currently remains unclear [77]. Anyway, the allowed region of parameter space for ALPs viable to explain the seeming TeV-Transparency of the universe is within reach of the ALPS II experiment (see Cha. 7).

Another category of astrophysical processes relevant in the context of ALPs is the cooling of stars where they could theoretically contribute an additional channel of energy loss. Of particular interest in this sense are Galactic Globular Clusters (GGCs) and more specifically the stars residing in the horizontal branch⁸ that would be effected most by additional cooling through ALP emission via the Primakoff-Effect. The ratio between those and the stars in the *red giant branch* allows to derive limits in the ALP-photon coupling. Though in a recent analysis [78] a weak indication of such anomalous cooling process compatible with the Primakoff-Effect of $g_{a\gamma\gamma} = 4.5_{-1.6}^{+1.2} \cdot 10^{-11} \text{ GeV}^{-1}$ has been found, the same analysis also provides an upper bound of $g_{a\gamma\gamma} < 6.6 \cdot 10^{-11} \text{ GeV}^{-1}$.

2.6 | LSW type compared to others

Having presented various different approaches to search for ALPs, this section briefly emphasises the main advantages and drawbacks of LSW type experiments.

First of all, the LSW type searches do not expose any model dependencies, whereas e.g. Helioscope searches (mildly) rely on the solar model used to calculate the ALP flux on earth or Haloscopes heavily rely on cosmological models predicting the CDM abundance at earths position. Further, the LSW type searches are sensitive in wide range of ALP masses in contrast to Haloscopes, that are designed for a very specific and narrow mass range. This broadband sensitivity is a feature that LSW experiments share with Helioscopes, due to their similar search strategy. On the other hand, this comes with the price of generally lower sensitivity on the

⁷Note that these magnetic fields are usually much weaker compared to those created in laboratory. But as opposed to this, their effective length scales are much larger and hence (BL) is again of notable size.

⁸Horizontal branch refers to a stage of evolution named after their occurrence in the Hertzsprung–Russell diagram.

ALP-photon coupling constant $g_{a\gamma\gamma}$ compared to narrowband Haloscopes. This goes in hand with the fact that with LSW experiments of the current stage it is impossible to probe the QCD-Axion band, i.e. the region of parameter space, where the Axion solving the strong CP-problem is expected, whereas Helioscopes and Haloscopes at least partially do.

Nevertheless, LSW experiments are very well suited to look for ALPs in a model independent way, exploring interesting regions of parameter space (cf. Sec. 2.5, CDM).

2.7 | The ALPlot

Summarizing all searches and observations described in this chapter in a single plot gives an overview of the already well excluded and but also the remaining allowed regions of parameter space for ALPs. Such summary plot is shown in Figure 2.5.

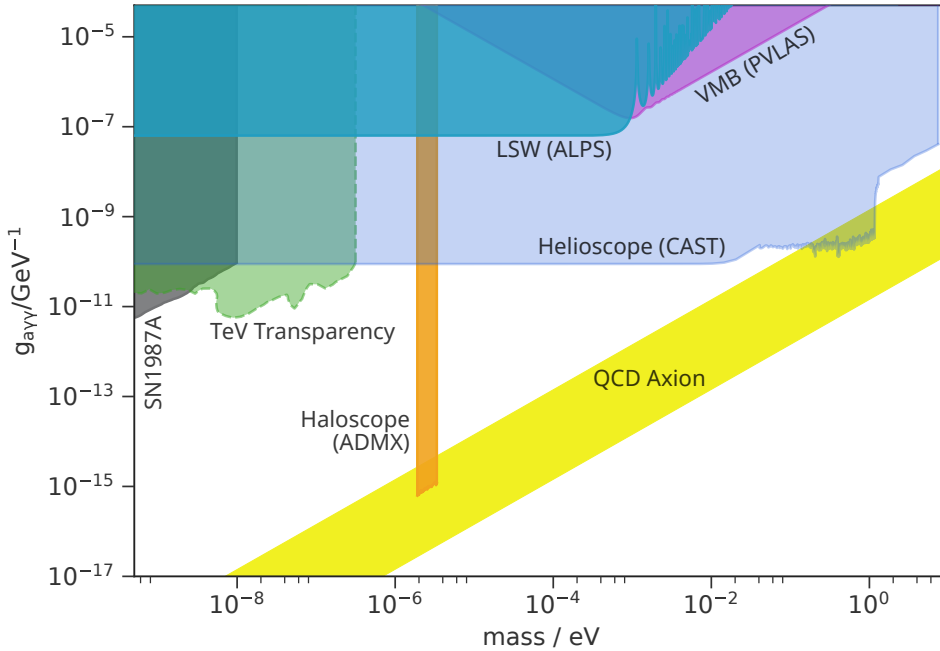


Figure 2.5: Summary of Axion-Like Particle exclusion limits created with the ALPlot web application.

This plot has been created using the *ALPlot — Axion-like Particle Exclusion Plots* web application, designed and implemented in the course of this thesis. The purpose of this web application is to collect the results of experiments and observations, providing them to the user for creating exclusion plots of the ALP parameter space as shown above. The plots and their composition are thereby fully customizable. The user may also create its own datasets to be included in the plot or explore how the sensitivity of e.g. LSW experiments changes when varying their parameters like BL or the laser wavelength.

The ALPlot web application is open source, licensed under BSD-3 and thus free to use, distribute and modify. The latest version is hosted at

<https://alplot.physik.uni-mainz.de/>

3

Overview of this work

We can only see a short distance ahead,
but we can see plenty there that needs to
be done.

ALAN TURING

After laying out the theoretical basis of the SM and motivating the search for ALPs, the now following work is split in parts devoted to the two most advanced Light Shining through a Wall experiments searching for ALPs at the low energy frontier, namely OSQAR located at CERN and ALPS II located at DESY. The given structure follows a chronological order as conducted during this thesis, whereas it should be noted, that, while OSQAR is an up and running experiment, ALPS II is still in the design and commissioning phase.

Part II will start in Chapter 4 with a general description of the OSQAR experiment and introduces the relevant terminology. Chapter 5 will then continue with a more detailed view on the several steps of data processing and selection, the cleaning algorithms, and finally describes the analysis method used to perform the search for ALPs with OSQAR. The last chapter of this part (Cha. 6) then summarizes the derived exclusion limits on (pseudo-) scalar ALPs, stating the most stringent limits provided by LSW type experiments up to today.

Part III then is devoted to the next development stage of LSW setups, i.e. the ALPS II experiment. Chapter 7 will again start with a general description of the ALPS II design including the foreseen improvements over its predecessor ALPS I and a particular focus on the detector concept of ALPS II as this will provide the context for the following thread of topics. This is, establishing a detector interface with the rest of the experiment (Cha. 8), designing and implementing a global slow control and a fast data acquisition system (Cha. 9), and finally developing a data analysis framework including algorithms for signal photon identification and background event suppression (Cha. 10). The closing Chapter 11 then concludes with a summary of the reached achievements and provides an outlook on the timeline of ALPS II.

The last Part IV of this work finishes with a brief summary of the discussed topics and tries to integrate this work in the general picture of ALPs searches.

Part II

OSQAR Experiment

4

Description of the OSQAR experiment

Experiments are the only means of knowledge at our disposal. The rest is poetry, imagination.

MAX PLANCK

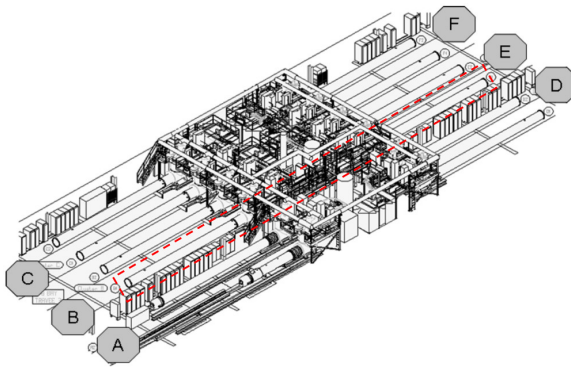
The Optical Search for QED vacuum birefringence, Axions and photon Regeneration (OSQAR) is a classic LSW type experiment (cf. Sec. 2.1) searching for ALPs. Exploiting the effective diphoton vertex, it utilizes two LHC dipole magnets, which provide the external magnetic fields for laser photons to convert into ALPs and back. On the optical side, it uses an 18.5 W solid state laser and a low-noise CCD for detecting the reconverted photons.

This chapter briefly describes all these subsystems and their interplay starting with the magnetic system in Section 4.1, followed by the laser and photon detection setup in Section 4.2. The last Section (4.3) then presents the procedure and protocol of data taking necessary for the subsequent chapters.

4.1 | Magnet system

The OSQAR experiment is situated in the SM18 hall at CERN in Geneva, an advanced test facility hall for magnets and instrumentation at low temperatures. Recently used to verify the functionality of the dipole magnets during installation of the Large Hadron Collider (LHC), it houses the infrastructure, i.e. cryogenics, high current power supplies and controls to operate several magnet test benches simultaneously.

The horizontal magnet test benches are arranged in two opposite groups of six parallel benches each separated by the supply infrastructure like the cryogenic feedboxes, as can be seen in Figure 4.1a. Two of these benches, forming a straight line with an unobstructed passage way in between, are used for the OSQAR setup. On both benches, one of the spare LHC superconducting



(a) Schematic view of the SM18 hall. The test benches dashed in red host the OSQAR experiment.



(b) Picture of the OSQAR laser hut and the production magnet.

Figure 4.1: OSQAR experimental site located in the SM18 magnet test facility hall at CERN. [79]

dipole magnets is mounted each providing a homogeneous magnetic field over 14.3 m length. The vertically oriented magnetic field thereby permeates two parallel beam pipes in opposite direction. The magnet's cold mass is cooled down to a temperature of 1.9 K using liquid helium. A cross-section of the dipole magnets *cold mass* is depicted in Figure 4.2.

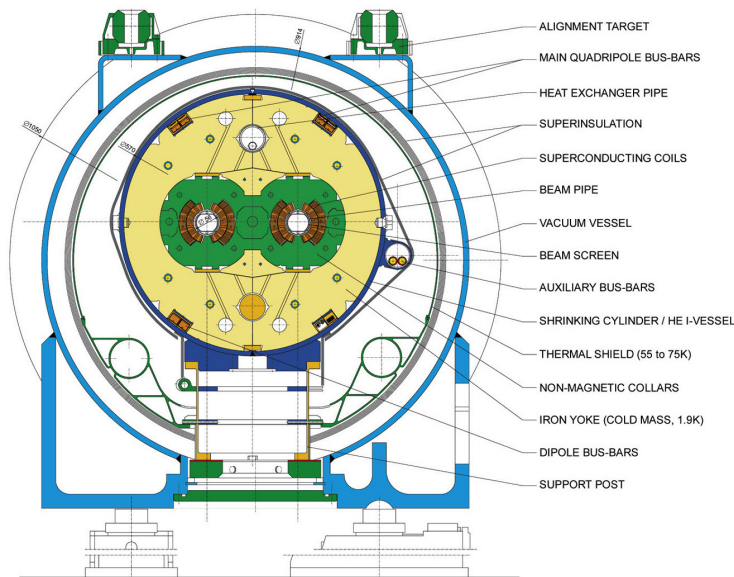


Figure 4.2: Schematic cross-section of the LHC dipole magnets. [80]

Though the dipoles were designed [80] to provide a nominal field of 8.33 T running with 11 850 A of electrical current, it is possible to operate them with an ultimate current of 12 840 A generating a magnetic field of 9 T, which is done for OSQAR. This is still well below the quench limit of 9.7 T, thus safe to operate.

In order to provide a clear aperture throughout the full length of the experiment, both dipole magnets have been aligned using a LTD 500 Laser Tracker from Leica. Further, both magnets have been equipped with *warm bore anticryostats* in order to perform magnetic field

measurements with common (room temperature) equipment. As a result, the free aperture of the bores has been measured to be 40 mm [81, 82].

Both beam pipes have been evacuated using turbo-molecular pumping groups, reaching down to 10^{-7} mbar of pressure. Apart from that, the operation of the dipole magnets has mainly been in the custody of the experienced SM18 staff.

4.2 | Laser and photon detector

The optical setup of the OSQAR experiment is housed in a laser safety hut directly attached to the first of the LHC dipole magnets (cf. Fig. 4.1b), covering the beam pipes up to the vacuum vessel. The used main laser is a Verdi V18 from Coherent Inc. delivering 18.5 W continuous wave output power. It is a diode-pumped solid state laser emitting monochromatic light of 532 nm wavelength linearly polarized in vertical direction. A $\lambda/2$ waveplate is subsequently used to adjust the polarization vector according to the desired relative orientation to the magnetic field. Basically either perpendicular or parallel alignment is used in order to search for scalar and pseudoscalar ALPs (cf. Eqs. (2.1), (2.2) and Sec. 2.1). As will be seen in Section 8.1, laser beams of large diameter exhibit less divergence compared to small sized beams, hence an optical telescope is installed in front of the beam pipe entrance collimating the beam to a spot size diameter of about 6 mm, well below the aperture limits of the beam pipe to avoid clipping.

After traversing and exiting the first magnet, the laser light is safely dumped, whereas the entrance of the second magnet is tightly sealed preventing stray light from entering the ALP \rightarrow photon regeneration area. For initial alignment and further diagnostics however, this seal can be removed.

The exit of the second magnets beam pipe thereafter is directly connected to the photodetector, realized by a thermo-electrically cooled Charge-Coupled Device (CCD) from ANDOR Co.¹ featuring 1024×1024 pixels of $13 \times 13 \mu\text{m}$ size equally distributed on an active area of 177 mm^2 . A focusing lens in front of the CCD is used to minimize the spot size on the pixel surface, in order to increase the Signal-to-Noise Ratio (SNR). As a result, more than 95 % of the beam are contained in an area of less than 4 pixels. The temperature of the CCD during operation is kept at -95°C , which effectively reduces the dark count rate, i.e. thermally excited electrons, since their rate is logarithmically related to the temperature.

4.3 | Data taking and preparation

The process of running the experiment and acquiring data is subdivided into *Runs* each composed by a sequence of measurements following a particular scheme. At the beginning of all runs, the light-tight seal at the entrance of the second magnet is removed and the laser output power is significantly lowered. Data acquisition then starts with capturing three consecutive CCD frames² of short exposure time (0.01 s) each separated by a 60 s pause. This will allow to identify the

¹Model: DU934P-BEX2-DD

²The term *frame* here and in the following denotes the acquisition of a single image with the CCD resulting in a 2D array of integer values.

signal region, i.e. the region where to expect reconverted photons, in the later analysis. After that, the seal is put back in place and the laser is set back to full power. What follows next is the main LSW measurement comprised by two sequentially acquired frames of 5400 s exposure each. A small pause of 100 s in between is required to perform the digital readout³. Finally, the procedure from the beginning of the run is reversed, i.e. the laser is switched to low power and the seal is removed again for the reason of acquiring another set of three short exposure frames. This way it is possible to check for relative drifts of the laser-CCD alignment.

The frames acquired by the camera are stored as comma separated values in plain text files in the first place, which ensures future-proof platform independent portability. However, this way of representing data in memory is particularly inefficient and disc space consuming, which is why a second format has been chosen for processing and analyzing the data, whereas the original text files remain as backup. The format used for further processing is called **HDF5** (Hierarchical Data Format, version 5) and is designed for scalability, speed and portability of large datasets [83]. API bindings to all major programming languages enables easy and versatile processing. For OSQAR, each HDF5 file represents a particular Run containing all important information for further processing and analysis (see Fig. 4.3). The three main nodes contain the CCD frames for the beam position measurements in the beginning and end of a Run, and the main LSW frames. Further, relevant metadata like the Run number, the laser power, and the laser polarization relative to the magnetic field is stored as key-value pairs.

The advantage of this is that all data from a Run is collected in a single file, using memory efficient storage algorithms allowing for fast access and processing.

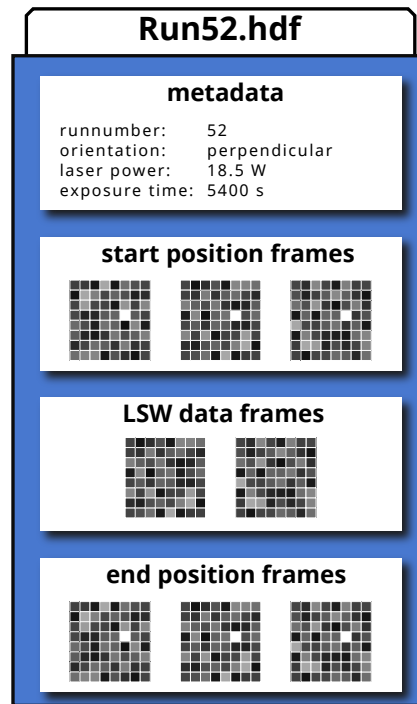


Fig. 4.3: Representation of a single run in the HDF5 format.

³Note that in order to reduce the *readout noise* the slowest Analog/Digital-Converter (ADC) rate implemented by the CCD has been used.

5

Searching for ALPs with OSQAR

God used beautiful mathematics in
creating the world.

PAUL DIRAC

The workflow of processing and analyzing the acquired data basically breaks down into two major parts. First of all, the runs are treated individually, that means isolated from each other, where all necessary (CCD) corrections and data quality criteria are applied. After that in a second step, the information about signal and background of the valid runs are used to infer a combined exclusion limit.

In Section 5.1 the former part is presented, giving an overview of the processing chain on single data runs, starting with finding the signal region and introducing all applied corrections. Finally, the amount of signal and background counts are evaluated and stored separately for each run. Section 5.2 thereafter introduces the limit setting method, which combines the results derived before into exclusion limits for scalar and pseudoscalar ALPs. In addition, a consistency check is performed in order to verify the overall analysis workflow.

5.1 | Data processing

As mentioned in the introduction above, the first part of the analysis workflow focuses on the data runs individually. Hence, the underlying datasets are comprised of the 2×3 beam position frames taken in the beginning and end of each run and of course the 2 consecutively acquired LSW frames. If any of the frames is missing, in particular the beam position frames, or the experimental setup has been tampered with during a run, e.g. temporary loss of the magnetic field, the whole run is excluded from the analysis. An overview of all rejection reasons and their frequency of occurrence is given in Section 5.2.

5.1.1 | Signal region definition

The most crucial information, stating the basis for the whole analysis chain, is the knowledge about which pixels on the CCD are exposed to possible reconverged photons, which is also the main reason for taking the *beam position frames* on each run (cf. 4.3). With the light seal opened, the laser beam is passing through both magnets, illuminating the region of interest on the CCD. As will be explained in greater detail in Section 8.1, the intensity profile of a laser beam can be parameterized with a 2D gaussian distribution, hence this function is fitted to the beam position frames yielding the beam position on one hand and its size on the other. Figure 5.1a exemplarily shows this fit for data of Run 90. As can be seen, the number of illuminated pixels is small, which comes as a result of the efforts focusing the beam tightly on the CCD's active area. The average spot size over all runs is (0.67 ± 0.05) pixel on the 1σ -level.

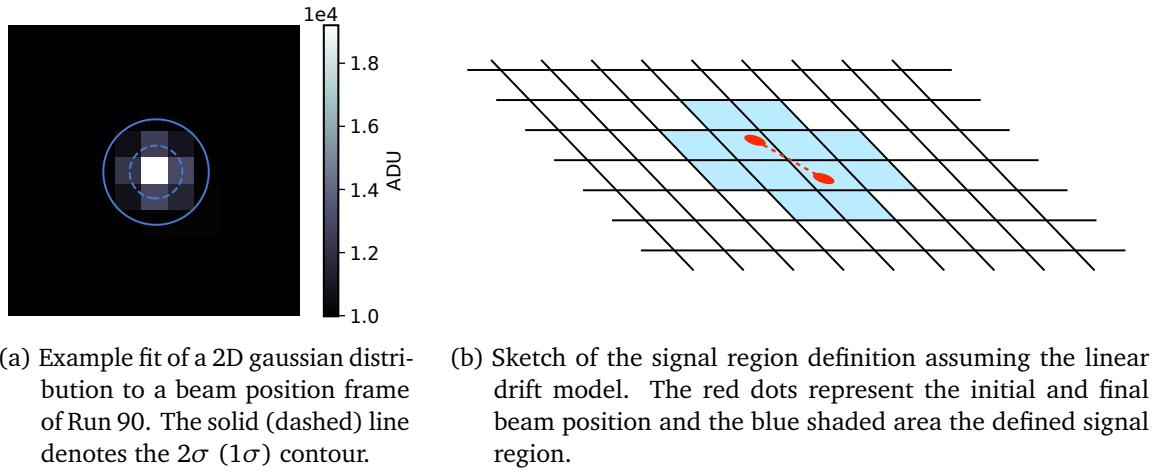


Figure 5.1: Signal region inference from beam position frames.

However, it has been observed, that the position of the beam spot is not entirely stable, but instead is subject to ultra slow drifts, mainly on the vertical axis. Further investigations of this effect have revealed, that environmental temperature changes due to the day-night cycle inside the SM18 hall introduce small deformations of the CCD support structure. The resulting relative displacements of the beam spot have shown to be unidirectional and typically below one pixel per hour. Taking the beam position frames acquired at the end of every run into account, the initial and final positions can be compared.

In order to conservatively define a *signal region*, i.e. the set X_{SR} of pixels exposed to reconverged photons, all pixels within $2\sigma_{\text{Run}}$ reach are considered, where σ_{Run} denotes the maximum value of the measured spot size in the start and end beam position frames. In case the initial and end positions of the beam do not coincide, the signal region is extended to all pixels within a $2\sigma_{\text{Run}}$ orthogonal distance to the connecting line between both points (cf. 5.1b).

$$X_{\text{SR}} = \{ \mathbf{x} \in X_{\text{CCD}} \mid 2\sigma_{\text{Run}} \geq | \mathbf{x} - [\mathbf{x}_i + t \cdot (\mathbf{x}_f - \mathbf{x}_i)] | \quad \forall t \in [0, 1] \} \quad (5.1)$$

Here \mathbf{x}_i and \mathbf{x}_f denote the initial (i) and final (f) beam positions and X_{CCD} the full set of pixel coordinates on the frame. As a consequence of this, the signal region varies from run to run.

5.1.2 | CCD corrections

After identifying the run-specific signal region, the next step is to apply CCD corrections on both LSW frames of the run, before evaluating the signal and background counts. At this point, for the first time in the analysis workflow, the data frames are actually altered, hence it is crucial to prove that the applied *corrections* do not spoil a possible signal content, which will be shown in Section 5.2.2.

Baseline correction

Given the geometry of the CCD interior, the cooling performance of the active area is not perfectly homogeneous, which gives rise to small temperature gradients across the chip. Directly related to these temperature gradients are small distortions of the frames baseline, leading to a non flat image response. In order to correct for this effect, a map of weights is created from the following definition.

$$w(x, y) = \frac{\text{med}[\{f(x+i, y+j) \mid i, j \in [-10, +10]\}]}{\text{med}[\{f(\mathbf{x}) \mid \mathbf{x} \in X_{\text{CCD}}\}]} \quad (5.2)$$

Here $f(x, y)$ refers to the pixel content at position $\mathbf{x}^T = (x, y)$ and $\text{med}[\cdot]$ to the *median* of the set in braces. Put simply, for each pixel of the frame, the median of its content and the contents of the surrounding 10×10 pixels is taken (local median) and is divided by the median of all pixels contents of the frame (global median). This way, a map of weights is created indicating the *local* baseline levels with respect to the *global* one. Figure 5.2 exemplarily shows such a weight map for the second frame of Run 90.

The reason for choosing the *local median* over the *local arithmetic mean* in this scheme is that it is more robust against outliers. This is an important property here, since at this stage, the (long exposed) frames are polluted by cosmic ray hits (see below) resulting in randomly distributed super bright pixels.

Each pixel in the original frame gets corrected by applying the corresponding weight from the baseline correction map. As one can see from Figure 5.2, all weights are close to unity proving that the effect of baseline distortion in general is small. However, since the baseline can vary from frame to frame, the weight map needs to be recalculated for every single frame individually.

Bias frame

The second correction applied is a very common operation in all kinds of scientific CCD imaging applications, namely the subtraction of the *bias frame*.

The basic working principle of a CCD is to convert the number of photo-electrons collected in each pixels to a digital value, referred to in Analog Digital Units (ADUs). Therefore the content of each pixel is amplified by a fixed gain and shifted up by an offset before the digitization process occurs. In a perfect sensor, there would not be any difference between the various pixels on the chip. In reality however, there are slight changes of these parameters from pixel to pixel,

which is why it is necessary to correct for them.

The bias frame is constructed to reflect these differences across the sensor and is applied by subtracting it from the actual frame to be corrected. In order to obtain the bias frame in the first place, several no-exposure-time frames with the camera shutter closed are taken and averaged, which means, all these no-exposure frames are added pixel-wise and all pixels thereafter are divided by the number of no-exposure frames. The averaging is needed as the content of each pixel is still subject to random readout noise.

Cosmic hit removal

The last correction step deals with the already mentioned cosmic ray hits, short *cosmics*. Out of the unceasing showers of cosmic rays hitting the atmosphere, charged particles — mainly muons — hit the CCD sensor now and then¹. Depositing a small fraction of their energy inside the chip, they manifest as ultra bright pixels or clusters of pixels, which is illustratively shown in Figure 5.3.

The information stored in the affected pixels is effectively lost for the analysis, thus they need to be identified and excluded from all further steps. The classification whether a pixel has to be removed or not is done by simple *threshold clipping*, which means, that a pixel whose content exceeds a certain predefined threshold is marked to be removed. The used clipping threshold is calculated for each frame individually, to compensate for possible variations of the base level or readout noise.

Obviously, the signal region is excluded from this cleaning procedure to not spoil a possible signal excess by removing those pixels. However, if the signal region is apparently hit by cosmics, as a comparison with other frames would reveal, the whole run is excluded from the analysis.

5.1.3 | Counting

The last run-individual step in the analysis workflow is the actual counting. At this point, the frames have undergone the correction procedures described above and only bias and cosmic free frames are left to be evaluated.

Starting with the most obvious, the signal region is evaluated by summing up all corresponding pixel contents to form n_s , i.e. the number of cumulated signal counts. In order to compare this number with the background expectation, all other pixels of the frame, outside the signal region and not masked by the cosmic ray filter, are used to infer the background distribution. For this purpose, the background pixels are grouped together in clusters of the same size as the signal region. For each of these clusters the content is again accumulated and filled to the background histogram of the frame. In Figure 5.4, the resulting background distribution together with the signal region counts is exemplarily shown for Run 90.

As can be seen, for this particular case the number of signal counts n_s is well consistent with the background expectation. In order to quantify this agreement in the next step, the background distribution is fitted with a gaussian distribution as indicated in Figure 5.4. The resulting fit for

¹The rate of muons on the earths surface is approximately $1 \text{ cm}^{-2} \text{ min}^{-1}$ [4].

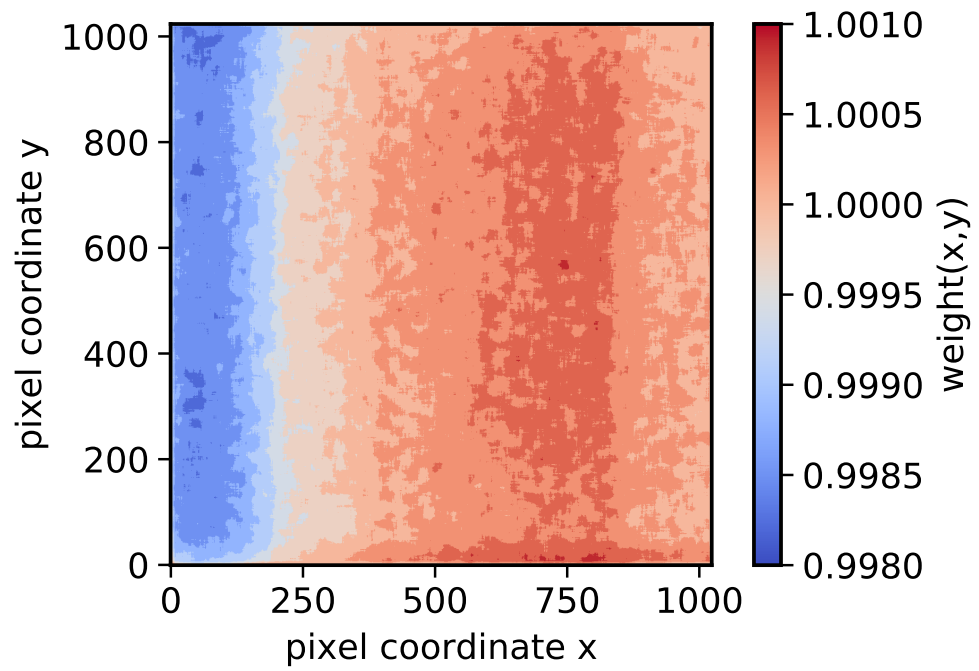


Figure 5.2: Baseline correction weight map for the second frame of Run 90.

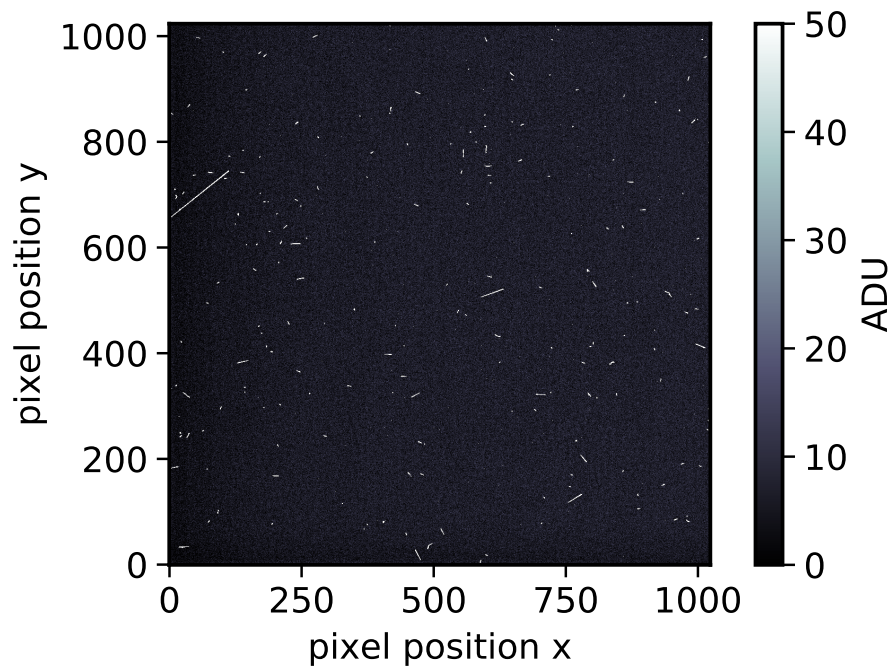


Figure 5.3: Cosmic ray hits on a long-exposed frame of Run 90.

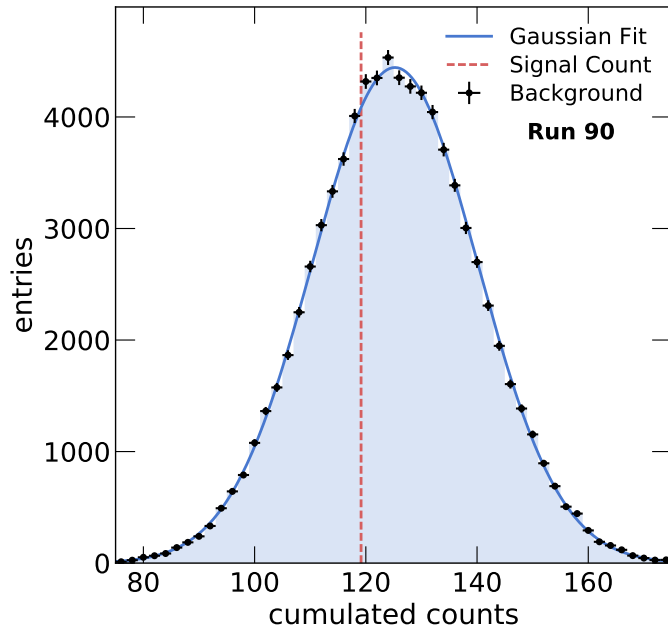


Figure 5.4: Background distribution (blue shape and black dots) and signal yield (red line) of Run 90. The background histogram has been fitted (blue line) using a gaussian distribution.

this run yields $\hat{\mu}_b = (125.24 \pm 0.05)$ ADU with a standard deviation of $\hat{\sigma}_b = (14.83 \pm 0.04)$ ADU. The reduced χ^2 of 56.6/47 proves a reasonable description of the data.

This representation of a frame can further be used to cross-check the CCD specifications given by the manufacturer, such as the *dark count rate*, i.e. electrons thermally created within the pixels adding to their ADU counts. Apparently this depends on the operation temperature of the CCD, but also scales approximately linearly with the exposure time, as thermal electrons accumulate until readout. From the cameras datasheet one reads a value for the dark count rate of $\approx 0.001 \text{ e}^- \text{ pixel}^{-1} \text{ s}^{-1}$ for the used operation temperature of $-95 \text{ }^\circ\text{C}$, which is well compatible with the $0.0012 \text{ e}^- \text{ pixel}^{-1} \text{ s}^{-1}$ estimated from the histogram shown above.

5.2 | Setting ALP exclusion limits

The dataset used in this thesis has been taken during the LSW campaign of OSQAR in August 2014 and is comprised of 119 experimental runs in total. Thereby 59 runs were taken with $(\mathbf{e}_\gamma \parallel \mathbf{B}_{\text{ext}})$, i.e. searching for *pseudoscalar* ALPs, whereas 60 runs were devoted to *scalar* ALPs $(\mathbf{e}_\gamma \perp \mathbf{B}_{\text{ext}})$. However, as already mentioned above, not all runs fulfill the required data quality criteria and have thus been excluded from the analysis. Table 5.1 gives an overview of the main reasons for rejecting a run from the analysis. The remaining runs correspond to 267 h of LSW data, which is used in the following to derive exclusion limits on ALPs, as no significant excess of signal counts could have been observed.

Table 5.1: Reasons to exclude runs from the analysis. The \parallel / \perp symbols in the second and third column refer to the relative alignment of laser polarization and magnetic field.

Rejection Reason	Rejected \parallel -Runs	Rejected \perp -Runs	Total Fraction / %
magnet quench or no B-field	4	11	12.6
no beam position measurement	2	1	2.5
data storage integrity	1	2	2.5
temperature stability	1	1	1.7
cosmic hit in signal region	0	1	0.8
other	4	2	5.0

5.2.1 | Bayesian method

The data processing workflow described in Section 5.1 yields three quantities for each valid run, namely the signal counts $n_{s,i}$, the estimated mean of the background distribution $\hat{\mu}_{b,i}$ and the corresponding standard deviation $\hat{\sigma}_{b,i}$ of the background distribution. The index i is used here to distinguish these quantities for the individual runs.

Assuming there are Axion-Like Particles showing up in the experiment as reconverted photons, these photons produce an excess of counts in the signal region over the background expectation in all runs. As usual in counting experiments, the number of signal counts is modeled by a Poisson distribution $\mathcal{P}(\frac{dN}{dt} \cdot t^{\text{exp}})$, here $\frac{dN}{dt}$ is the number of signal counts² per second and $t^{\text{exp}} = 2 \times 5400$ s is the integration (measurement) time of each run. Since the background expectation is found to be gaussian distributed, the goal is now to evaluate how likely it is to find

$$n_{s,i} = \underbrace{n_{b,i}}_{\text{bkg. only}} + \underbrace{\mathcal{P}\left(\frac{dN}{dt} \cdot t^{\text{exp}}\right)}_{\text{reconv. photons}} \quad (5.3)$$

counts in the signal region, while only expecting $\hat{\mu}_{b,i}$ varying about $\hat{\sigma}_{b,i}$. For this purpose a Bayesian approach [4, 84, 85] has been chosen, inferring knowledge about $\frac{dN}{dt}$ from experimental observations. From the considerations above, one can construct the following Likelihood function combining all runs in a single model:

$$\mathcal{L} \propto \prod_{i \in \Omega} \mathcal{N}(n_{s,i} | \hat{\mu}_{b,i} + \mathcal{P}\left(\frac{dN}{dt} \cdot t^{\text{exp}}\right), \hat{\sigma}_{b,i}) \quad (5.4)$$

The notation $\mathcal{N}(x|\mu, \sigma)$ represents the probability of randomly drawing a sample x from a gaussian distribution of given parameters μ and σ . The index i runs over the set of run numbers Ω of either parallel or perpendicular polarization.

The posterior distribution — in *Bayesian speech* the *belief* about the parameter of interest updated by the experimental observation — denoted as $p(\frac{dN}{dt} | \text{data})$ is now inferred by marginal-

²Note: The signal count rate must not be confused with the rate of reconverted photons. However, both quantities are directly related by the *detection efficiency*, i.e. mean number of photons required to generate one count (measured in ADU) in a CCD pixel.

izing the likelihood (5.4) after choosing a so-called prior distribution $\pi(\frac{dN}{dt})$ that represents the knowledge *prior* to the experimental observation³. For this analysis a flat prior distribution is assumed, as it embodies the unbiased *zero-knowledge* presumption of the parameter of interest. The marginalization itself is done numerically using Markov Chain Monte-Carlos (MCMCs) [86] implemented in the PYTHON package PYMC [87]. In order to minimize numerical fluctuations and thus uncertainties on the posterior, a huge number of random samples is required in the MCMC process. For the case of this analysis, it has been found, that twenty million samples for each polarization are enough to diminish this uncertainty to a negligible level.

5.2.2 | Consistency checks

In order to thoroughly verify the whole analysis workflow, including all correction/filtering steps and statistical methods described above, a fake signal is imposed on all runs with the goal to be reproduced by the analysis chain.

The used fake signal is injected into the signal regions of all LSW frames and corresponds to a signal count rate $\frac{dN}{dt}$ of 10^{-3} s^{-1} . Realistically⁴ this would represent an ALP with $g_{a\gamma\gamma} = 3.8 \cdot 10^{-8} \text{ GeV}^{-1}$ and $m_a \leq 1 \cdot 10^{-4} \text{ eV}$. Like in the original analysis, the runs are treated separately according to the laser polarization setting. The resulting posterior distributions for both cases are shown in Figure 5.5.

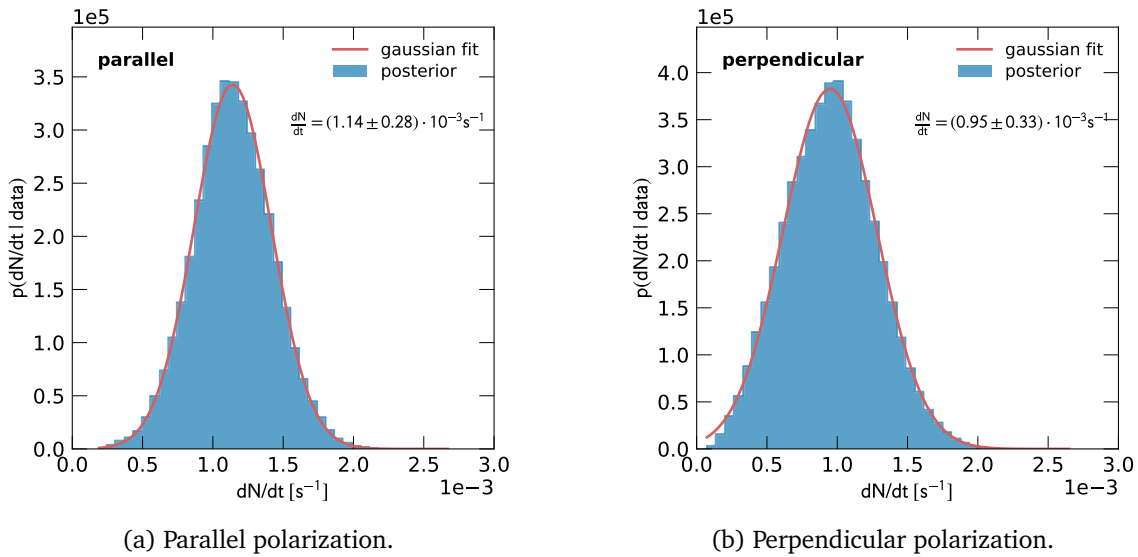


Figure 5.5: Consistency check of the full analysis workflow including all corrections and statistical methods. The fake signal of $\frac{dN}{dt} = 10^{-3} \text{ s}^{-1}$ is consistently reconstructed for both polarization cases.

As can be seen from the posterior distributions, the artificial signal of $1 \cdot 10^{-3} \text{ s}^{-1}$ is consistently reconstructed by the analysis resulting in $(1.14 \pm 0.28) \cdot 10^{-3} \text{ s}^{-1}$ in the parallel case and

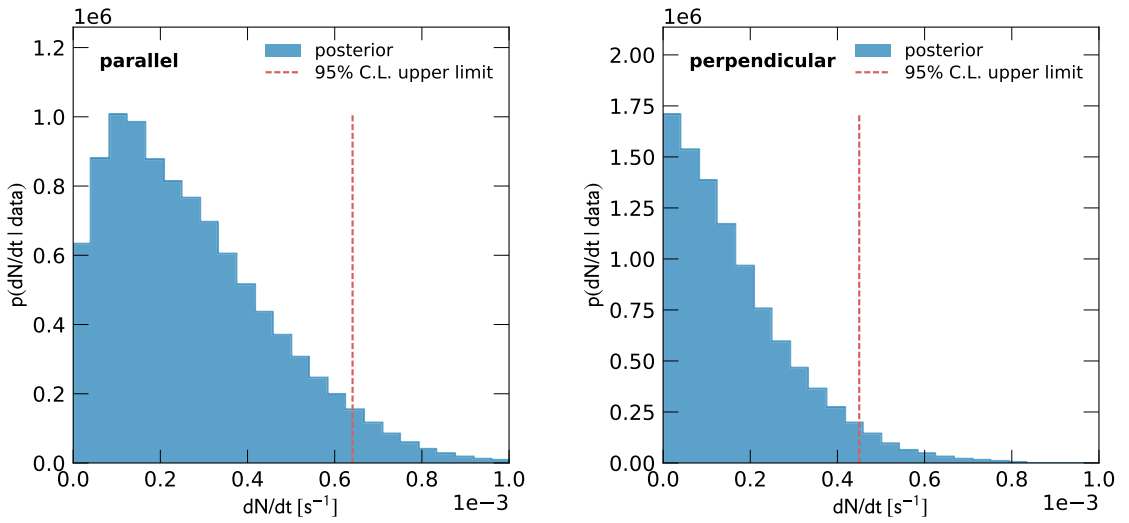
³The choice of the used prior in Bayesian analysis is often a point of contention, as it could influence the resulting posterior distribution in principle. However, in many cases, especially if enough experimental data is available, it can be shown that the result is robust against variations of the prior, like in the case of this analysis.

⁴considering the detection efficiency of the setup

$(0.95 \pm 0.33) \cdot 10^{-3} \text{ s}^{-1}$ in the perpendicular case. Both values have been achieved by fitting a gaussian distribution to the posterior. This consistency check intuitively proves that on one hand the correction and filtering algorithms do not spoil a possible signal contamination, and on the other the Bayesian method correctly reproduces the expected values.

5.2.3 | Results

With the analysis chain prepared and verified, it is now straightforward to infer the actual exclusion limits from the OSQAR LSW runs. The final posterior distributions of the signal count rate are shown in Figure 5.6 with the 95 % upper exclusion limits resulting in $0.64 \cdot 10^{-3} \text{ s}^{-1}$ and $0.45 \cdot 10^{-3} \text{ s}^{-1}$ for parallel and perpendicular polarization respectively.



(a) Parallel polarization.

(b) Perpendicular polarization.

Figure 5.6: Posterior distributions of the signal count rate (blue). The vertical lines (dashed red) mark the excluded value of $\frac{dN}{dt}$ at the 95 % level.

Finally, what is still missing in order to derive exclusion limits on the ALP parameter space is the *detection efficiency* η of the system, i.e. how many photons leaving the second dipole are required on average to produce 1 ADU in the CCD. This number directly relates the excluded signal count rate $\frac{dN}{dt}$ to the excluded rate of reconverted photons $\frac{dN_\gamma}{dt}$ as

$$\frac{dN_\gamma}{dt} = \frac{1}{\eta} \frac{dN}{dt} \quad (5.5)$$

For the detection efficiency of the implemented setup, a value of $\eta = (0.56 \pm 0.02) \frac{\text{ADU}}{\gamma}$ has been measured by [88], including losses due to the exit window of the anticryostat, the focusing lens, and the CCD's entrance window, quantum efficiency and ADC sensitivity. Using this value for the detection efficiency finally yields the exclusion limits on the rate of reconverted photons, as given in Table 5.2.

Table 5.2: Excluded rates of reconverted photons for (pseudo-) scalar ALPs.

ALP chirality	polarization	dN_γ/dt (95 % C.L.)
pseudoscalar	$(\mathbf{e}_\gamma \parallel \mathbf{B}_{\text{ext}})$	$1.1 \cdot 10^{-3} \text{ s}^{-1}$
scalar	$(\mathbf{e}_\gamma \perp \mathbf{B}_{\text{ext}})$	$0.8 \cdot 10^{-3} \text{ s}^{-1}$

Now it is possible to infer exclusion regions in the ALP parameter space by means of Eq. (2.3), as shown in Figure 5.7. The solid and dashed lines depict the 95 % confidence limits

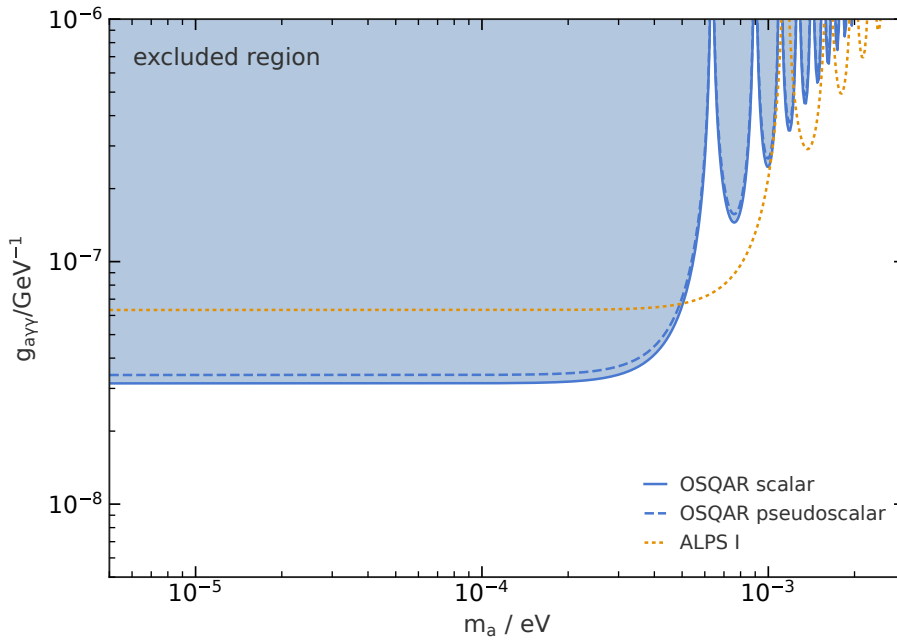


Figure 5.7: Exclusion limits at the 95 % level for scalar (dashed) and pseudoscalar (solid) ALPs. The limits previously established by ALPS I [55] are shown as dotted orange line.

on pseudoscalar and scalar ALPs, excluding the (shaded) parameter space above them. In the so-called *massless limit*, i.e. for $m_a \rightarrow 0$, the lines become flat, as the ALP-photon conversion probability is approximately independent of the ALP mass⁵. In this regime, the excluded ALP-photon coupling constants are $g_{a\gamma\gamma} < 3.5 \cdot 10^{-8} \text{ GeV}^{-1}$ in the pseudoscalar and $g_{a\gamma\gamma} < 3.2 \cdot 10^{-8} \text{ GeV}^{-1}$ in the scalar case. This establishes the most stringent constraints on the ALP-photon coupling ever achieved in LSW experiments.

⁵cf. Eq. (2.3)

6

Results and prospects

It is wrong to think that the task of physics is to find out how nature is. Physics concerns what we can say about nature.

NIELS BOHR

In this chapter, the presented results of the OSQAR experiment will be briefly summarized, and as well a prospect to future developments will be given.

The OSQAR experiment utilizes a classic LSW approach (see Sec. 2.1) to search for scalar and pseudoscalar Axion-Like Particles. In the dataset collected in 2014, no significant excess of signal counts over the background expectation could have been detected, hence constraints on the rate of reconverted photons have been derived (see Tab. 5.2) using a Bayesian method. These constraints have subsequently been used to put exclusion limits on the ALP-photon coupling parameter space resulting in the most stringent limits ever achieved in laboratory ALP searches. For this reason, the OSQAR limits are quoted by the Particle Data Group (PDG) review on “Axions and other similar particles” [4]. The results of this analysis have been published in [89].

As the current implementation of the OSQAR setup is already using state of the art components, there is no straightforward way to improve the sensitivity significantly by only replacing components. This is why elaborating the optical design by means of using a Fabry-Perot cavity (see Sec. 2.1) around the first LHC dipole is currently considered [90] as an upgrade possibility. This would effectively increase the circulating power on the production side improving the sensitivity (cf. Eq. (2.5)) by a factor of $\beta^{\frac{1}{4}}$, where β denotes the power buildup of the cavity. Nevertheless, this clearly comes with its own technical challenges such as locking the cavity with the mirrors being separated by the LHC dipole and keeping it locked bearing the seismic noise in the SM18 hall. After preliminary laboratory studies, the feasibility of this option will be explored in 2017, aiming to have an operational setup in 2018. Another possibility would be to spatially extend the magnetic field, utilizing two LHC dipoles on either side of the optical barrier, which would enhance the sensitivity by a factor 2. However, this comes with the price of huge infrastructure investments in the SM18 hall, which might be inefficient, given the relatively small improvement in sensitivity.

Part III

ALPS II Experiment

7 |

From ALPS I to ALPS II

In general, scientific progress calls for no more than the absorption and elaboration of new ideas.

WERNER HEISENBERG

The ALPS I experiment¹, based at Deutsches Elektron-Synchrotron (DESY) in Hamburg accomplished the quest for searching ALPs with an LSW type setup, resulting in the most constraining limits achieved in laboratory based experiments at that time. This pioneering work was conducted using only a single HERA dipole magnet and meanwhile the OSQAR experiment has reached better sensitivity by incorporating two LHC magnets (see Part II). Nonetheless, the next step of evolution in Light Shining through a Wall setups is currently being prepared, namely the ALPS II experiment. As the successor of ALPS I, the ALPS II setup includes improvements in all aspects of the experiment, allowing for a large gain in sensitivity.

The following Section 7.1 will describe these improvements in more detail, always with a view of contrast to ALPS I, and will summarize the expected sensitivity in the ALP parameter space in Section 7.1.4. The subsequently following Section 7.2 is devoted to the new detector concept, as this will lay the ground for all following chapters of this part.

7.1 | General overview

Around the ALPS II experiment an international collaboration has formed, unifying all expertise needed to realize the experiment. As the time of writing this, there are 22 members from 5 institutes contributing to the project. Like its predecessor, the ALPS II experiment will be deployed at DESY and its first stage² is currently in the commissioning phase.

The following subsections will focus on the three main aspects of every LSW type setup, that are magnets, optics and photon detection. Most of the information given here is described in more details in the ALPS II Technical Design Report (TDR) [54].

¹Any Light Particle Search

²More about the different stages in Section 7.1.4.

7.1.1 | Magnet system

From Eq. (2.5) it is apparent that the parameter having the largest impact on the sensitivity is the *magnetic length*, i.e. the product BL of the magnetic field strength and its length. As already mentioned in the introduction, ALPS I utilized a single HERA dipole magnet featuring a magnetic field of 5 T over a total length of 8.8 m. But, since this magnet was used for both production and regeneration region, the effective magnetic length is halved resulting in 22 T m (see Figure 7.1).

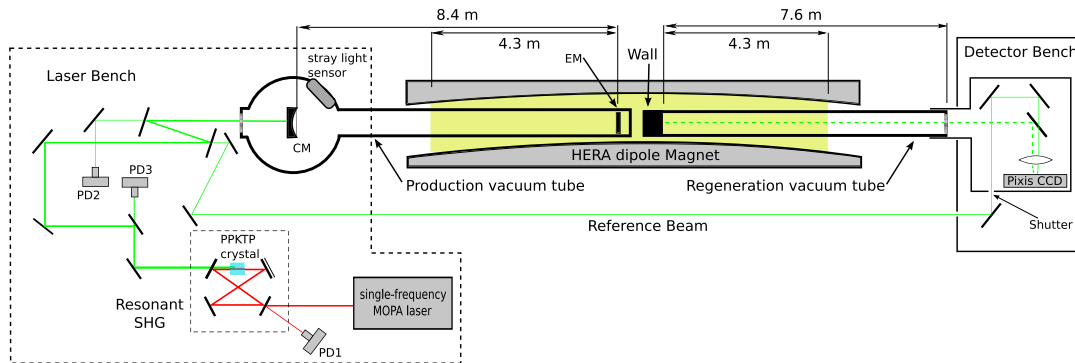


Figure 7.1: Schematic view of the ALPS I setup [55]. The HERA dipole magnet was split into regions for ALP production and regeneration. On the production side, a Fabry-Perot cavity was installed, increasing the circulating power.

ALPS II will again rely on the usage of HERA dipole magnets, since there is a large number of magnets, that have been produced as spare replacements for the HERA accelerator, available to the collaboration. However, instead of using only one of these in ALPS II, the magnetic length is vastly increased by building a string of 10 HERA dipoles on either side of the optical barrier. Further, as has been shown by [91], the HERA dipoles can be safely operated at a field strength of 5.3 T using 5.7 kA of electric current, well below the quench current of about 6 kA. This results in a total magnetic length of 468 T m which is about a factor of 21 larger than compared to ALPS I.

The operation of these 2×10 magnets is foreseen in the HERA accelerator tunnel, having the center of the setup, i.e. the optical barrier, situated in one of the former experiment halls³, while *stretching out* both magnet strings on opposite sides into the tunnel. This has the advantage that all cryogenic support infrastructure necessary to operate the magnets at 4 K is already in place and can be reused after slight modifications. A cross-section of the HERA dipoles is shown in Figure 7.2. The resulting total spatial extent of each of the two magnet strings is about 100 m taking the field free gaps of 0.936 m each between the magnets into account. On these scales, the original purpose of the HERA dipole magnets catches up, which was to guide the beam of protons around the circular accelerator. Although the inner diameter of the vacuum pipe of each dipole magnet is 55 mm, its effective free horizontal aperture is reduced to 35 mm due to the bending. This states a problem for the proposed optics concept of ALPS II implementing high finesse cavities, as will be described in the next section. The free aperture through the magnet

³Currently the point *HERA North*, where the H1 experiment was located, is considered.

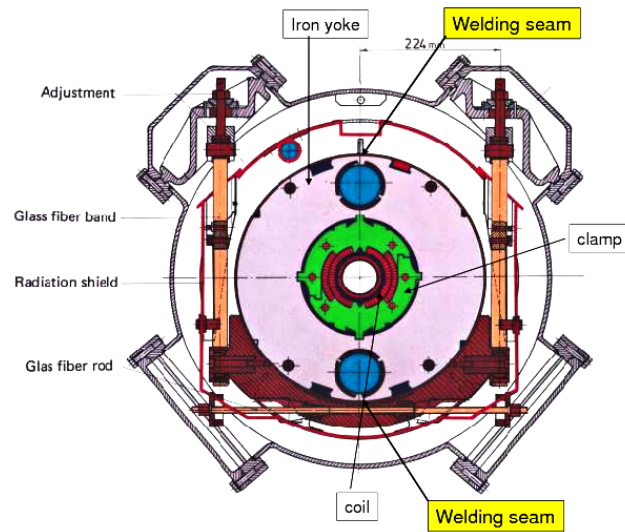


Figure 7.2: Schematic cross-section of a standard HERA dipole magnet. [54]

string limits the achievable power buildup of these cavities and thus is required to be at least 40 mm in order to meet the design specifications [54]. The solution to this issue is to straighten the magnets by using a *brute force* method, which is to apply about 40 kN horizontally on the iron yoke this way deforming the cold mass and the beam pipe. This restores the clear aperture almost fully to a value of 50 mm leaving 10 mm of safety margin for alignment tolerances. Once straightened, the deformation of the cold mass is maintained by inserting so-called *pressure props* between the yoke and vacuum vessel. This procedure has been shown to neither damage the cold mass nor diminish the performance of the magnet.

7.1.2 | Optics concept

The advantage of using resonant Fabry-Perot cavities in LSW experiments has already been motivated in Section 2.1, but as a quick recap, their task is to effectively increase the number of photons, i.e. the circulating power, within the production region in front of the optical barrier, and to enhance the ALP-photon reconversion probability in the regeneration area behind the barrier.

Already in ALPS I, a Production Cavity (PC) was implemented boosting the available input laser power by a power buildup factor of $\beta_{PC} \approx 300$ to 1.2 kW (cf. Fig. 7.1). For ALPS II this scheme is continued implementing a 100 m PC and increasing its power buildup to $\beta_{PC} = 5000$. Likewise, the setup is extended by using another cavity on the regeneration side, this time aiming for a power buildup of $\beta_{RC} = 40000$. The asymmetry in the values of power buildups originates from the fact the cavity end mirrors can only withstand a certain amount of optical power before the reflective coatings get damaged. This is also the reason for operating the experiment at twice the wavelength, compared to ALPS I, namely 1064 nm as these damage thresholds are wavelength dependent. In general, the optical design parameters are subject to a trade-off between the power buildup, the mirror damage thresholds and the available aperture given by the magnet strings.

In addition, there are several technical challenges affiliated with this scheme. First of all, the main laser mode needs to be matched with the eigenmode of the PC. For this purpose, an Electro-Optic Modulator (EOM) is used to imprint phase sidebands to the laser beam, allowing to use the reflected light from the cavity to be analyzed in a Pound-Drever-Hall (PDH) detection scheme [92]. This generates an error signal of the cavity length, which is fed back to the laser oscillator tuning the laser frequency to resonantly match the cavity length. Further, Quadrant Photodiodes (QPDs) are used in combination with Differential Wavefront Sensing (DWS) [93] allowing to monitor the lateral offset and tilt of the laser beam with respect to the PC's optical axis. Likewise an error signal is generated, which is used to adjust the alignment by means of actuating two mirrors on piezoelectric transducers.

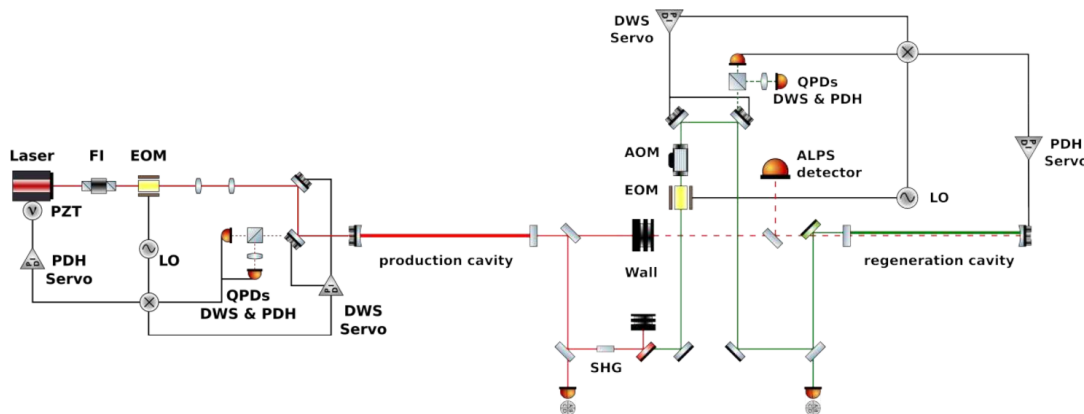


Figure 7.3: Simplified schematic of the ALPS II optics concept including control loops. [54] (Not to scale!)

In between the PC and RC resides the central breadboard — a monolithic ultra flat aluminum plate carrying one mirror of each PC and RC. These mirrors are aligned in parallel, thus defining the *common optical reference axis* of both cavities⁴. In order to keep the RC resonantly locked to the PC mode, the light transmitted from the PC is sent through a non-linear optical crystal producing green light via Second Harmonic Generation (SHG). Next a dichroic mirror separates the remaining red light reflecting it to a beam dump, whereas the green light is transmitted to another EOM again imprinting side bands. Subsequently an Acousto-Optic Modulator (AOM) is used to shift the frequency of the green beam.

The conditioned green beam is sent back and is injected to the RC, effectively bypassing the wall. Here again, a combination of PDH and DWS is implemented to generate error signals of the RC's length and alignment error actuating on the *injection mirrors* and the RC end mirror. However, for this scheme to work, an initial lock of both cavities has to be acquired, which is done by removing the wall, adjusting both cavities relative lateral alignment and tuning the frequency of the green light utilizing the AOM to be resonant with the RC.

Achieving and remaining the locked state and reaching the design performance of the cavities comes with tough requirements on the initial alignment and the control electronics, but “simulations of the optical setup and estimations of the control loop performance indicate

⁴As described in Section 2.1, the effect of resonantly enhanced ALP-photon conversion requires both cavities to be matched on a common mode with maximum spatial overlap.

that all the requirements can be met with state-of-the-art optics, electronics and fabrication processes”[54]. Given the design parameters of the ALPS II optical scheme and considering Eq. (2.5), an overall sensitivity gain of 57 compared to ALPS I is achieved (see Table 7.1).

Table 7.1: Sensitivity gain of ALPS II due the optics related changes compared to ALPS I.

improvement	ALPS II	ALPS I	gain
Laser power / W	30	4	1.7
Laser wavelength / nm	1064	532	1.2
PC power buildup	5000	300	2
RC power buildup	40 000	1	14

As is apparent, the improvements here with the largest impact on the sensitivity are the combined usage of a production and regeneration cavity.

Recently a single 20 m cavity has been setup within the ALPS II laboratory in order to test and characterize the performance of the optical and control systems described above. As a result [94], it was shown that more than 95 % of the incident laser light were coupled into the cavity while all control systems, i.e. frequency stabilization, automatic alignment, and input power stabilization were capable of reducing their respective noise source such that a cavity finesse of more than 3000 was achieved. The system was able to stay in resonance for more than 48 h before the measurement was manually stopped. However, additional losses of about 300 ppm were observed limiting the power buildup of the cavity and requiring further investigation. In summary, the characterization of the individual control loops indicate that the system should allow for a stable resonance condition for the 100 m Production Cavity of ALPS II.

7.1.3 | Single photon detector

While in ALPS I, similar to OSQAR, a CCD has been used to detect possible reconverted photons, this is not the best option for the ALPS II setup. The reason for this is the change of the laser wavelength from 532 nm to 1064 nm. While the former resides in the *visible regime* where CCDs are well suited, their efficiency rapidly drops when increasing the wavelength to the infrared regime, i.e. when the photon energy approaches the band gap of silicon. The typical quantum efficiency of a CCD for 1064 nm photons is of order $\mathcal{O}(0.01)$.

Therefore a different type of photon detector has been chosen for ALPS II, namely a Transition Edge Sensor (TES), to which Section 7.2 is devoted describing the working principle and the installation of a TES in ALPS II. The typical quantum efficiency of a TES itself is close to unity, whereas including losses due to the interface to the rest of the experiment might decrease the overall detection efficiency again to a realistic value of about 0.75. Compared to ALPS I this would state a slight loss of sensitivity with a factor of about 0.96 (cf. Eq. (2.5)). On the other hand, a TES usually features a lower noise rate compared to a CCD, which again improves the sensitivity.

Recently, an alternative approach based on the heterodyne detection of a beat note between the reconverted photon signal and a local oscillator has been proposed and is described in more detail in Appendix A.

7.1.4 | Expected sensitivity

Summarizing all improvements mentioned above, the ALPS II design aims for an increase in sensitivity by more than a factor of 3000 compared to its predecessor ALPS I. Figure 7.4 shows the expected sensitivity of ALPS II in the ALP parameter space.

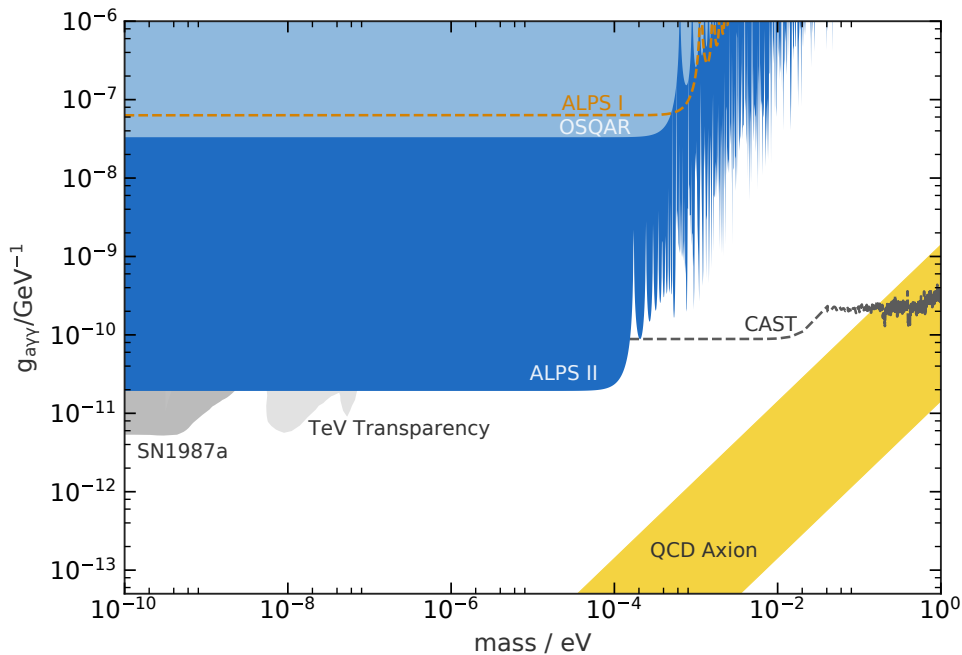


Figure 7.4: Expected sensitivity of ALPS II in the ALP parameter space. (Created using the ALPlot web application, cf. Sec. 2.7)

As can be seen, the design sensitivity of ALPS II easily covers the exclusion limits derived by OSQAR (see Cha. 5) and even surpasses the latest CAST results (see Sec. 2.2). Further, the ALPS II design is sensitive enough to cover most of the domain in parameter space, where the anomalous transparency of the universe for TeV photons (see Sec. 2.5) hints to. Given the available technology and the expertise of the collaboration, ALPS II makes a viable representative of the next evolution step in LSW experiments.

The construction and commissioning of ALPS II is planned to happen in two stages. First, a small scale setup without magnets is envisioned, to demonstrate the feasibility of the optics and detector concept. On a 2×10 m scale the initial alignment and simultaneous locking of production and regeneration cavity will be shown. Further the TES detector is commissioned and its performance investigated. At this stage, a first physics run will be conducted searching for Hidden Photons (HPs) [95, 96, 97] — lightweight hypothetical bosons kinetically mixing with the QED photon. Meanwhile the necessary preparations in the HERA tunnel will be accomplished before the full ALPS II design is deployed in its final stage, including the 2×10 dipoles magnet string, enabling the experiment to search for Axion-Like Particles.

7.2 | Transition Edge Sensor

As already motivated above, the ALPS II design requires a novel detector concept, as standard CCDs are not applicable for 1064 nm photons. The challenge of every LSW type experiment is to be as efficient in detecting signal photons while keeping the noise background, i.e. dark counts not originating from reconverted photons, as low as possible. The reason is that due to the nature of ALPs and their ultra small coupling constant, the expected rate of signal photons is extremely low⁵.

The strived detector concept of ALPS II relies on a Transition Edge Sensor (TES), a cryogenic superconducting micro-calorimeter capable of detecting single photons with high efficiency. This Section will introduce the basic working principle of a TES and briefly presents the current status within ALPS II. The installation and first characterization of the TES based ALPS II detector is covered in great detail in [98] for further reference.

7.2.1 | Working principle

The theoretical framework used here to understand and describe the TES calorimeter response is commonly referred to as *small signal theory* and is greatly worked out in [99].

In a nutshell, a TES consists of a small piece of absorber material cooled down to exactly the temperature where the effect of superconductivity [100] occurs. Right at the transition point between normal conductivity and superconductivity, the absorption of a photon and the associated rise of temperature leads to a tremendous change of the material's electric resistance (see illustration in Figure 7.5), which is subsequently measured.

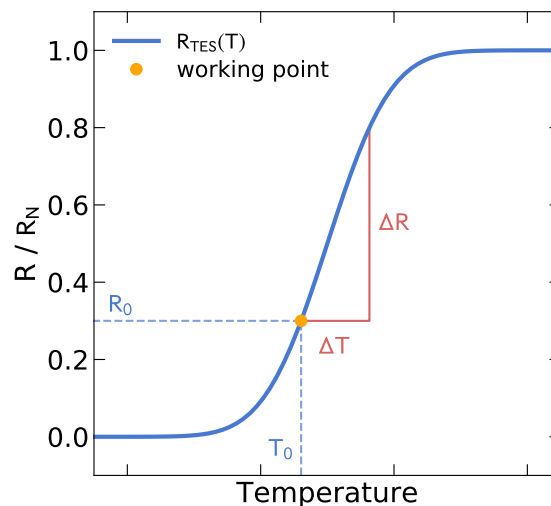


Figure 7.5: Illustrative plot of the *transition edge*. The TES working point resides between normal resistivity R_N and superconductivity. When the temperature increases as a result of photon absorption by ΔT , the TES resistance changes by ΔR . At the working point, the TES has a non-vanishing electrical resistance R_0 .

⁵Compare the excluded rate of reconverted photons by OSQAR in Table 5.2, which is $\mathcal{O}(\text{mHz})$

Usually the TES physical dimensions are chosen to be small, allowing to assume an instantaneous heat-up of the absorber material by $\Delta T = \Delta E/C$, where ΔE denotes the amount of energy absorbed, and C the heat capacity. Since the absorber is connected to a thermal bath for cooling via a thermal link G , the temperature and thus the TES resistance relaxes again after heat-up, given the exponential time constant $\tau = C/G$.

In order to set the TES to its working point within the transition edge, a bias circuit I_b limited by a shunt resistor R_{sh} is used, allowing much finer tuning capabilities, compared to naively adjusting the thermal bath temperature instead. The bias current induces joule heating in the TES, which, in the state of equilibrium, just cancels with the heat flow to the thermal bath resulting in a constant temperature, i.e. $\frac{dT}{dt} = 0$. However, when the temperature increases as consequence of a photon absorption, the TES resistance rises, which immediately leads to a decrease of the joule heating power. This in turn relaxes the TES back to the equilibrium state and is called *electro-thermal feedback*.

The full *thermal differential equation* of the TES reads

$$C \frac{dT}{dt} = -P_{\text{bath}} + P_{\text{bias}} + P_{\gamma} \tag{7.1}$$

where P_{γ} denotes additional power load due to incident photons. A typical operation circuit is shown in Figure 7.6.

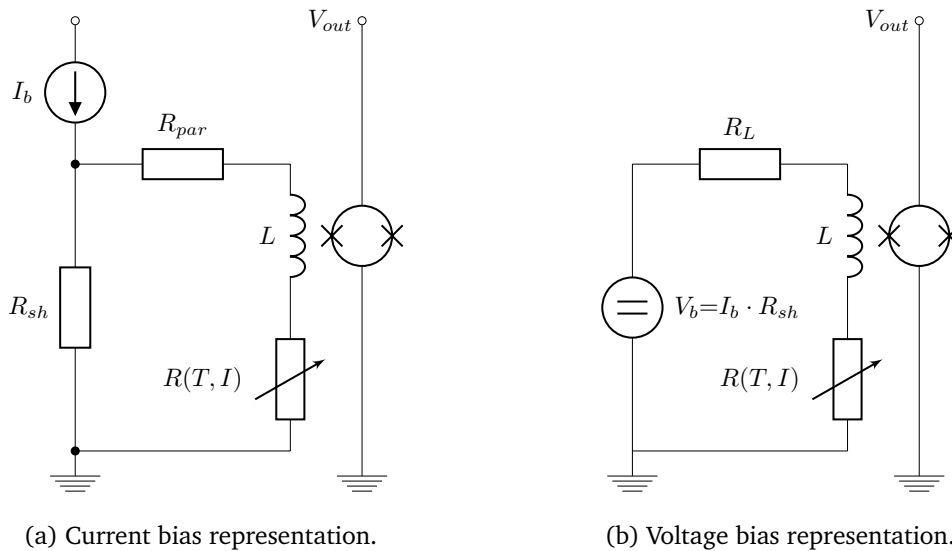


Figure 7.6: Equivalent representations (Thevenin-Theorem [101]) of the electric circuit used to operate a TES in biased mode. $R(T, I)$ denotes the current and temperature dependent resistance of the TES.

The TES circuit further includes an inductance L used to *read* the change of current and thus the associated change of resistance by an ultra sensitive magnetometer, i.e. a Superconducting Quantum Interference Device (SQUID) [102]. The inductance itself comes with a parasitic resistance R_{par} due to possible non-superconducting parts in the circuitry. While the scheme in Fig. 7.6a is the most widely realized one, the scheme of Fig. 7.6b is more intuitively used

in calculations. However, as can easily be shown from the Thevenin-Theorem [101], both representations are equivalent.

Analog to Eq. (7.1), an electrical differential equation of the TES can be formulated. Looking at Figure 7.6b, one obtains from Kirchhoff's law

$$L \frac{dI}{dt} = I_b R_{sh} - IR_L - IR(T, I) \quad (7.2)$$

where $R_L = R_{sh} + R_{par}$ is the combined non-TES related resistance of the circuit. These two non-linear (coupled) differential equations (7.1) and (7.2) fully describe the TES response in the most general way. However, in order to find analytic solutions, further assumptions are required in order to linearize them.

Describing the steady working point state by quantities R_0 , T_0 and I_0 , a small signal⁶ only induces small deviations from this state, e.g. $T_0 + \delta T$ or $I_0 + \delta I$. The TES resistance then reads

$$R(T, I) \approx R_0 + \left. \frac{\partial R}{\partial T} \right|_{I_0} \delta T + \left. \frac{\partial R}{\partial I} \right|_{T_0} \delta I \quad (7.3)$$

$$\approx R_0 + \underbrace{\frac{T_0}{R_0} \left. \frac{\partial R}{\partial T} \right|_{I_0}}_{=: \alpha} \frac{R_0}{T_0} \delta T + \underbrace{\frac{I_0}{R_0} \left. \frac{\partial R}{\partial I} \right|_{T_0}}_{=: \beta} \frac{R_0}{I_0} \delta I \quad (7.4)$$

Thereby, the dimensionless coefficient α denotes the system's *temperature sensitivity*, i.e. the steepness of the transition edge in Fig. 7.5, whereas β denotes the analog quantity representing the systems *current sensitivity*. Using these particular simplifications the linearized (small signal) version of the systems differential equations can be obtained as follows

$$\frac{d}{dt} \begin{pmatrix} \delta I \\ \delta T \end{pmatrix} = - \begin{pmatrix} \frac{R_L + R_0(1+\beta)}{L} & \frac{I_0 R_0 \alpha}{L T_0} \\ \frac{-I_0 R_0(2+\beta)}{C} & \frac{I_0^2 R_0 \alpha - T_0 G}{T_0 C} \end{pmatrix} \begin{pmatrix} \delta I \\ \delta T \end{pmatrix} + \begin{pmatrix} \frac{\delta V}{L} \\ \frac{\delta P_\gamma}{C} \end{pmatrix} \quad (7.5)$$

This states a linear system of coupled inhomogeneous differential equations. One way to solve this goes along the line of diagonalizing (7.5) for $\delta V = 0$ and $\delta P_\gamma = 0$, thus obtaining the general solution for the homogeneous case, and subsequently adding a particular solution of the inhomogeneous case, which however will not be carried out in this thesis. Rather, an interesting special case will be presented, namely the already mentioned instantaneous heat-up by photon absorption at $t = 0$. For all times $t > 0$ the temperature and current equations then read

$$\delta T(t) = \left[(\tau_I^{-1} - \tau_-^{-1}) e^{-t/\tau_+} - (\tau_I^{-1} - \tau_+^{-1}) e^{-t/\tau_-} \right] \frac{\Delta E / C}{\tau_+^{-1} - \tau_-^{-1}} \quad (7.6)$$

$$\delta I(t) = \left(\frac{\tau_I}{\tau_+} - 1 \right) \left(\frac{\tau_I}{\tau_-} - 1 \right) \frac{\Delta E}{(2 + \beta) I_0 R_0 \tau_I^2} \frac{(e^{-t/\tau_+} - e^{-t/\tau_-})}{(\tau_+^{-1} - \tau_-^{-1})} \quad (7.7)$$

⁶Hence the name *small signal theory*

where the following time constants have conventionally been introduced

$$\frac{1}{\tau_{\pm}} = \frac{R_L + R_0(1 + \beta)}{2L} + \frac{1}{2\tau_I} \pm \frac{1}{2} \sqrt{\left(\frac{R_L + R_0(1 + \beta)}{L} - \frac{1}{\tau_I}\right)^2 - \frac{4\alpha(2 + \beta)I_0^2 R_0^2}{T_0 LC}} \quad (7.8)$$

$$\frac{1}{\tau_I} = \frac{G}{C} - \frac{\alpha I_0^2 R_0}{T_0 C} \quad (7.9)$$

When recording signals using the scheme depicted in Figure 7.6, the interesting Equation to describe the resulting waveform is Eq. (7.7) of which Figure 7.7 shows the qualitative behavior.

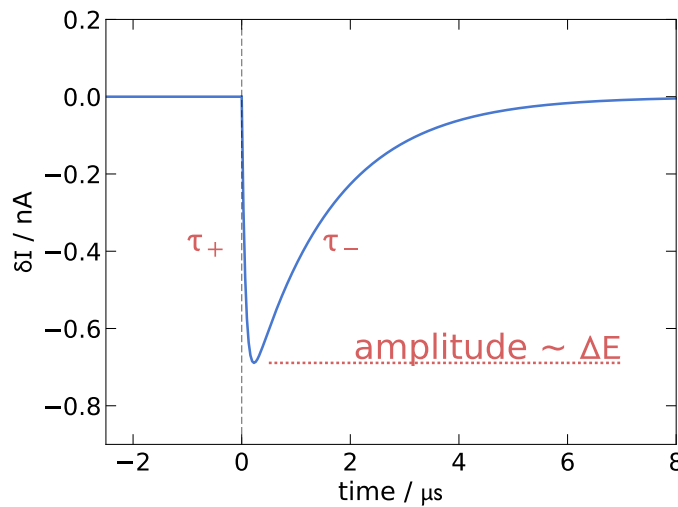


Figure 7.7: TES current response as given by Eq. (7.7).

The time constants τ_+ and τ_- can be identified with the *rise-* and *fall-times* of the exponential functions governing the TES response. Further, the amplitude of the (negative) signal peak is proportional to the original photon energy, as can be read off from Eq. (7.7), thus allowing to use the TES not only as single photon detector, but also as calorimeter.

7.2.2 | Current Status

For the ALPS II experiment a tungsten (W) based TES detector from the National Institute of Standards and Technology (NIST) is used, with a small film of tungsten being the absorber and the resistive part of the TES at the same time. The tungsten film is of size $25 \mu\text{m} \times 25 \mu\text{m} \times 20 \text{nm}$ and is deposited within an optical stack optimizing the transmission for 1064 nm photons (see Figure 7.8).

The whole stack resides on a silicon substrate paddle, with the TES being in the center of the *disc* (cf. Figure 7.9a). The substrate paddle is mounted to a copper support structure, not only providing the thermal link to the cooling system (see below), but also carrying a sleeve of zirconia, allowing to easily connect an optical fiber to the TES in a plug-and-play fashion. The sleeve accepts standard ferrule terminated optical single mode fibers as commonly used in e.g.

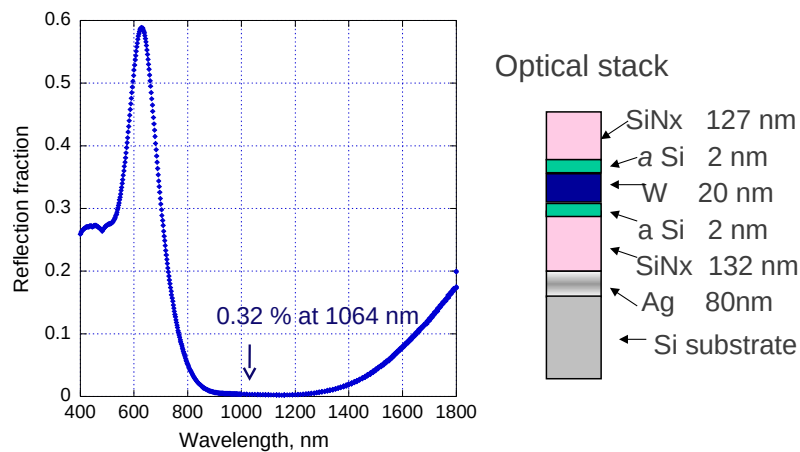


Figure 7.8: Optical stack of the NIST TES optimized for the transmission of 1064 nm photons. Left: Plot of the stacks reflection coefficient. Right: Materials and thicknesses of the stack layers. [98, 103]

telecommunication applications⁷ and ensures that the fiber core (typical diameter $< 10 \mu\text{m}$) is kept in the substrate disc's center above the TES. Due to the precise manufacturing process the resulting off-center misalignment error has shown to be only $3.1 \mu\text{m}$ on average resulting in 0.1 % fiber-to-chip coupling losses at maximum [104].

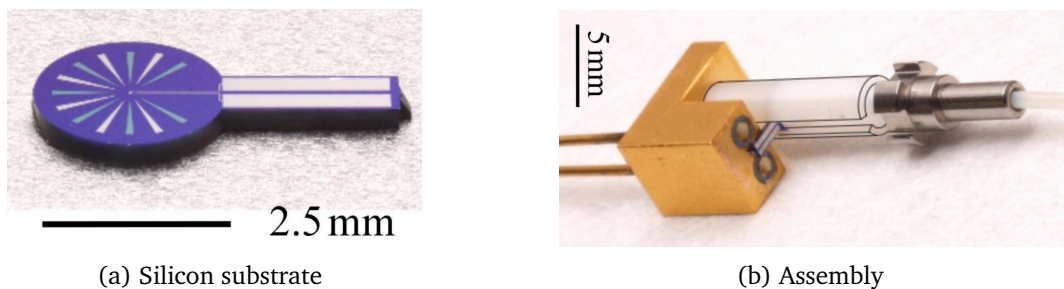


Figure 7.9: **(a)** Silicon substrate (blue) carrying the optical stack with the tungsten film in the center of the disc, i.e. where the arrows point to. **(b)** TES detector module assembly with the support structure made of copper and the zirconia sleeve (white) aligning the optical fiber to the substrate center, where the TES resides. [104]

The TES electrical setup and in particular the SQUID based readout system has been developed and added to the ALPS II detector module by the Physikalisch-Technische Bundesanstalt (PTB) in Berlin. The TES circuit inductance (see Figure 7.6) is interfaced by a single front-end SQUID and is subsequently amplified using a linear array of 16 SQUIDS in series [105].

In order to create the necessary cryogenic environment for the TES and the SQUIDS, an Adiabatic Demagnetization Refrigerator (ADR) by Entropy⁸ has been used up to now⁹. The working principle relies on the magnetocaloric effect in solid materials [106] exposed to strong

⁷A more detailed description on optical single mode fibers is given in Section 8.1

⁸Entropy GmbH, Gmunder Str. 37a D-81379 München

⁹Due to unforeseen personnel restructuring, the ADR system used in ALPS II is no longer available to the collaboration. As of today, a compatible replacement is in the process of procurement. (Author's note)

magnetic fields. In the used Entropy ADR this is realized by Gadolinium Gallium Garnet (GGG) and Ferric Ammonium Alum (FAA) contained in so-called salt pills within a 6 T superconducting solenoid magnet. The magnet is mounted to the 4 K-stage, which is cooled using a pulse tube cooler. A schematic cross-section view of the Entropy ADR is shown in Figure 7.10.

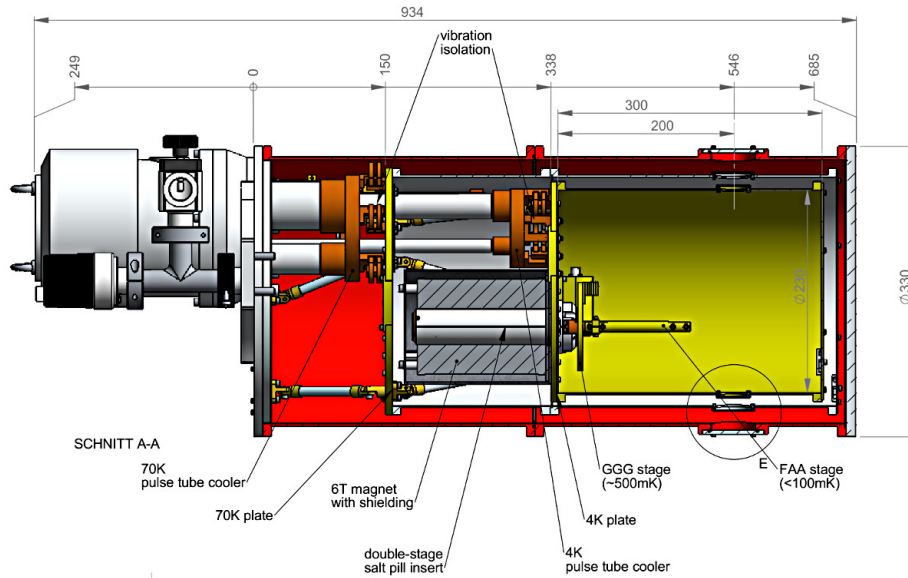


Figure 7.10: Schematic cross-section of the ADR from Entropy. [98]

The actual refrigeration cycle starts with ramping up the magnetic field, forcing all atomic spins in the salt pills to align in parallel. Due to the conservation of energy, this adiabatic magnetization process results in a heat up of the system for the time being. However, while maintaining the magnetic field, the system is again cooled down (externally using the pulse tube cooler), thus the additional heat is removed. At the end of this step, the salt pills are back at the baseline temperature but with the atomic spins still aligned with the magnetic field. Next, the salt pills are decoupled from the rest of the system and the magnetic field is ramped down allowing the atomic spins to reorientate, naturally increasing the systems (magnetic) entropy. Thereby, (thermal) energy is required resulting in an effective cooling of the system.

With this technique, the FAA stage (cf. Fig. 7.10), where the TES detector module is mounted to, is cooled down to temperatures below 100 mK. The working point chosen for the ALPS II detector module is about 80 mK and has been motivated in [98].

As already mentioned in footnote ⁹ of this chapter, the ALPS II cryostat system is currently being replaced. The successor of the previously used ADR is most likely to be a *Dilution Refrigerator*, offering several advantages over the usage of an ADR, such as constant operation in cold state, i.e. no need for refrigeration cycles as described above. However, as the detector module will stay the same, the following developments and results of this thesis are independent on the actual cryostat system and thus are still fully applicable to the next generation of cooling system.

8

Signal photon coupling

Nothing in life is to be feared, it is only to be understood.

MARIE CURIE

A crucial part in the chain of guiding reconverted photons from the RC to the TES involves the coupling of a light beam as thick as a human thumb ($\varnothing \sim \text{mm}$) into the core of a Single Mode Fiber with a diameter smaller than a human hair ($\varnothing \sim \mu\text{m}$). The design, implementation and testing of an optical setup realizing this technical challenging task is the topic of this chapter.

Section 8.1 will start off with some basics about gaussian beam optics defining common beam characteristics such as width and divergence and introduces the concept of light guiding optical fibers. The subsequent Section 8.2 will then focus on an experimental method of measuring these properties, in particular for beams of extreme size as mentioned above, and the design and construction of a device for this purpose. After that in Section 8.3, the actual coupling setup is presented and explained before Section 8.4 concludes with the achieved coupling efficiency and stability.

8.1 | Gaussian beam theory

Before going into the details of the coupling setup, it is rewarding to introduce some basic concepts of gaussian beam optics and light propagation.¹

Wave optics serving as classical theory of light intermediate between simple geometric (ray) optics and the more general electromagnetic or even quantum optics, is mainly used when a scalar wave theory² is enough to describe the observed phenomena. *Gaussian optics* in particular is a special case within wave optics used when light beams fulfill the so-called *paraxial approximation*, that is, when the wavefront normals enclose only a small angle with the propagation axis.

¹For a more detailed introduction to this topic consult a standard text book, e.g. [107]

²in contrast to the electromagnetic description of two coupled vectors

In this approximation when solving the general wave equation

$$\nabla^2 U(\mathbf{r}, t) - \frac{1}{c^2} \frac{\partial^2 U(\mathbf{r}, t)}{\partial t^2} = 0 \quad (8.1)$$

with a complex wave function $U(\mathbf{r}, t) = U(\mathbf{r}) \exp(2\pi i \nu t)$ separating time from spatial coordinates, one finds the *paraxial Helmholtz equation*

$$\nabla_t^2 A(\mathbf{r}) - i2k \frac{\partial A(\mathbf{r})}{\partial z} = 0 \quad \text{with} \quad \nabla_t^2 = \frac{\partial^2}{\partial x^2} + \frac{\partial^2}{\partial y^2} \quad (8.2)$$

where $A(\mathbf{r})$ depicts the complex amplitude of $U(\mathbf{r}) = A(\mathbf{r}) \exp(-ikz)$ and $k = 2\pi/\lambda$ is the wave number. As can easily be shown, one important solution to (8.2) is the *gaussian beam* with complex amplitude

$$U(\mathbf{r}) = A_0 \frac{w_0}{w(z)} \exp\left(-\frac{x^2 + y^2}{w^2(z)}\right) \exp\left(-ikz - ik \frac{x^2 + y^2}{2R(z)} + i \tan^{-1} \frac{z}{z_R}\right) \quad (8.3)$$

in which the following expressions have been conventionally introduced:

$$w(z) = w_0 \sqrt{1 + \frac{z^2}{z_R^2}} \quad (8.4)$$

$$R(z) = z \left(1 + \frac{z_R^2}{z^2}\right) \quad (8.5)$$

Thereby z_R is termed *Rayleigh Range* and is related to w_0 by $z_R = w_0^2 \pi / \lambda$ leaving A_0 and w_0 as the only free parameters of (8.3).

For a given value of z , i.e. a particular position along the propagation axis, it becomes apparent why this is called the *gaussian beam* solution when looking at the resulting intensity profile

$$I(\mathbf{r}) = |U(\mathbf{r})|^2 = I_0 \left(\frac{w_0}{w(z)}\right)^2 \exp\left(-\frac{2(x^2 + y^2)}{w^2(z)}\right) \quad (8.6)$$

This represents a 2-dimensional gaussian distribution in the transversal plane as illustrated in Fig. 8.1a. One common way to define the beams width in this plane is taking the radius of the intensity profile where its value drops to $1/e^2 = 0.135$ of the maximum. As can be read of from Eq. (8.6) the variation of the beam width along the z -axis is given by $w(z)$ with its global minimum at $w(z = 0) = w_0$ called the *beam waist* (see Fig. 8.1b). For values $|z| \gg 0$, i.e. far away from the beam waist, this variation can be approximated by a straight line:

$$w(z) \underset{(|z| \gg 0)}{\approx} \frac{w_0}{z_0} z = \theta z \quad (8.7)$$

In the last expression the *divergence angle* θ has been introduced (cf. Fig. 8.1b), that can be directly related to the wavelength by $\theta = \lambda / \pi w_0$.

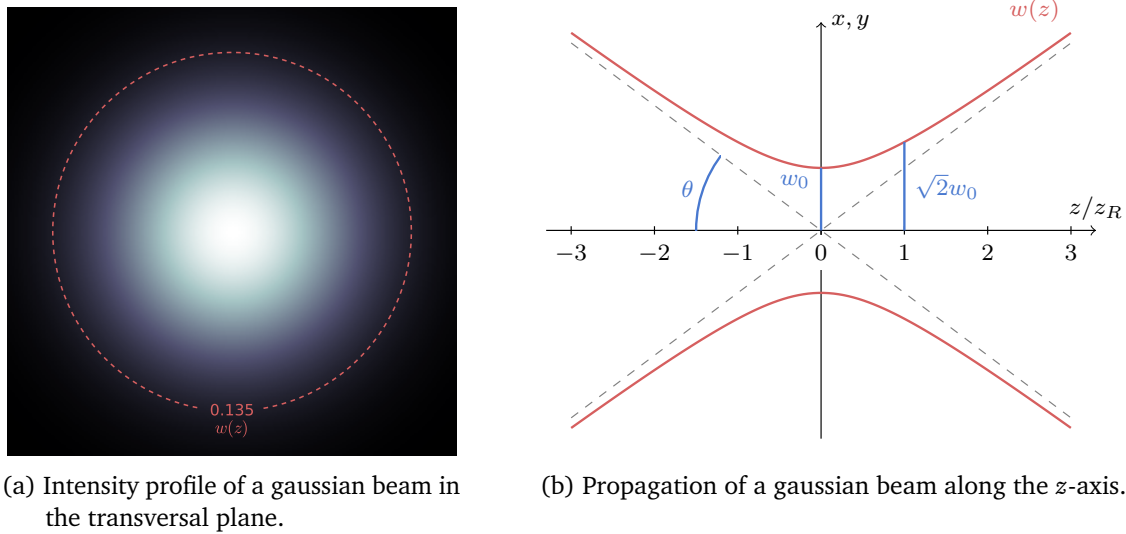


Figure 8.1: Gaussian beam profile and propagation. The red lines indicate the beam width as defined on the intensities $1/e^2$ contour.

Summarizing the above, the full beam geometry can be determined by fixing the waist size and the wavelength. In particular Eq. (8.7) implies for a fixed wavelength that tightly focused beams (small waist size) result in a large divergence angle, as opposed to collimated beams which require large waist sizes.

It should be noted that *the Gaussian beam* is not the only solution to the paraxial Helmholtz equation (8.2). In fact, one can find complete sets of solutions into which any beam can be decomposed. Two prominent examples of those sets are the *Hermite-Gauss-Modes* and the *Laguerre-Gauss-Modes*. Figure 8.2 exemplarily shows the intensity profiles for two members of each of these sets.

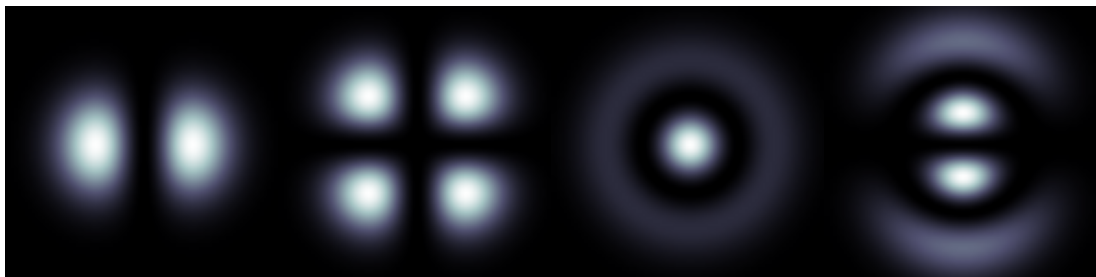


Figure 8.2: Examples of higher order modes in the Hermite-Gauss (left-hand side) and the Laguerre-Gauss (right-hand side) set of modes.

In the case of optical waveguides and Single Mode Fibers (SMFs) in particular, one has to cope with boundary conditions when solving the Helmholtz equation, such as the distinct refractive indices of the fiber core (n_1) and cladding (n_2). Figure 8.3a sketches the basic structure of an SMF³. The solutions in this special case can be expressed analytically using Bessel

³Note that only *step-index* fibers are considered here as they are used in the TES setup

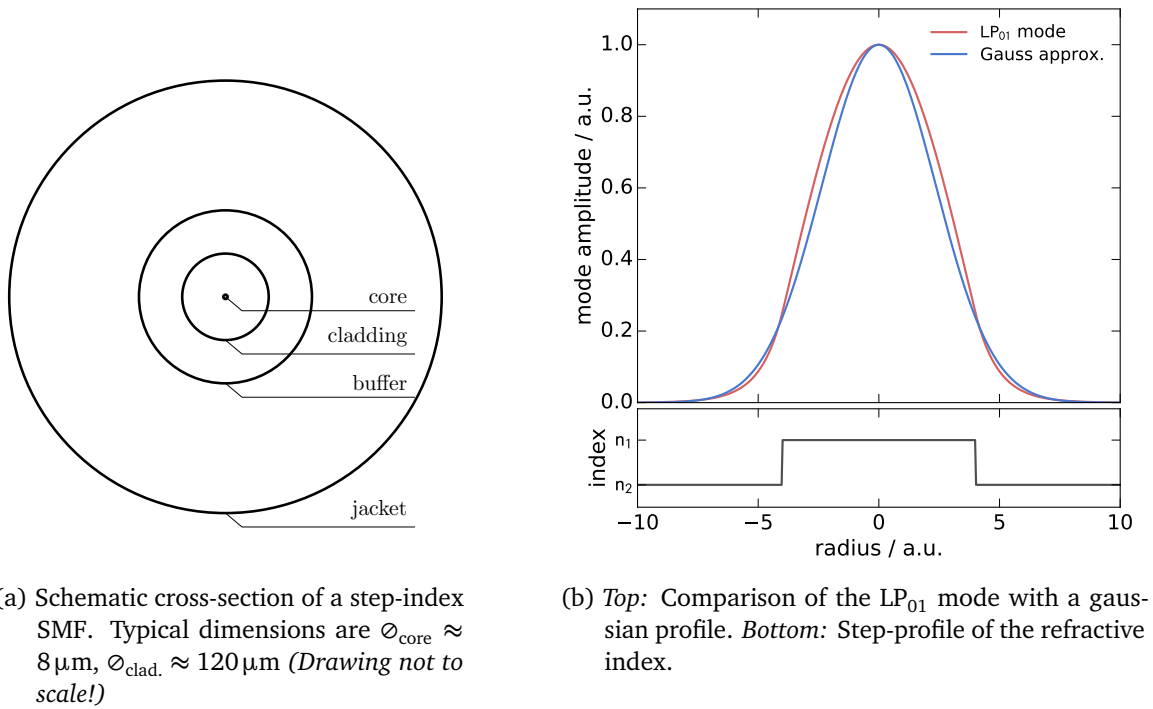


Figure 8.3: Cross-section and mode field distribution of a step-index SMF.

functions [108]. Depending on the wavelength, the size of the core and difference in refractive index between core and cladding, only certain modes are allowed to propagate through the fiber, which can be used to decompose any allowed field configuration. Further it is possible to choose the core size and the refractive indices such that for a given wavelength only a single mode is allowed, hence the name Single Mode Fiber. This (lowest-order) mode is labeled LP_{01} and has a similar radial distribution to that of a gaussian beam (see Fig. 8.3b). Note that this approximation is adequate for most SMF applications and will be assumed for the rest of this thesis.

8.2 | Beam parameter measurement and the Knife-Edge method

After laying out the basics of gaussian beams, this section now deals with the experimental challenge of measuring the beam geometry, in particular its width and divergence. As will become clear in the following section, having this ability comes as requirement when building the signal photon coupling setup.

The probably most straightforward approach to this is measuring the intensity profile directly (at different position along the beams propagation axis) and inferring the beam width from the resulting 2D distributions. For this purpose a standard CCD with well-known geometry can be used. However, it is obvious that this method is only applicable in situations where the expected beam size is neither too large compared to the extent of the CCD's active area, nor too small compared to the pixel size typically of order $\varnothing(10 \mu\text{m})$.

In the context of the desired signal photon coupling, actually both of these cases occur. On one side, the beam leaving the RC (cf. Sec. 7) will have a diameter⁴ of about 8 mm whereas the target fiber on the other side has a mode field diameter of only about 6 μm . To overcome the drawbacks of a CCD in this situation a dedicated device implementing the so-called *knife-edge method* has been designed and built during this thesis.

The basic idea behind this method is to move a sharp edge, for instance a razor blade, gradually *through* the beam, perpendicular to the propagation axis, while a photometer records the amount of light still passing the device. Mathematically this is equal to evaluating the integral

$$\int_{-\infty}^x dx' \int_{-\infty}^{\infty} dy I(x', y) = \frac{P_0}{2} \left(1 + \operatorname{erf} \left[\frac{\sqrt{2}x}{w} \right] \right) =: P(x) \quad (8.8)$$

using Eq. (8.6) for the gaussian beams intensity distribution⁵. From the recorded power distribution $P(x)$ one can now infer the beam width by either fitting Eq. (8.8) or by localizing the 10% and 90% power levels [109] and scaling their distance using the percent-point function of the normal distribution (cf. Fig. 8.4). Although in both cases a gaussian beam shape is implicitly assumed, the latter one is more robust against deviations from that shape.

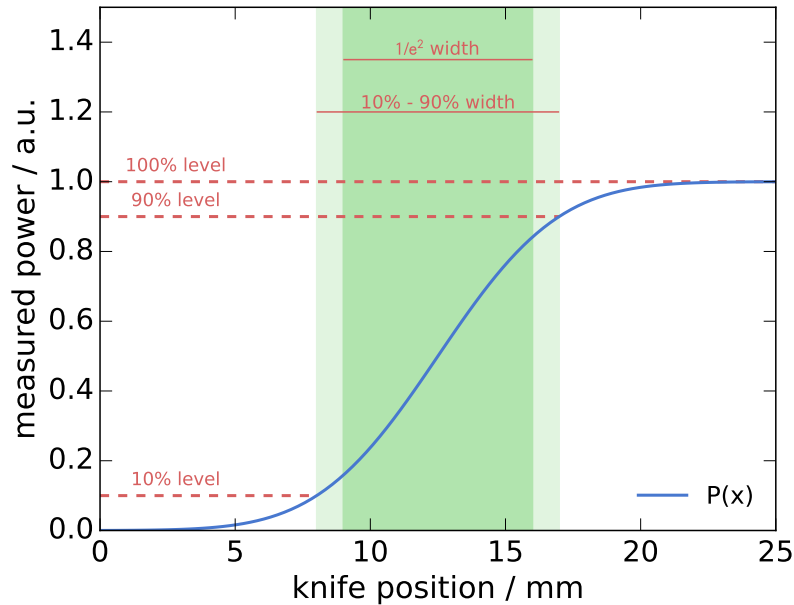


Figure 8.4: Plot of an exemplary power distribution for a perfect gaussian beam.

The device that has been designed and built for this purpose is shown as rendered image in Fig. 8.5. It basically consists of three movable stages⁶ (as indicated by the red arrows) and a pair of perpendicularly assembled razor blades. When the base plate of the device is properly

⁴Note that for the rest of this thesis, statements about beam sizes will always refer to the $1/e^2$ intensity contour as defined in Sec. 8.1

⁵ $\operatorname{erf}(x) = \frac{2}{\sqrt{\pi}} \int_0^x e^{-t^2} dt$ is the so called *error function*

⁶One Thorlabs MTS50 and two Thorlabs Z825B motorized stages

aligned in parallel to the beam propagation axis, the upper two stages (actuating in the plane normal to that) can move the blades either horizontally or vertically into the beam as is desired⁷. The bottom stage is then used to shift the measurement plane along the beams propagation axis enabling the measurement of the divergence angle. The minimum step size of all stages is smaller than $0.1\ \mu\text{m}$ whereas the total travel distance is 25 mm for both lateral and 50 mm for the longitudinal stage. Hence the device is well suited to resolve beam widths in the given context.

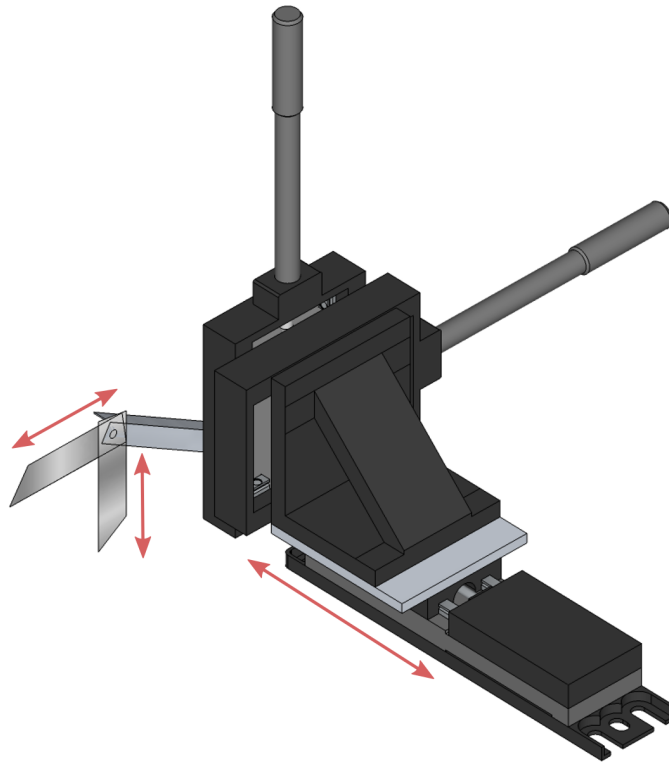


Figure 8.5: Render view of the Knife-Edge beam profiling device. The red arrows indicate the possible directions of motion.

Behind the device, a silicon photodiode⁸ is used to measure the power passing the knife. In order to reduce noise and artifacts from ambient stray light, the photodiode has been equipped with a Schott RG850 effectively filtering all visible and UV radiation below 850 nm. While the stage controllers are already shipped with an USB interface for communication, the photodiodes (analog) signal is digitized and serialized using an Arduino Uno⁹ microcontroller board connected via USB.

On the software side, the stage controllers implement the Thorlabs APT[™] protocol, for which a PYTHON3 module has been ported¹⁰ to be used by the acquisition and control software¹¹ also entirely written in PYTHON3. The latter provides smart measurement routines and a Graphical

⁷Note that in general the beam might not expose perfect radial symmetry, which is why both directions are supported

⁸Thorlabs DET100A — Si Detector, 350 nm to 1100 nm

⁹<https://www.arduino.cc/en/Main/ArduinoBoardUno>

¹⁰<https://gitlab.com/weinshec/pyAPT>

¹¹<https://gitlab.com/weinshec/KnifeEdge>

User Interface (GUI) allowing the perform a full measurement of the beam width and divergence implementing both methods, i.e. fitting of Eq. (8.8) and the $w_{10\%-90\%}$ estimation, as described above. All acquired (raw) data can also be exported in `.csv` format, if further processing or analysis is desired.

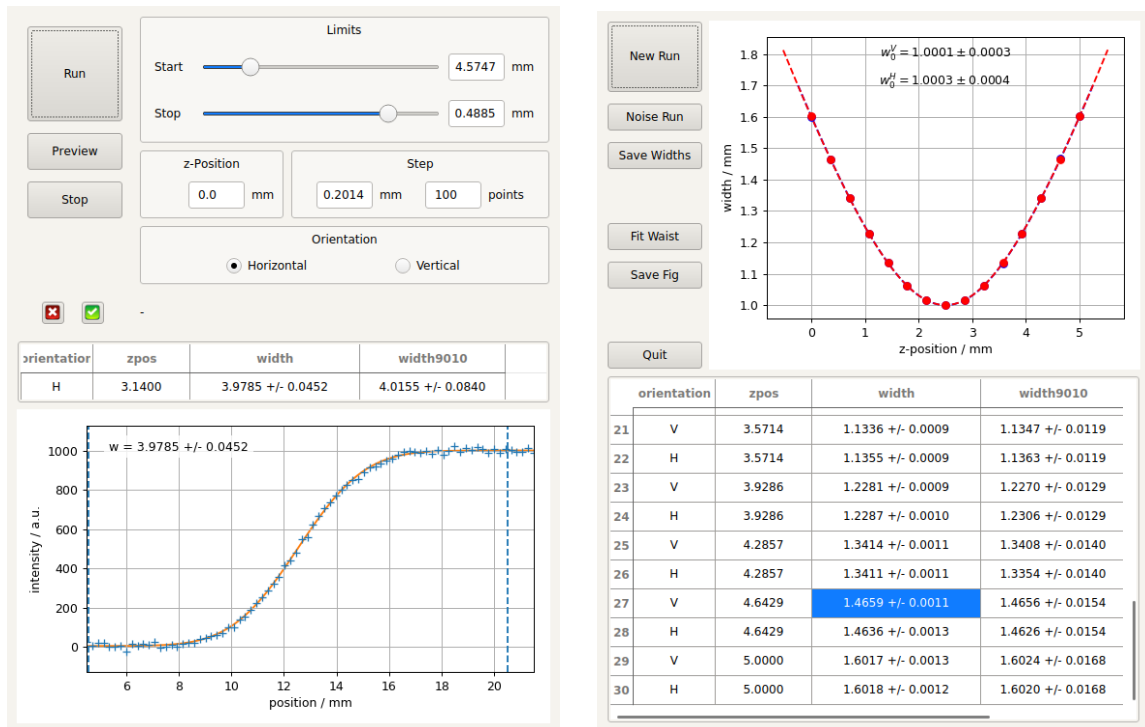


Figure 8.6: Screenshots of the Knife-Edge acquisition and control software GUI.

A user config file allows to identify the used stages by serial number and type and leaves the possibility to provide stage-specific scale corrections for individual calibration. Although the Thorlabs stages ship with preset internal calibration factors, it is usually worth to doublecheck them, as can be seen from Figure 8.7. For the determination of the physical position a caliper gauge with 0.02 mm precision has been used and the resulting scale corrections for all stages turn out to be in the order of a few per mill.

In order to verify the calibration of the device a comparison measurement with a commercially available CCD-based beam profiler (DataRay Inc. WinCamD) has been conducted using the (attenuated) beam of the Production Cavity for reference. The results are shown in Fig. 8.8 and endorse a good agreement between both devices. The uncertainties shown in this plot are of statistical nature only in case of the WinCam measurements, and include scale calibration systematics in the case of the KnifeEdge measurement.

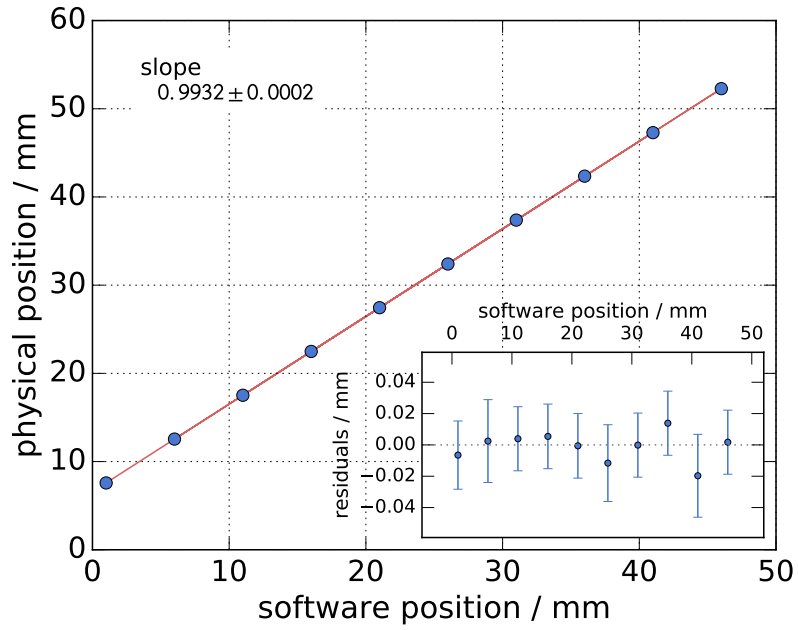


Figure 8.7: Calibration of the Thorlabs MTS50 motorized stage correcting the internal (software) scale for the actual (physical) position.

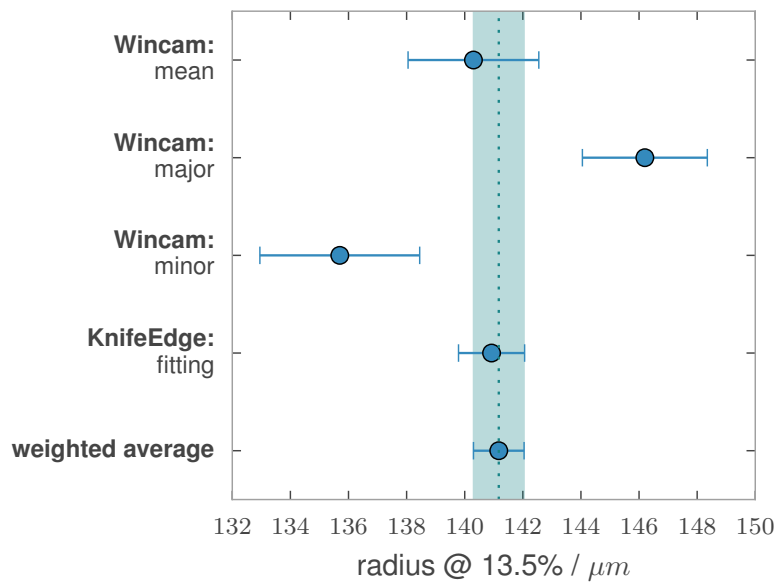


Figure 8.8: Comparison measurement between the Knife-Edge device and a commercial beam profiler (WinCam). The upper three measurements are the result of three different algorithms used by the WinCam.

8.3 | Free-Space-To-Fiber-Coupling setup

The beam of reconverted photons leaving the Regeneration Cavity (RC) needs to be guided to the active area of the TES down in the cryostat, in order to be detected. This path of optical guidance can be divided into two main parts. Starting from the RC side the beam leaves the vacuum system into free space and enters an optical single-mode fiber. The fiber then leads the way into the cryostat guiding the photons through the several cooling stages (cf. Section 7.2) until it reaches the TES. While the latter part, i.e. the coupling between the fiber and the TES is already well covered by [104], the coupling of the free space beam into the fiber needs to be implemented and will be described below.

For an efficient coupling to the Single Mode Fiber, the free space beam needs to be focused on the fiber tip, more specifically the fiber core, which is about three orders of magnitude smaller compared to the beam size. The resulting coupling efficiency then depends on the matching between the (focused) incoming beam and the allowed fiber mode (cf. Sec. 8.1). In general this can be calculated theoretically by evaluating the *overlap integral*:

$$\eta = \frac{|\int dA E_0(x, y) E_1(x, y)|^2}{\int dA |E_0(x, y)|^2 \cdot \int dA |E_1(x, y)|^2} \quad (8.9)$$

The $E_i(x, y)$ hereby denote the field amplitudes of the incoming and target beam respectively. Assuming the gaussian approximation for the fiber mode¹² Eq. (8.9) evaluates to

$$\eta_0 = \left| \sqrt{\frac{2}{\pi w_0^2}} \sqrt{\frac{2}{\pi w_1^2}} \iint dx dy \exp\left[-\frac{x^2 + y^2}{w_0^2}\right] \exp\left[-\frac{x^2 + y^2}{w_1^2}\right] \right|^2 \quad (8.10)$$

$$= \frac{4w_0^2 w_1^2}{(w_0^2 + w_1^2)^2} \quad (8.11)$$

As can easily be seen, for perfectly matching beams, i.e. $w_0 = w_1$, the efficiency reaches unity, whereas for beams of different widths, the efficiency quickly drops¹³. Nevertheless, even for perfectly matching beam sizes, the coupling efficiency can be limited by the relative alignment of the incoming beam to the target mode. The following list covers all degrees of freedom that possibly lead to a reduced efficiency and illustrates their occurrence in the given setup.

Longitudinal displacement The beam waist positions exhibit a non-zero offset along the beam propagation axis, i.e. the focal spot of the incoming beam does not coincide with the fiber tip. Quantifying this offset by Δ_z Eq. (8.9) evaluates to

$$\eta = \frac{4\pi^2 w_0^2 w_1^2 (\Delta_z^2 \lambda^2 + \pi^2 w_0^4)}{(\Delta_z^2 \lambda^2 + \pi^2 w_0^4 + \pi^2 w_0^2 w_1^2)^2} \quad (8.12)$$

¹²see Sec. 8.1

¹³It might seem counterintuitive first that focusing the incoming beam to even smaller widths than the fiber mode results in a degradation of the coupling efficiency. However, it becomes more clear if one considers that according to gaussian beam optics (see Sec. 8.1) the beam width determines also its divergence (for a given wavelength).

Lateral displacement The beam propagation axis shows a lateral offset with respect to the target modes optical axis, i.e. the incoming beam does not hit the fiber core's center. With Δ_x denoting this offset, the coupling efficiency drops as

$$\eta = \eta_0 \cdot \exp\left[-\frac{2\Delta_x^2}{w_0^2 + w_1^2}\right] \quad (8.13)$$

Angular tilt The beam propagation axis are not parallel, i.e. the incoming beam hits the fiber tip with a non-perpendicular angle. Let θ be the angle between the optical axes. The coupling efficiency then goes as

$$\eta = \eta_0 \cdot \exp\left[-\frac{\pi^2 w_0^2 w_1^2 \sin^2(\theta)}{2\lambda^2(w_0^2 + w_1^2)}\right] \quad (8.14)$$

In a real setup all effects become important, which is why their relative size matters. Figure 8.9 shows a comparison of all degradation effects for realistic values of wavelength (1064 nm) and beam sizes (5.5 μm).

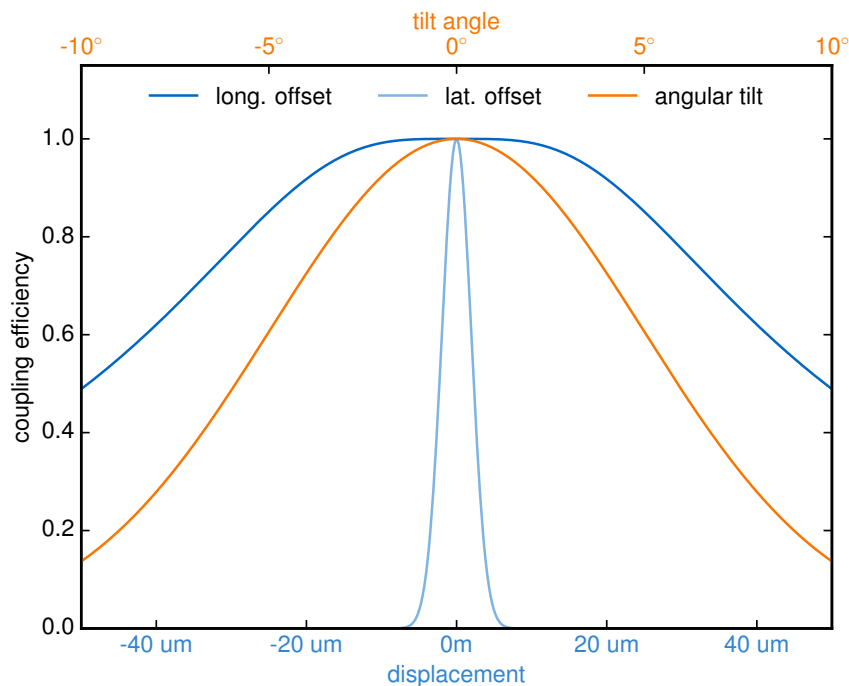


Figure 8.9: Theoretical coupling efficiency for various effects of degradation. All effects are considered isolated, though in a real setup they all become important at the same time. (Assumes perfectly matching beam widths, i.e. $w_0 = w_1$)

Not surprisingly, the lateral displacement is the most sensitive degree of freedom. Micrometer precision is required here in order to achieve a reasonable coupling efficiency. This is why in the actual setup, a coupling device is used unifying a focusing lens and the fiber mount in a single monolithic block. Though the task of matching and aligning the incoming beam with the

target mode still remains, the sensitivity of the coupling efficiency to lateral displacements is reduced¹⁴. The full coupling setup depicted in Figure 8.10

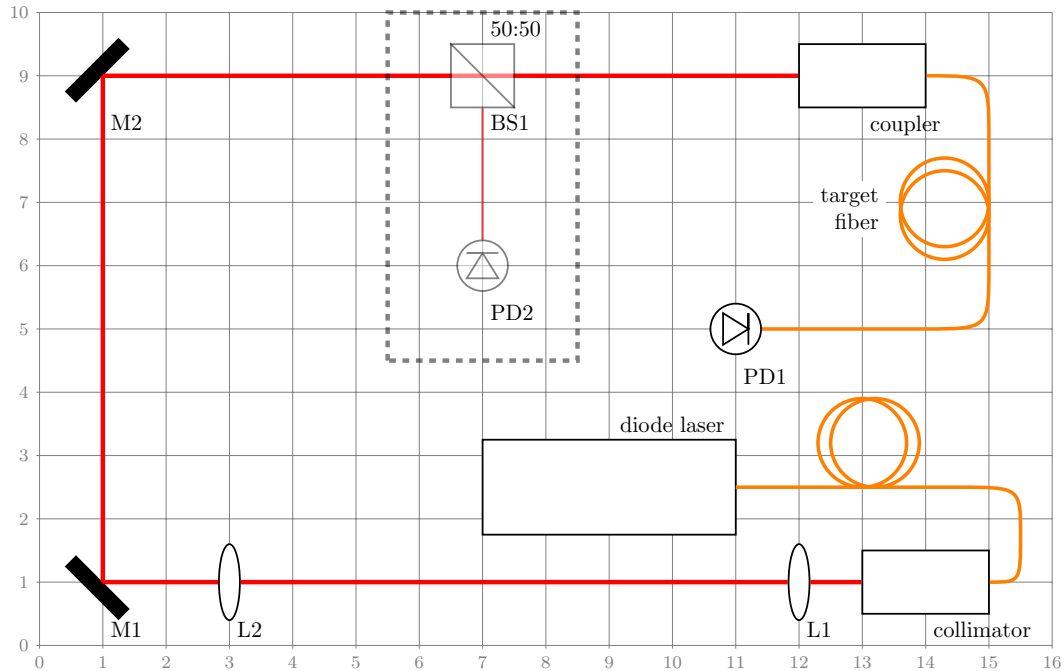


Figure 8.10: Schematic view of the free space to fiber coupling setup. The collimator is used as mockup of the beam leaving the RC. The grayed out components are optionally inserted to compensate for laser power fluctuations during stability tests of the setup.

The collimator on the lower right together with a 1064 nm diode laser builds a mockup of the incoming beam thus it has been chosen to mimic the characteristics of the beam leaving the RC. The ensuing lenses (L1 and L2) are then used to match the modes of the incoming and target beam mode, both of which have been examined beforehand using the knife edge device. For the incoming beam a width radius of (3.935 ± 0.003) mm has been found¹⁵, while the target mode shows a waist size of (0.854 ± 0.020) mm, located at about 1.94 m distance from the coupler¹⁶. The lenses' focal lengths have been chosen to be $f_{L1} = 200$ mm and $f_{L2} = 50$ mm as the result of numerically optimizing the coupling efficiency (8.11) while trying to keep the beam path as short as possible. Two adjustable plane mirrors (M1 and M2) are necessary to compensate lateral offsets and angular tilts simultaneously, i.e. four degrees of freedom. Finally, the beam reaches the coupler to which the target fiber is connected, guiding the light further into the ADR. For the demonstration setup the fiber instead shines its light onto a photodiode (PD1) measuring the power coupled in.

¹⁴Consider Eq. (8.13) with $w_0 = w_1 \equiv w$ (perfect mode matching) for large values of w .

¹⁵close to the design value of 4 mm

¹⁶Note that while the incoming beam is well collimated, the *back propagating* beam from the coupler has non-negligible divergence due to its smaller width

8.4 | Performance and stability

The coupling efficiency of the setup can easily be measured by building the ratio between the power in the target fiber P_1 and the incoming power P_0 of the laser.

$$\eta = \frac{P_0}{P_1} \quad (8.15)$$

As has been shown in the previous section, this crucially depends on how precise the optical components have been placed and how well the beam is aligned with the target mode. To fix possible lateral displacements and angular tilts, a technique called *beam walking* can be used, performing an iterative sequence of detuning and realigning both mirrors, converging to a maximum coupling efficiency. However, the mode matching and longitudinal offsets depend on the relative positioning of the components on the table and thus are less easy to correct. In particular, the relative distance between L2 and L1 is essential for the resulting beam width and divergence. The optimization process is implemented by mounting L2 on a xyz-stage with micrometer adjustment screws and monitoring the outgoing beam width as the stage is manually tuned. Further, though less sensitive, the distance between L2 and the fiber coupler is responsible for possible longitudinal mode displacements.

Applying the optimization procedures from above, a coupling efficiency of 90 % has been achieved. Once all components were correctly positioned, it was easy to reproduce this value even when the mirrors were intentionally detuned and recovered afterwards. However, care needs to be taken when rebuilding the whole setup from scratch, as the initial positioning of the components is crucial.

In order to probe the stability of the setup, a beamsplitter was installed in the beam path (see Fig. 8.10), allowing to correct for output power fluctuations of the diode laser. With this it was found that the compensated coupling efficiency was varying below the percent level, proving a stable performance of the setup.

In the general view of ALPS II both of these values, i.e. the achieved coupling efficiency itself and its stability, are satisfactory as the global sensitivity on $g_{a\gamma\gamma}$ scales as $1/\eta^{1/4}$ with the efficiency. However, the presented setup leaves room for further improvements. First of all, the optical components should be equipped with proper anti-reflective coatings for the operating wavelength of 1064 nm, as this was not necessary for the demonstration setup. Further the first lens facing the incoming beam (L1) should be replaced by a 2 inch equivalent of the currently used 1 inch optics as this reduces spherical aberrations. Also the fiber coupler could be replaced by a so-called Gradient-Index (GRIN) lens for which it is possible to directly fuse the fiber to it thus reducing the number of optical surfaces.

9

Implementing a slow control and DAQ system

Things are only impossible until they're not!

JEAN-LUC PICARD

There are two very basic requirements of any physics experiment. First, there is the need to operate and control the experiment — often an ensemble of various components and subsystems. Second there is the eager wish to acquire and store the accruing data in a meaningful way for later analysis.

The following chapter covers both aspects starting in Section 9.1 with the design and implementation of a Slow Control System for the ALPS II experiment. After discussing the general requirements on such a system, Sec. 9.1.1 describes DOOCS as the particular system chosen for ALPS II. As illustrative example Sec. 9.1.2 continues with the development and integration of climate monitoring into this system, while Sec. 9.1.3 proceeds with a more global view on the scalability. Finally, Sec. 9.1.4 summarizes the efforts and presents the current status.

The second part of this chapter starts with the description of the new DAQ system for the TES in Sec. 9.2 and in particular the software framework that has been developed in order to acquire and store the data (Sec. 9.2.1). Its integration and commissioning into the ALPS II experiment is described in Sec. 9.2.2 before Sec. 9.2.3 closes with a brief summary.

9.1 | A slow control system for ALPS II

The term *Slow Control System (SCS)* is mainly shaped by the High Energy Physics (HEP) community and is commonly used to describe a monitoring and control system acting on much slower time scales and smaller data rates compared to the main detector used in a (HEP) experiment. The spectrum of applications reaches from passive monitoring of environmental conditions such as climate to more complex control tasks such as actively steering actuators.

Before going into the details of the actual implementation the general requirements for such a monitoring and control system are reviewed. The first thing that comes in mind when interacting with hardware devices is the way how to communicate with them, i.e. the protocol or interface. A good SCS is supposed to support as many protocols and interfaces as possible maximizing the catalog of devices that may be integrated. In the same line goes multi-platform support making it possible to deploy the necessary software on various system architectures. The second most important criteria are reliability and stability which includes proper handling of failure scenarios and the ability to automatically return to a state of normal operation once a lost resource (e.g. network connection) is restored. Since the ALPS II experiment is planned in two stages of different extent and complexity (see Chapter 7) the SCS should be scalable, thus allowing the integration of additional devices without much effort. Some minor but non-negligible features are the availability of proper user-documentation and support.

There are various monitoring and control frameworks readily available for use, such as EPICS [110], TINE [111] or TANGO [112], that have often been developed in the scope of large scale experiments. The choice made for ALPS goes in the same line as it was originally designed as control system for the TTF LINAC¹ [113] at DESY and goes under the name of Distributed Object-Oriented Control System (DOOCS).

9.1.1 | Distributed Object-Oriented Control System

As already mentioned in the introduction, DOOCS was originally developed at DESY to cope with its large scale photon science experiments, e.g. the European XFEL [114] as the latest incarnation, and is still maintained and extended by DESY. DOOCS is written in C++ and follows, as the name already suggests, an object-oriented programming paradigm [115], which means that all devices (physical and virtual ones) are abstracted to classes that represent their particular kind of device and implement all necessary functionality. Each device under control is then represented by an instance of its corresponding class, hereinafter called *device server*.

The second main attribute of DOOCS is its *distributivity* which refers to its decentralized architecture as sketched in Figure 9.1. All nodes within this sketch embody a physical host machine interconnected by standard Ethernet [117] as commonly used in Local Area Networks (LANs). On the first layer, the *front-end* or *device* layer, the host machines are physically connected to the device to monitor or control and thus need to provide all necessary interfacing hardware. While DOOCS itself does not put any constraints on this interface, the above mentioned device server needs to run on this machine in order to provide the device's functionality to the DOOCS network. If a target device features an Ethernet interface itself it might also be connected to the DOOCS network with its monitoring/controlling device server running on another host within the network. The second layer in the DOOCS architecture is the *middle layer* featuring various kinds of services, most importantly a *name server* that translates the DOOCS internal addressing scheme to human readable specifiers of the following syntax:

Facility/Device/Location/Property

Each time an action or value is requested from a device server, DOOCS first resolves its address

¹nowadays FLASH

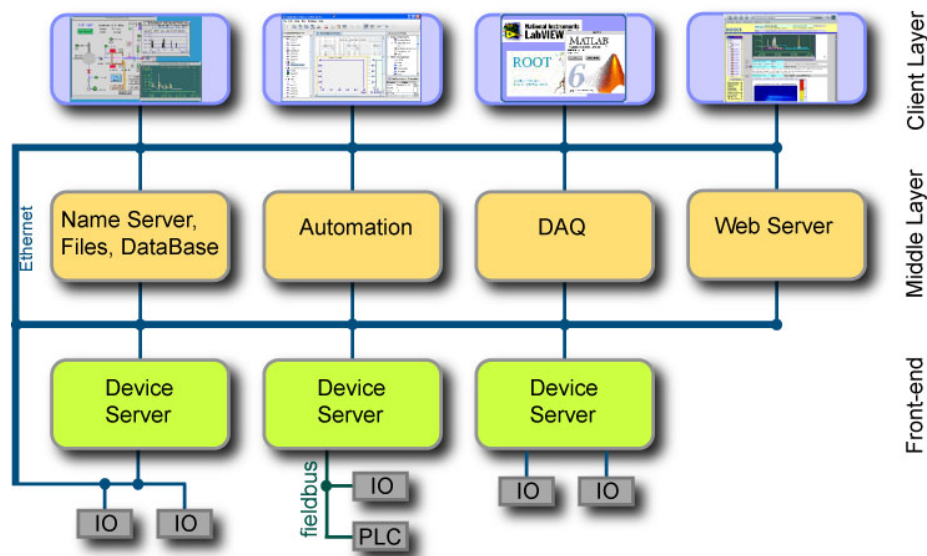


Figure 9.1: Conceptual design of the Distributed Object-Oriented Control System architecture. Nodes represent dedicated physical host machines interconnected by a standard Ethernet network. [116]

contacting the name server and starts the data exchange subsequently². Thereby, DOOCS uses Remote Procedure Calls (RPCs) to realize the interprocess communication between instances on different hosts. While running a name server is essential for the DOOCS infrastructure, other middle layer services are optional, e.g. an archiving server that periodically requests data from device servers and stores it to disk. The last layer is the *client layer* where users can access the network. DOOCS provides an Application Programming Interface (API) featuring various bindings to high-level languages such as PYTHON, JAVA and MATLAB, that allow users to access device servers or middle layer services. A common use case is e.g. the creation of a display panel showing live status information about the experiment, see e.g. Fig. 9.10 showing such a panel for the ALPS climate monitoring.

Finally, evaluating DOOCS along the requirements given in Section 9.1, it matches most of the given criteria:

- DOOCS itself has no constraints on the supported interfaces and even comes with a software repository of ready-to-use device servers.
- The officially supported operating systems are Linux (Ubuntu 64 bit [118] and Raspbian [119]), MacOS X [120], Solaris [121] and (experimentally) Windows [122].
- Due to its distributed approach, all device servers run independently, which means that in case of losing network connectivity, the device servers remain fully functional including local storage of all the data. Once the network connection is restored, the interprocess communication is automatically reestablished. Additionally, there is a *watchdog process* running on each individual device server, making sure that all necessary processes are up and running.

²somewhat similar to DNS resolution on the Internet

- Regarding scalability for the final stage of ALPS, there is only the necessity of providing enough network bandwidth throughout the experimental site, which nowadays is an easy task.
- The user documentation seems sparse in some places, though the DOOCS website³ provides a wiki-like *programmers guide*. Unfortunately this mostly documents raw API methods and classes without drawing a coherent picture of the framework.

Finally, DOOCS reveals itself as reasonable choice for the purpose of implementing a Slow Control System for ALPS II.

9.1.2 | Example: Environmental climate monitoring

Among various other devices that have been integrated during the course of this thesis (see Section 9.1.4 for a complete list), the environmental climate monitoring serves as an example here and is described in more detail. For the optical scheme described in Chapter 7, a stable atmospheric environment within the cleanrooms and in particular above the optical tables is crucial. Hence, continuous accurate monitoring is inevitable in order to assure stable conditions and the functionality of the automatic climate control system. As target reference value for the temperature stability, the TDR [54] states a value better than ± 0.1 K for all cleanrooms.

For this purpose the DS18B20 high-precision temperature sensor from Maxim Integrated⁴ has been chosen. This small Integrated Circuit (IC) device features digital temperature readings with 12 bit resolution within a temperature range of -55 °C to 125 °C [123] allowing for an effective precision of ± 0.044 K. The measurement principle is based on the comparison of two internal “bandgap-generated voltage sources” [124], one of them having a low, the other one having a high temperature coefficient. The actual temperature measurement is then deduced by comparing both sources and digitizing the voltage difference using a built-in ADC.

One of the great advantages of this particular sensor is the way it can be wired and deployed. The sensor communicates digitally utilizing the *1-wire* bus protocol only requiring a single communication line alongside the electrical ground reference.

1-wire communication bus

For the succeeding sections it is useful to understand the basic properties of the 1-wire bus protocol, hence it will be discussed briefly in the following.

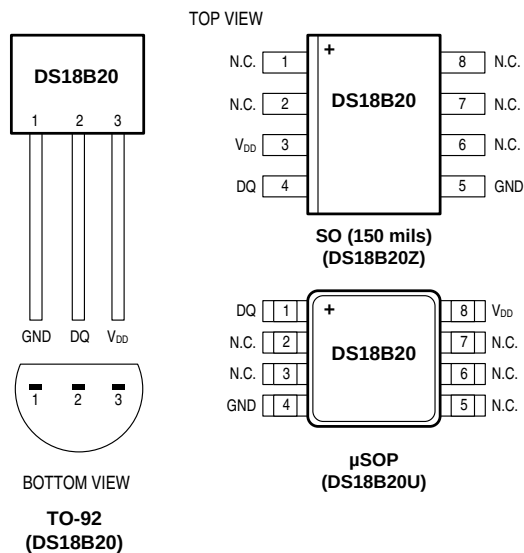
The 1-wire bus is a classical master/multi-slave bus system using asynchronous serial data transmission for communication. This means that multiple slave devices act on the same bus line controlled by a single master device without the need of distributing a common clock signal. Instead, synchronization is restored on every falling flank when the master pulls the bus to ground, i.e. logical LOW. The bus master addresses the slave devices with their imprinted 64 bit unique ROM number sending requests and assigning exclusive time slots for data transmission.

³<http://tesla.desy.de/doocs/index.html>

⁴Maxim Integrated, 160 Rio Robles, San Jose, CA 95134 USA

From the electrical point of view the bus consists of only two wires, a data line and ground. When the bus is idle the data line carries a voltage between 2.8V and 5.5V (logical HIGH) depending on the used type of 1-wire compliant devices. This allows the slave devices to acquire their supply power from this line, charging an internal capacitor that provides the supply voltage during time slots when the bus is in LOW state. This concept drastically simplifies the deployment process as no additional power supply is needed on the slave site. This mode of operation is called *parasitic power mode*.

The sensor itself is housed in a TO-92 package as can be seen in Figure 9.2a. In order to enable the creation of multi-sensor nets in an easy extensible and relocatable manner, the sensors were equipped with a standard Lemo® connector and a short (≈ 30 cm) coaxial cable. Figure 9.2b shows an example of an assembled and deployed sensor above one of the laser tables.



(a) Packaging options. The V_{DD} pin is shortened to ground if operating in parasitic power mode. [123]



(b) Sensor equipped with a Lemo® connector and deployed above a laser table.

Figure 9.2: Packaging options and deployment example of the DS18B20 temperature sensor.

Several sensors have been prepared this way and deployed within the laboratory environment forming a single extended net interconnected by coaxial cables. In order to provide a 1-wire bus master to this net, a *Raspberry Pi 2 Model B* single-board computer⁵ is used.

Its widely used operating system Raspbian⁶ already comes with a software-defined 1-wire bus master implemented as kernel module. On the hardware side it only requires a passive 4.7 kΩ pull-up resistor connecting the supply voltage and the data line (cf. Figure 9.3) in order to prevent an electrical short when the bus is pulled to ground.

However, the drawback of this “simple solution” is, that it only performs well when operating on small sensor nets. A quick test connecting only a single DS18B20 temperature sensor to

⁵Raspberry Pi is a trademark of the Raspberry Pi Foundation. <https://www.raspberrypi.org/>

⁶Derived from the Debian Operation System

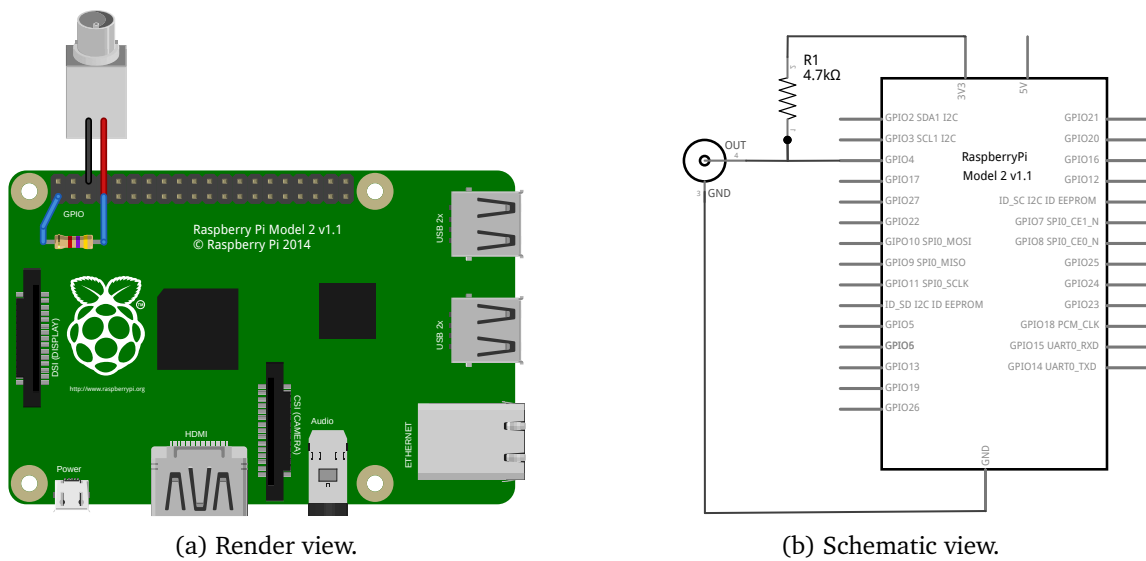


Figure 9.3: Hardware wiring for the software designed 1-wire master requiring only a passive pull-up resistor.

the 1-wire master probing different lengths of the coaxial cable shows a maximum line length of 35 m. For transmission line lengths above this value, the 1-wire master loses connectivity with the sensor. Since the reason for this effect is apparently of electrical nature, the same test conducted with half the pull-up resistance allowed for twice the maximum length, i.e. 70 m.

It is apparent that reducing the pull-up resistance further is not a reasonable option in the light of ALPS II, where distances of more than 100 m need to be covered. In order to investigate the factor limiting the transmission line lengths, an oscilloscope was utilized to observe the (logical) electrical signals sent across the bus line between master and sensor. The most prominent change in the waveform could be discovered at the end of a “0 bit”, i.e. the rising flank after the bus line has been released from being pulled to ground. There, with varying either line length or pull-up resistance, a change in the rise time is observed. Figure 9.4 contains the two example configurations from above with the default and halved (passive) pull-up resistance.

As can be seen, the time constant of the rising flank increases reciprocal with the (passive) pull-up resistance. Analogous it increases linearly with the transmission line length. This effect can be understood when considering the electrical properties of the used coaxial transmission cable, which features a specific capacitance of up to 100 pF m^{-1} . Together with the pull-up resistor this leads to *capacitor charging curve* with time constant

$$\tau_{\text{rise}} \propto RC \propto cRl \quad (9.1)$$

where denotes c the specific capacitance per cable length l . This clearly excludes this particular implementation of the 1-wire master since restoring the rising flanks time constant would require to drop the pull-up resistance to zero.

A more elaborate version has been developed using the DS2482–100 single channel 1-wire master [125]. This compact IC is designed to serve as bridge device between the 1-wire network and an I²C controller which the Raspberry Pi can provide. The most important feature comes

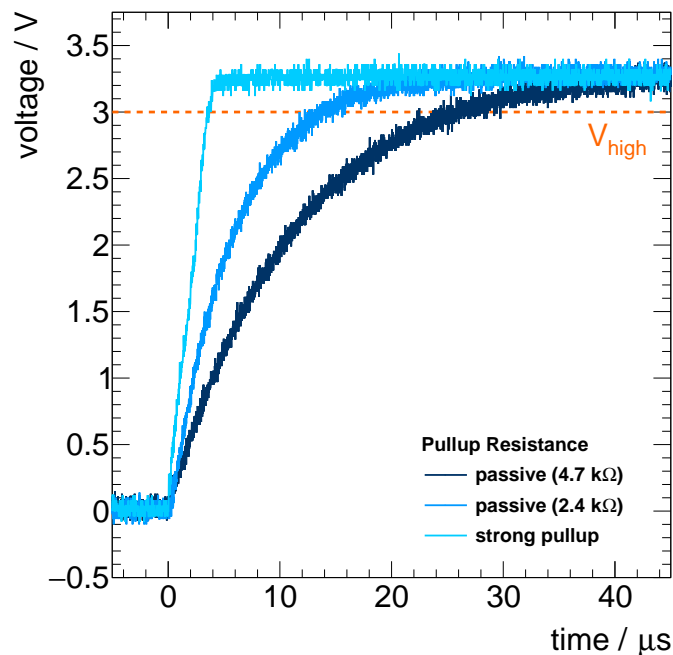


Figure 9.4: Rising flank on the 1-wire bus at the end of a “0 bit” for different realizations of the pull-up resistor. All measurements were taken with a single DS18B20 temperature sensor on a 20 m transmission line to the 1-wire master. The orange dashed line denotes the limit at which a voltage signal is recognized as HIGH.

with the possibility to control an external MOSFET providing a *strong pull-up* (see Fig. 9.5).

The working principle of this setup is to offer a low-impedance path from the voltage source to the bus line when the bus is HIGH while still presenting a finite resistance during the bus being LOW. The integrated p-Channel MOSFET is controlled by the DS2482-100 and switches accordingly between low and high impedance as is appropriate. This restores the time constant of the rising flank as can be seen in Figure 9.4. With this configuration the same transmission line tests using a single sensor have been conducted and line lengths of more than 100 m have successfully been operated.

For easy mounting, a Raspberry Pi compatible *shield* carrying all 1-wire master components (cf. Fig. 9.5) has been designed. Figure 9.6 shows the prototype with the Lemo[®] connector facing the sensor network. On the software side the 1-Wire Filesystem (OWFS) project⁷ is used providing a filesystem entry for every sensor recognized in the network. With this, sensor readings can easily be triggered by issuing

```
$> cat /mnt/1wire/<sensor ROM>/<property>
```

from the command line which enables a very simple and robust way of integrating the sensor network into DOOCS. The only task remaining for the DOOCS device server (see Section 9.1.1) is to issue the above command for every sensor and store the temperature value returned after applying a calibration correction function.

⁷<http://owfs.org/> (licensed under GPL)

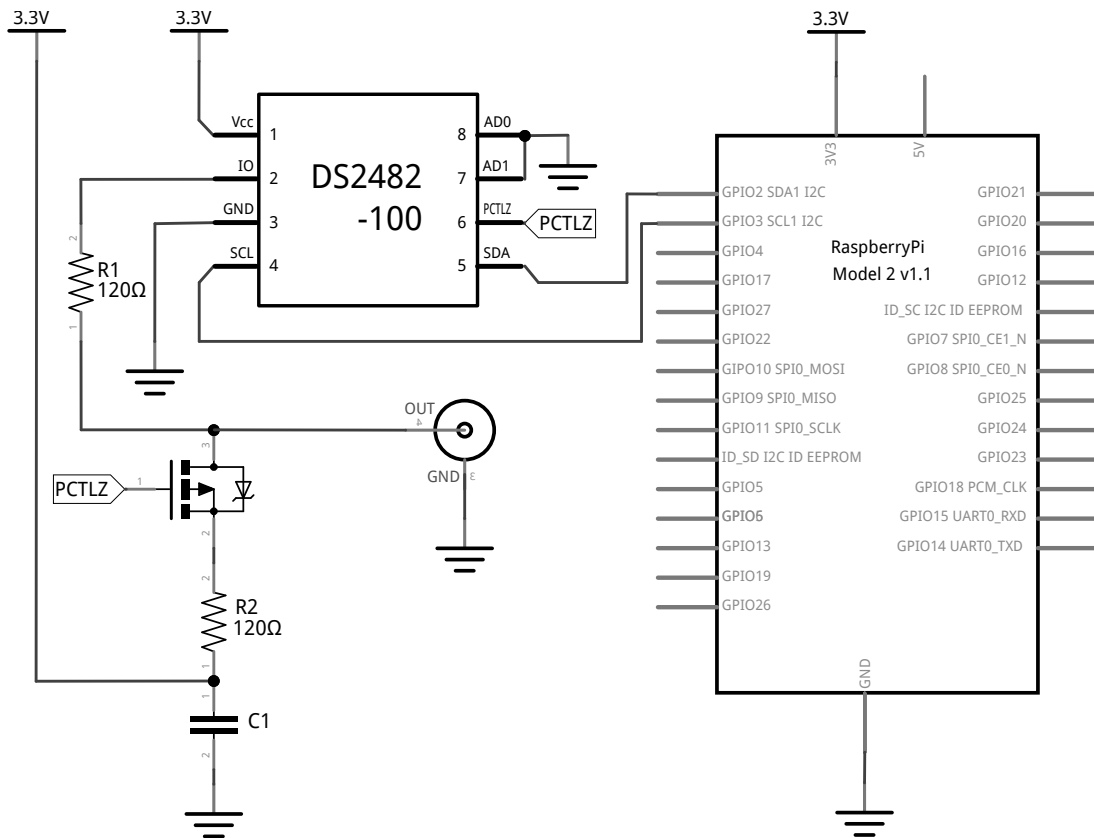


Figure 9.5: Schematics of the 1-wire master using the DS2482–100 bridge device and an external MOSFET for strong pull-up.

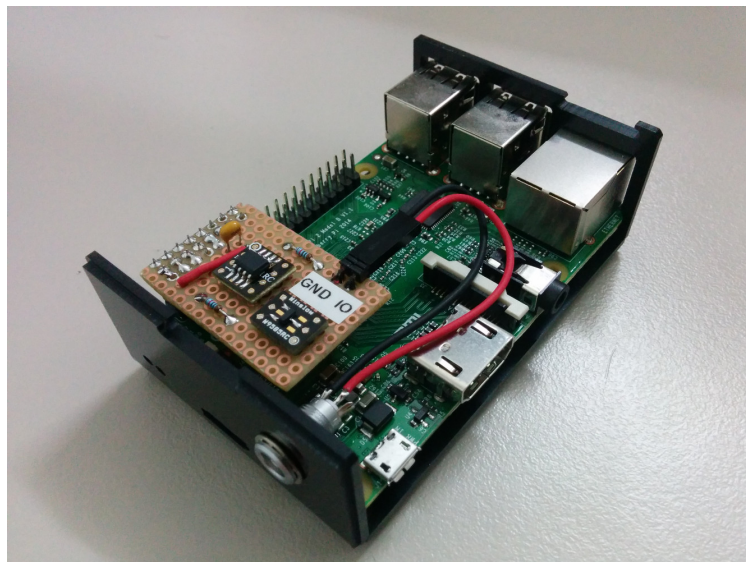


Figure 9.6: 1-wire master hardware shield mounted on a Raspberry Pi. The connector at the bottom interfaces the sensor network.

Although from an optics point of view, mostly relative temperature changes are of interest, all sensors have been calibrated against a high-precision temperature reference to allow for comparability of the conditions on different laser tables. Using a controllable climate chamber with all available sensors packed closely side-by-side with the reference probe, various temperature conditions from 0 °C to 40 °C have been set. An example calibration curve is given in Figure 9.7. It shows the difference between the temperature measured by the DS18B20 and

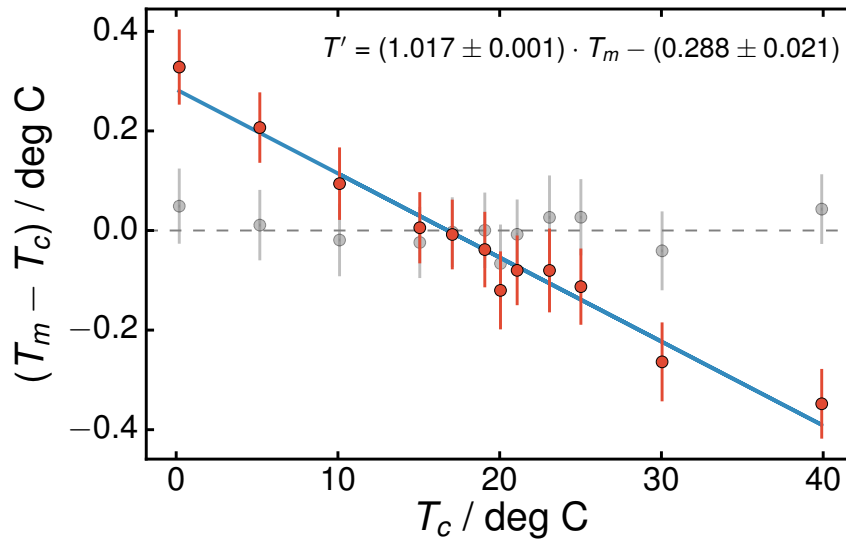


Figure 9.7: Example calibration of a DS18B20 temperature sensor against the high precision temperature probe. T_m and T_c refer to the measured (uncalibrated) temperature value and the reference temperature respectively. The uncertainties shown include digitization error and statistical fluctuation. The grey dots indicate the closure of the original data *after* applying the calibration correction.

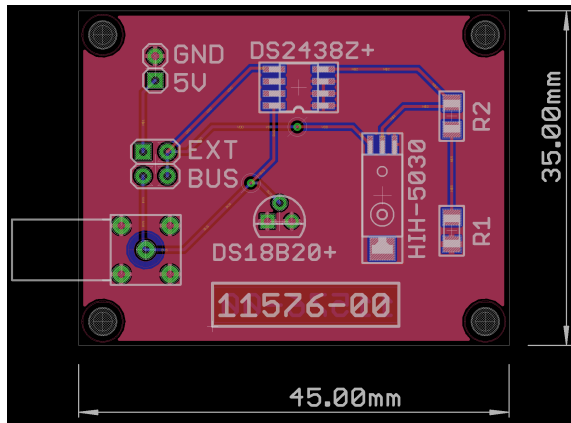
the temperature of the reference probe with the respect to the latter. The resulting curve can be approximated with a first order polynomial leading to the correction function given in the upper right corner of the figure with T' being the corrected temperature. A similar behaviour has been found for all the sensors and a table of the resulting calibration coefficients is given in the appendix (Table B.1).

Figure 9.7 also shows a closure test, i.e. the original data points corrected by the determined calibration function, indicated by the grey dots. As can be seen from the resulting plot, the accuracy of the calibrated temperature reading is better than 0.1 °C which matches very well with the requirements given in the beginning.

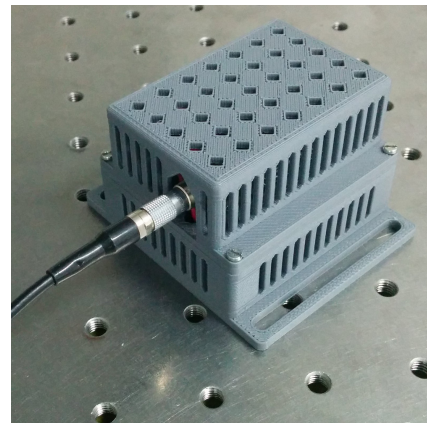
ALPS climate board

Besides individually deployed temperature sensors, a small modular *climate board* has been developed, carrying a sensor for relative air humidity next to a DS18B20. The layout of the Printed-Circuit-Board (PCB) is shown in Figure 9.8a. The Relative Humidity (RH) measurement is performed by a Honeywell⁸ HIH-5030 low voltage humidity sensor delivering an output signal

⁸Honeywell, 1985 Douglas Drive North, Golden Valley, MN 55422



(a) PCB layout.



(b) Assembled climate board inside its housing.

Figure 9.8: ALPS climate board for relative air humidity and temperature monitoring compliant with the 1-wire bus system.

proportional to the measured RH

$$V_{\text{out}} = V_{\text{cc}}(a \cdot \text{RH} + b) \quad (9.2)$$

with V_{cc} denoting the supply voltage and a and b being calibration constants given in the datasheet [126]. However, since this is quite dependent on the air temperature, the RH value still has to be corrected using

$$\text{RH}_{\text{true}} = \frac{\text{RH}}{c - d \cdot T} \quad (9.3)$$

with the correction coefficients c and d given by the manufacturer [126].

All this work, i.e. reading the output voltage, converting it to digital and applying calibration and temperature correction functions, is done by the 1-wire compliant DS2438. This IC, originally designed to act as battery monitor, comes with a built-in ADC and a temperature sensor capable of performing all tasks mentioned above. However, since its internal temperature sensor is of lower accuracy than compared with the DS18B20, the climate board may optionally be equipped with the latter one.

For convenient deployment of the climate board, including an optional battery pack⁹, a well-aerated housing has been designed and synthesized using a 3D-printer. A fully assembled and connected package is shown in Figure 9.8b.

9.1.3 | Building the computing infrastructure

A reliable and performant computing infrastructure is a crucial prerequisite to nearly every physics experiment. Since the demands on such infrastructure are highly case-dependent, there is usually no off-the-shelf solution that fully covers all requirements. The following section out-

⁹Operating too many HIH-5030 sensors on the same bus line exceeds the power available from the Raspberry Pi.

lines the design (goals) and implementation process of the *ALPSnet*, the computing infrastructure for the ALPS laboratory.

The main ambition when creating the ALPSnet was to rely on as least *external services* as possible meaning to create an isolated network infrastructure, independent from the local institute's IT department. This allows to dynamically and quickly adapt to upcoming needs, like the provision of new services or the integration and interconnection of new subsystems, but also comes with the price of being in charge of responsible administration. However, this approach secures the performance needs, e.g. interconnection bandwidth, availability of services, ..., and also reduces the attack surface, as will soon be obvious.

The basic network infrastructure is depicted in Figure 9.9. The ALPSnet is physically interconnected using Gigabit Ethernet throughout the laboratory space with the host called `alpsdaq0` being the only access point from the public network. Any traffic into or out of the ALPSnet needs to pass this host while according `iptables` rules filter any attempt to access the network other than via `ssh` enforcing user authentication.

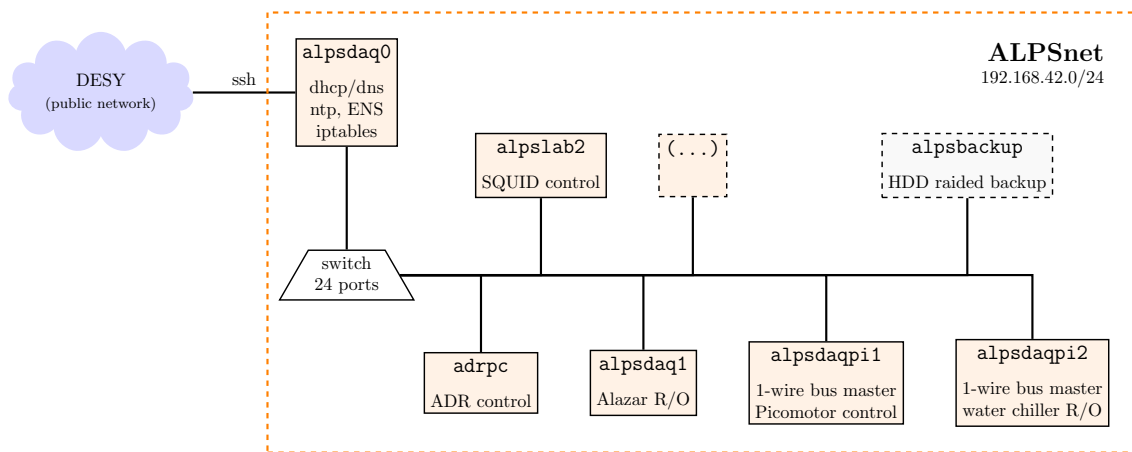


Figure 9.9: ALPSnet network infrastructure. Black lines represent Ethernet network connections. Orange boxes show currently operating host systems with their corresponding hostname (purpose) on top (bottom). Black dashed boxes state future hosts.

Further `alpsdaq0` provides other central services to the network, summarized in the following list:

DHCP/DNS: Provides assignment of IPv4 addresses and hostnames. Registered hosts are allocated with a fixed IP address, while half of the `/24` address space is reserved for dynamic allocation to transient devices.

NTP: All hosts within the ALPSnet synchronize their system clocks with `alpsdaq0` on a regular basis. This ensures a consistent time reference throughout the network. The `alpsdaq0` itself synchronizes with the Network Time Protocol (NTP) servers provided by DESY.

ENS: Resolution of device names used in DOOCS. Data requests or device commands are preceded by a call to this service in order to resolve the according device server (cf. Sec. 9.1.1).

The ALPSnet infrastructure as described above allows for easy extension, e.g. an automatic backup server continuously requesting data from *all* device servers, is currently envisioned.

9.1.4 | Summary and current state

The sections above describe the design and commissioning of the SCS for the ALPS experiment which is now briefly summarized.

The ALPSnet constitutes the base layer of device interconnection throughout the laboratory space. Disjunct from the public institute's network featuring a single gateway host¹⁰ it provides all services necessary to operate the control and monitoring system autonomously and independent from the public network or the internet.

On top of the ALPSnet resides the actual Slow Control System layer realized by DOOCS. Due to its distributed nature, all device servers controlling or monitoring physical hardware are run on host machines located in the close proximity to this hardware without the need of centralized services¹¹. This also guarantees ongoing operation without data loss even in the case the network connection drops. As of writing this thesis the devices listed in Table 9.1 have already been integrated into DOOCS and Figure 9.10 shows an example status panel visualizing the climate conditions across the experimental site.

Table 9.1: Devices integrated into the SCS and the according tasks performed by the DOOCS device servers.

device	device server tasks	interface
Termotek P810 Air/Water Chiller	Monitor In/Out water temperature / flow, exhaust temperature, system status	RS232
Entropy ADR cryostat	Monitor temperature of all stages, magnet current, vacuum pressure	logfile
New Focus 8152 Picomotor controller	Control mirror actuators	RS232
ALPS climate board	Initiate and log temperature/humidity measurements	I ² C / 1-wire
Alazar ATS9626 waveform digitizer	Initiate and control data acquisition runs and monitor current status	PCIe
Beckhoff CX1000 Laser controller	Monitor output power and diode currents of the main laser	logfile

Further extensions are already foreseen including monitoring of the magnet current of the ALPS II magnet string, the status of the laser interlock safety system and the vacuum pressure

¹⁰[alpsdaq0](#), cf. Figure 9.9

¹¹The only exception to this is the Equipment Name Server hosted on [alpsdaq0](#) to allow for easy accessing the device servers.

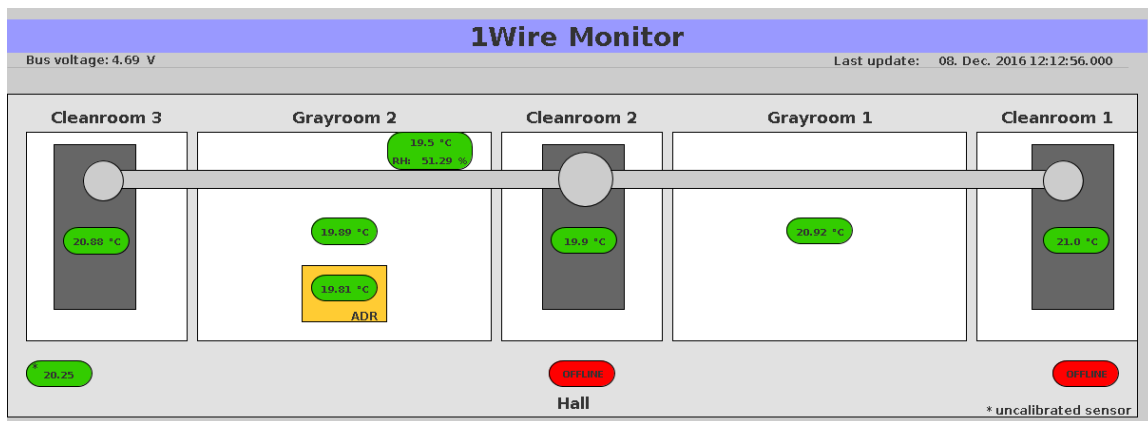


Figure 9.10: DOOCS status panel visualizing the current temperature and humidity readings from the 1-wire bus system.

of the beam pipe pumps. Integrating all these devices leads to the creation of a coherent picture of the experiment's status.

9.2 | Fast DAQ system for the ALPS detector

On much faster timescales than the previously described SCS operates the Data Acquisition (DAQ) system used to record detector data from the TES. The duration of signal pulses¹² is typically in the order of a few μs with the rising flank's time constant being even down to the order of ns. The task for the DAQ system is to provide accurate time resolution and low noise digitization of the waveforms, as this is crucial for e.g. the energy resolution of the system and the suppression of pile-up induced background (see also Cha. 10).

The previously operated DAQ system was realized by a Tektronix DPO7104C oscilloscope used to acquire data from the detector and store it in its internal memory using plain text files. This virtue of simplicity however suffered from the fact that due to the given hardware, there was always a trade-off between sampling rate and measurement time to be made. Choosing a high sampling rate only allowed for storing a few seconds of data whilst a low sampling rate embodies an effective loss of information.

For the new DAQ system the ATS9626 waveform digitizer from Alazar¹³ has been chosen. This PCIe card features two simultaneously sampled input channels with a maximum sampling rate of 250 MHz at 16 bit depth. Further it comes with an Altera Stratix III coprocessor FPGA allowing for fast preprocessing of the raw input data even before storing it to the on-board memory. These and all other relevant characteristics are listed for reference in Table 9.2.

Besides a classical triggered acquisition mode using either the built-in threshold trigger or listening to the external trigger input, it is possible to operate the card in *continuous mode*. Utilizing the on-board memory, this allows for gapless acquisition while streaming the data to the host computer.

¹²see Section 7.2 for more details on the signal pulse shape

¹³Alazar Technologies Inc., Canada

Table 9.2: Characteristics of the Alazar ATS9626 waveform digitizer card used for TES data acquisition.

sampling rate	250 MHz
sampling depth	16 bit
input range	± 1.25 V (fixed)
input bandwidth	DC–120 MHz
on-board memory	$2 \cdot 10^9$ samples dual-port
interface	PCIe x8 (gen. 1.0)

The following section explains the implemented readout modes in more detail with an emphasis on acquiring TES detector data¹⁴ and discusses the achieved performance.

9.2.1 | Building the DAQ framework

The ATS9626 ships with a proprietary pre-compiled library and an API with bindings to various programming languages. For performance reasons, in particular the new multithreading concepts for parallel processing recently added to the standard¹⁵, C++ has been chosen as main language to develop the DAQ framework.

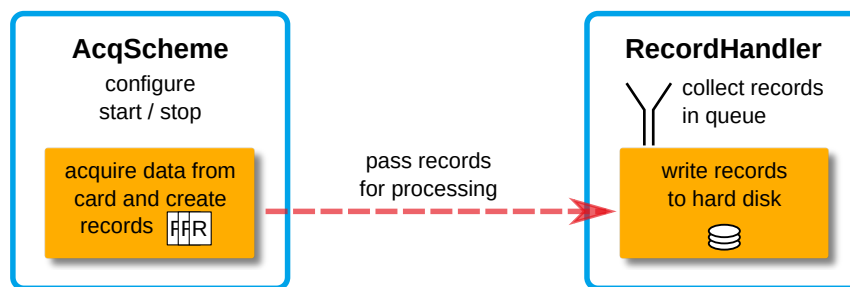


Figure 9.11: Schematic working principle (simplified) of the DAQ framework. Blue boxes depict object classes, orange boxes separate threads.

The basic working principle of the framework is schematically depicted in Figure 9.11. The main class interacting with the ATS9626 card is named `AcqScheme` (Acquisition Scheme). Its responsibility is to configure the card for the desired acquisition mode (see below), and provide methods to actually control the data taking, like e.g. `start` and `stop`. Raw data collected by the card is first buffered in the on-board memory and subsequently transferred in bunches of predefined size through the PCIe bus right into the host computer’s memory using Direct Memory Access (DMA). For this purpose the acquisition framework has to allocate sufficiently enough memory buffers to receive this data. During transfer, new incoming data is still recorded to the on-board memory¹⁶ and is subsequently transferred to the host, enabling to continuously record data without interruption.

¹⁴For a detailed description of the expected TES signal shape refer to Section 7.2

¹⁵referring to the C++11 standard here, see e.g. [127]

¹⁶The on-board memory is a dual-ported First In First Out (FIFO) memory, allowing to write new data on one side while reading old data on the other side.

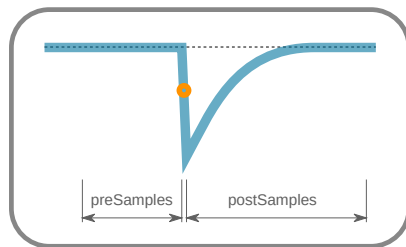
In the next step, the `AcqScheme` encodes the raw data, i.e. converts 16 bit *unsigned integer* values to their corresponding *floating point* voltage values, and creates *Records*. Among the actual voltage data, these *Records* also contain further meta data like, e.g. input channel, a timestamp and the sampling rate. Since *Records* at this point still *reside* within non-permanent Random Access Memory (RAM), the `AcqScheme` hands them over to a `RecordHandler` and returns the used memory buffer back to the AT9626 to be filled with another bunch of (raw) data.

As writing data to a Hard Disk Drive (HDD) is an *expensive* operation (in terms of time) compared to RAM I/O, the `RecordHandler` runs in a separate thread to avoid blocking of the `AcqScheme`. Therefore the only task of the `RecordHandler` is to retrieve *Records* enqueued for writing and save them permanently to disk.

Both, `AcqScheme` and `RecordHandler`, are abstract classes only implementing the base functionality. Child classes inheriting from the latter one include the `RootRecordHandler` writing ROOT [128] trees and the `BinaryRecordHandler` saving *Records* in a custom binary format. The descendants of `AcqScheme` realize different modes of acquisition and are listed below:

Triggered Mode

Classical triggered acquisition utilizing the built-in threshold trigger.

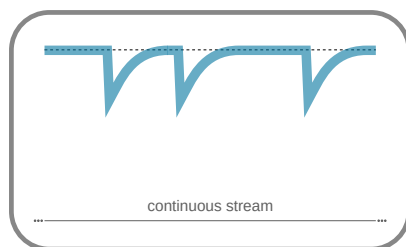


Fires when the input signal exceeds a certain voltage threshold on either rising or falling flank. The stored data consists of a pre-defined amount of samples before and after the trigger point.

Although this seems to be the most straightforward approach to record TES events it has a significant flaw. That is, the built-in trigger is not sensitive for signal amplitudes smaller than ± 120 mV, which just coincides with the expected amplitude range of the TES signals. Further the trigger threshold is encoded in only 8 bit, which means it can only be adjusted in steps of ≈ 10 mV (max. input range divided by 2^8). Of course it is possible to amplify the input TES signals, but as this would introduce additional sources of noise, this solution is disfavored over the others described below.

Continuous Mode

Gapless continuous streaming of the sampled time series.



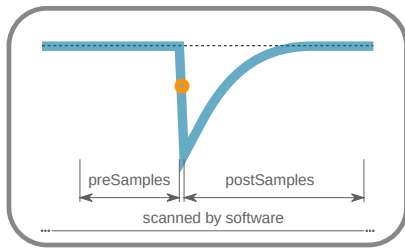
The input signal is perpetually sampled and the data is stored (in bunches) as *full-take*.

This allows to store time series of TES data for specialized offline analysis, e.g. baseline noise (see below) or high-rate photon samples like pileup or saturation. Naturally this generates a tremendous amount of data in a short period of time, e.g. $2 \cdot 16 \text{ bit} \cdot 50 \text{ MHz} \approx 200 \text{ MB s}^{-1}$ when sampling both channels at a frequency of 50 MHz. Hence,

the maximum time series length is limited by the used sampling frequency as the host computer's disk write speed constitutes the bottleneck. However, even when sampling with maximum rate, i.e. 250 MHz or equivalently 1 GB s^{-1} , tests showed that the system can keep up for a full second of continuous data recording, as opposed to the previous DAQ system, where the equivalent maximum sampling rate for 1 s time series was 20 MHz.

Pseudo-triggered Mode

Triggered mode analysing the continuous stream of data in host memory.



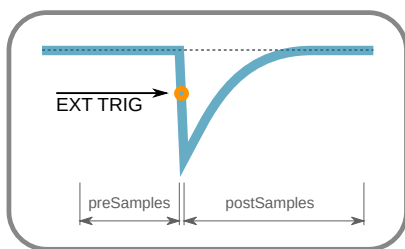
Like in *continuous mode*, the data is streamed to host memory, but is scanned for a matching trigger condition by the host CPU. In case the trigger fires, a pre-defined amount of samples before and after the trigger point is stored. This mode has been designed to overcome the drawbacks of the classical *triggered mode* described above.

As the rate of incoming data scales linear with the used sampling rate, an efficient scanning algorithm is required in order to avoid blocking conditions, i.e. the decision if a data bunch contains a triggering event¹⁷ needs to be made before the next data bunch can be processed. Such algorithm has been developed splitting the bunches into four parts scanned in parallel using multithreading¹⁸.

Since the trigger threshold is set in software and compared to the raw input data, it is effectively encoded in 16 bit allowing much finer granularity as opposed to the built-in hardware trigger.

External-triggered Mode

Triggered acquisition using an external trigger signal.



Listens for a logical signal on the card's *external trigger* input and stores the input signal (pre- and post-samples) when such a trigger signal arrives.

This mode also tackles the insensitivity problem of the built-in hardware trigger (see above) by utilizing an independent external trigger source while retaining the simplicity and robustness of the classical *triggered mode*.

For the application of recording TES signal data, a NIM¹⁹ crate has been composed analysing the analog input signal and providing a suitable logical trigger signal to the DAQ card as Section 9.2.2 will describe in more detail.

Several basic tests have been performed in order to verify the correctness of implementation in particular the correct handling of data bunches after retrieving them from the ATS9626. An

¹⁷It is also possible that a bunch contains more than one triggering event.

¹⁸Together with the remaining threads for `AcqScheme` and `RecordHandler` this utilizes up to 6 CPU cores at once, leaving enough resources for the operating system on the host computer.

¹⁹Nuclear Instrumentation Standards [129]

exemplary result is shown in Figure 9.12, where the recorded time series of a 10 Hz test signal is plotted.

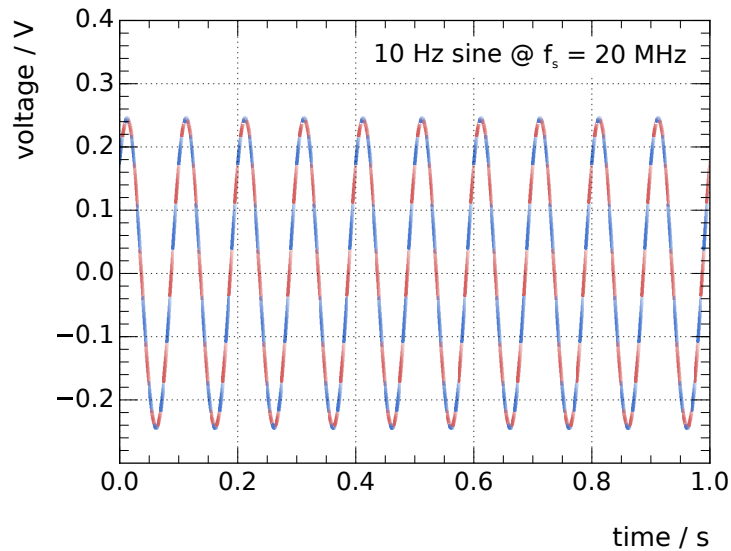


Figure 9.12: A 10 Hz test signal recorded by the ATS9626 in *continuous mode* sampling with 20 MHz. The alternating colors indicate the single buffers in which the data has been transferred to the host memory.

This simple but important test demonstrates the interruption-free acquisition of the card and furthermore the correct processing of the retrieved data buffers by the framework.

9.2.2 | Commissioning and integration

The ATS9626 card has been installed in an appropriate workstation computer featuring an Intel® Xeon® E5-1620 v2 CPU [130] and 16 GB of RAM providing reasonable processing power for the (multithreaded) data acquisition.

The external trigger implemented in a NIM conformal crate enables in its simplest configuration the setting of an analog trigger threshold on a single channel. More complex plans, e.g. 2 channel coincidence triggering, can easily be realized due to the modular nature of the standard. The crate in its current configuration is shown schematically Figure 9.13. For the sake of simplicity the following description refers only to a single channel setup as the two channel configuration is straightforward. The first step in the processing chain of the crate is a Fan-In/Fan-Out module with the sole purpose of duplicating the input signal. Both outputs carry the unmodified signal, hence one of them is plugged directly to the DAQ card's input. The other one is connected to a first amplifier stage allowing to amplify the signal without altering its shape. The multiplication factor has been chosen to be 10 in order to match the dynamic range of the following discriminator stage. With its adjustable threshold (from -0.03 V to -1.0 V) this defines the actual trigger condition. An adjustment screw on the front panel allows to tune this threshold and a DC test point allows to obtain the corresponding value²⁰. The last stage

²⁰simple voltage measurement of this point against ground, e.g. the crate itself, with an additional factor of $\times 10$

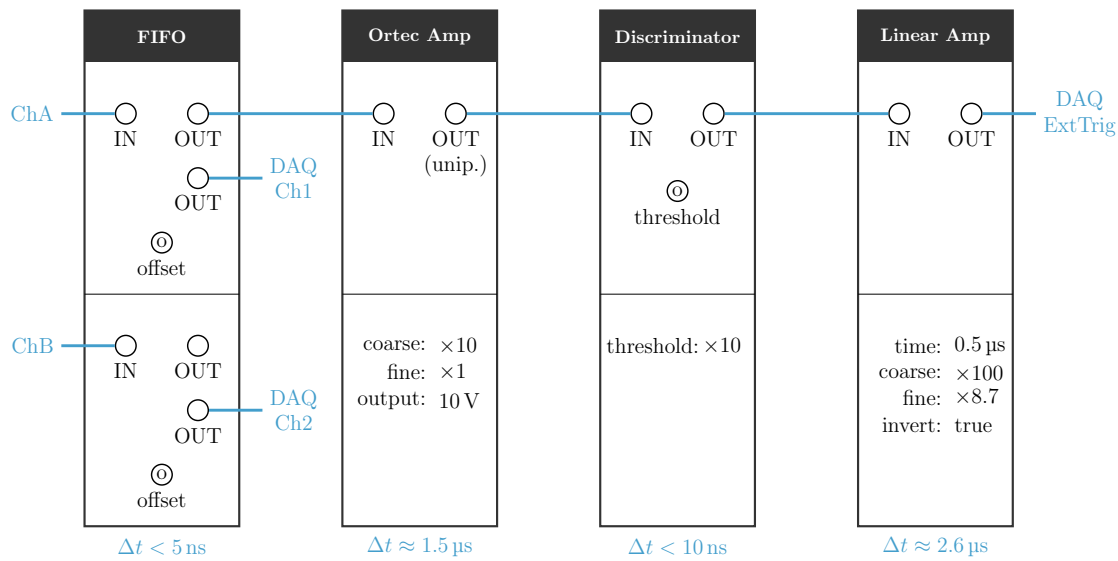


Figure 9.13: Schematic view of the NIM crate used as external trigger to record TES events with the ATS9626 data acquisition card. The individual time delays introduced by each module are shown at the bottom and were estimated using an oscilloscope.

in the chain is another amplifier translating the discriminators trigger pulse from NIM voltage standards to LVTTTL²¹ which is recognized by the DAQ card. The signals passage through the NIM modules introduces a time delay of about 4.1 μs with respect to the split-off signal line directly connected to the DAQ card. This, however, can easily be compensated by the readout framework by choosing enough pre-samples²² in the acquisition mode or using a delay line.

The maximum trigger rate that this setup can cope with has been determined using a waveform generator producing TES-like signals at defined repetition rate and turns out to be 10 kHz — several orders of magnitude above the expected event rate of ALPS II. The trigger efficiency has been measured at this maximum rate using the same waveform digitizer with variable amplitude and a simple NIM counter module. Calculating the ratio between triggered and generated pulses yields the trigger efficiency²³:

$$\hat{\varepsilon} = \frac{N_t}{N_0} \quad \sigma_{\hat{\varepsilon}} = \sqrt{\frac{\varepsilon(1-\varepsilon)}{N_0}} \quad (9.4)$$

The resulting turn-on curve is plotted in Figure 9.14. For each signal amplitude value about $1.2 \cdot 10^6$ pulses have been generated and sent through the crate probing for a trigger. Assuming only stochastic fluctuations of the probe signal's amplitude, the resulting turn-on curve should follow the Cumulative Distribution Function (CDF) of a normal distribution centered around the trigger threshold with a variance corresponding to these fluctuations. Figure 9.14 shows the fit of such CDF and the resulting parameters are given in Table 9.3. As can be seen, the fitted

²¹Low Voltage Transistor-Transistor Logic

²²samples recorded before the trigger point, cf. Section 9.2.1

²³The ratio corresponds to the Maximum Likelihood Estimator (MLE) of the propability assuming the trigger decision to be a Bernoulli process

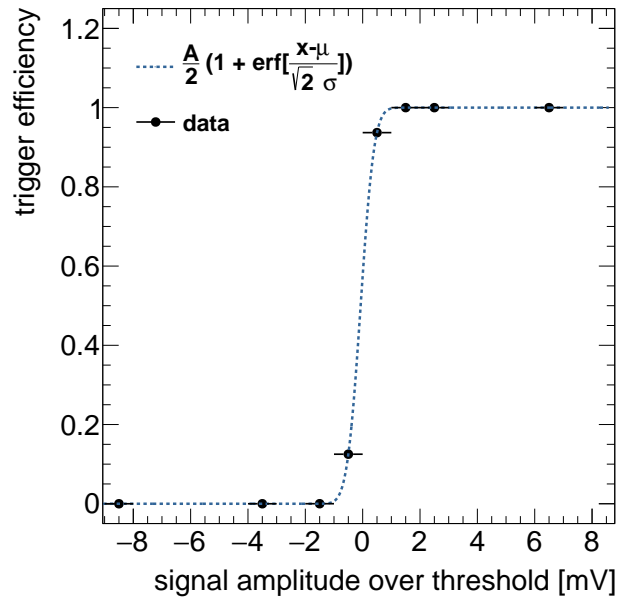


Figure 9.14: Trigger efficiency of the external NIM trigger. Test signal pulses generated by a waveform generator with tunable amplitude.

Table 9.3: Estimated parameters of the trigger efficiency turn-on curve fit. Resulting $\chi^2/\text{NDF} = 48.3/5$

parameter	value
μ/mV	$-0.0709(4)$
σ/mV	$2.679(2)$
A	$0.999\,967(3)$

curve describes the data appropriately, whereas the reduced χ^2 of 9.7 is quite large. However, it should be noted that the uncertainty estimator σ_ε given in Eq. 9.4 is only valid for non-vanishing and non-unity values of ε which reduces the meaningfulness of this value.

Another important characteristic of the DAQ system to examine is its baseline noise level. In order to measure and compare this noise spectrum with the previously used oscilloscope, an Fast Fourier Transform (FFT) application²⁴ based on FFTW [131] has been developed inferring frequency spectra from time domain samples and vice versa. The plot in Figure 9.15 shows the linear spectral densities of both, the ATS9626 and the oscilloscope, calculated from 10 s timelines each having all inputs terminated with 50 Ω load impedance. The most prominent and also most important difference between them is the fact the ATS9626 has a baseline noise level about two times lower compared to the oscilloscope over the major part of the spectrum. The few spectral features showing up as narrow peaks, are most likely caused by the intrinsic details of the acquisition electronics. Figure 9.15 further shows the theoretical levels of digitization

²⁴implemented in the FAST framework described in Cha. 10

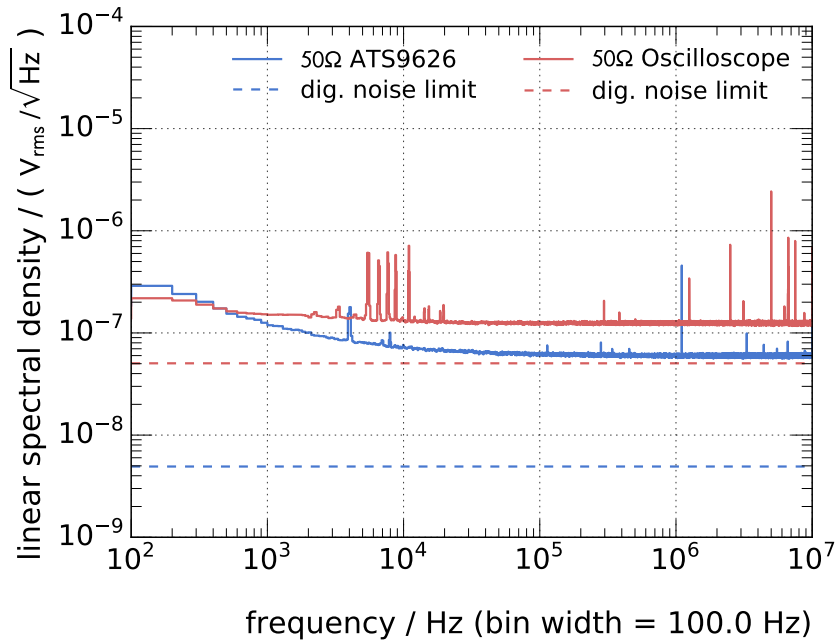


Figure 9.15: Baseline noise spectra of the ATS9626 compared to the previously used oscilloscope both terminated with $50\ \Omega$ impedance. Dashed lines indicate the fundamental digitization noise limit for both devices.

noise as fundamental lower limit for both devices. These estimates [132] are based on

$$\tilde{U}^{\text{dig}} = \frac{U_{\text{LSB}}}{\sqrt{6 \cdot f_{\text{BW}}}} \quad (9.5)$$

with U_{LSB} denoting the voltage equivalent of the *Least-Significant-Bit*²⁵ and f_{BW} being the acquisition bandwidth.

For the integration into the ALPS Slow Control System a DOOCS interface has been implemented allowing to configure and control the acquisition with the ATS9626, even remotely.

9.2.3 | Summary and current state

This section described the implementation and commissioning of a new fast DAQ system for the Transition Edge Sensor.

On the software side, a versatile and performant acquisition framework has been implemented making use of the parallel processing capabilities of the DAQ card itself as well as the host computer it is installed in. On the hardware side an external trigger realized by a chain of NIM modules has been assembled and tested, demonstrating its performance is well-suited for the expected trigger rate of TES events.

The new DAQ system is superior over the previously used oscilloscope in terms of resolution (time and voltage), data handling and baseline noise and has smoothly been integrated into the ALPS Slow Control System.

²⁵i.e. the smallest representable voltage step

The FAST framework

The glory of creation is in its infinite diversity.

GENE RODDENBERRY

The Framework for Analysis and Simulation of Transition edge sensors (FAST) is a toolset developed in the course of this thesis providing easy and performant processing capabilities for all kinds of TES acquired data. Built on top of the newly established data acquisition system (see Sec. 9.2), it concludes the task for a complete environment for the detection of reconverged photons starting with the detector interface to the optical setup (cf. Cha. 8), acquiring the detector's data output (cf. Sec. 9.2) and finally, the processing and analysis of this data, described in the following.

FAST uses the format produced by the acquisition framework¹ as underlying data type, but also provides tools for converting legacy data as acquired by the previously used oscilloscope. The FAST framework has been published as open source software and is publicly available² for free copy and usage.

In this chapter the three main parts of FAST are described, giving an overview of its performance spectrum and providing real world example applications using actual TES acquired data³. Section 10.1 will start off with the description of the spectrum tools developed in order to infer frequency spectra from TES time series for the analysis of noise contributions. The subsequently following Section 10.2 deals with the generation of simulated TES events and time series, providing a powerful tool for the development and optimization of analysis strategies and algorithms. The last Section 10.3 concludes with the presentation of a novel analysis method implemented in FAST utilizing the tools from the previous parts and contrasting it to previously used strategies.

¹LZMA compressed ROOT trees. See Sec. 9.2 for further reference.

²<https://gitlab.com/weinshec/fast>

³**Important note:** Due to the political issues already mentioned in footnote ⁹ of Chapter 7, the actual detector was not available for the acquisition of new data in combination with the new DAQ system. This is why mostly simulated and only a small part of legacy data is used here in order to demonstrate the FAST framework's performance.

10.1 | Spectrum tools

The chronologically first part of FAST is the group of spectrum tools allowing to perform system noise measurements based on Fast Fourier Transforms (FFTs). Since the nature of TES data is time series, the ability to estimate the general noise contribution is of great importance for optimization and analysis purposes.

10.1.1 | DFT and IDFT

Like in many other real world data acquisition system, the TES data is acquired as a series of data points discrete in time, which is why the mathematical framework of the Discrete Fourier Transform (DFT) is required. In the following, the basic concepts of the DFT and its inverse (IDFT) will be briefly summarized in order to provide a better understanding of implemented tools. The notation and conventions used here mostly follow [133], which also provides a great introduction to DFTs in data analysis applications.

In the common case, like it is described here, the input signal comes as a (real valued) time series of voltage readings digitized by an ADC. Let this series of length N be denoted by x_k with $k \in [0, N - 1]$. The DFT is defined as⁴

$$y_m = \sum_{k=0}^{N-1} x_k e^{-2\pi i \frac{mk}{N}} \quad \text{with } m \in [0, N - 1] \quad (10.1)$$

whereas the inverse transformation (IDFT) is given by

$$x_m = \frac{1}{N} \sum_{k=0}^{N-1} y_k e^{+2\pi i \frac{mk}{N}} \quad \text{with } m \in [0, N - 1] \quad (10.2)$$

The output of the DFT is a series of complex numbers of same length (N). For real valued inputs x_k , one can show that the y_k expose a certain symmetry

$$y_{N-m} = y_m^* \quad (10.3)$$

where $*$ denotes the complex conjugate. Hence, in this case, the *second half* of the series y_k is redundant and will never be computed in efficient implementations. In contrast, the remaining *first half* of complex values corresponds to the content of frequency bins

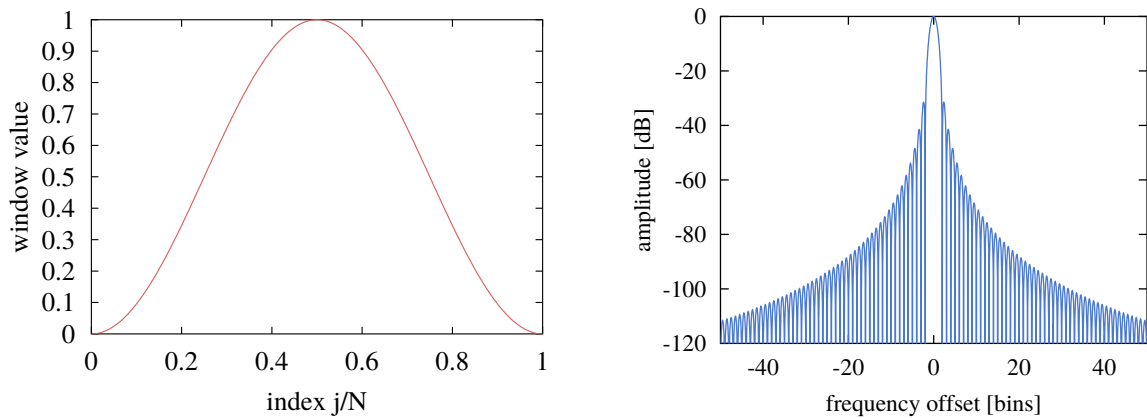
$$f_m = m \frac{f_s}{N} = m f_{\text{res}} \quad \text{with } m \in [0, N/2] \quad (10.4)$$

where f_s denotes the sampling frequency. This goes in line with the Nyquist-Shannon theorem [134], stating that the maximal useful frequency is indeed $f_s/2$. From (10.1) it is further apparent that the f_0 bin represents the DC component of the input signal, as it simply computes

⁴Note that the normalization coefficient of y_m is a matter of convention. Here, 1 has been chosen, but common other examples are $1/\sqrt{N}$ or $1/N$. For the IDFT an appropriate coefficient has to be chosen, such that the overall normalization is valid, i.e. the IDFT of a DFT transformed series has to yield the original series again.

the sum of all values⁵. The according magnitudes of the complex values y_m constitute the signal power contained in the corresponding frequency bin. Nevertheless, there is an intrinsic issue arising from the nature of real world signals.

While the mathematical formulation of the DFT implicitly assumes that the input signal is periodically repeating itself infinitely, the real world signal hardly exposes this symmetry. Hence, there is a (virtual) discontinuity occurring between the first and last value of the input signal, resulting in power spread over the spectrum, contaminating all frequency bins. The solution to this is the application of a *window function* on the time series. The particular choice of the window function to use depends on desired goal and is usually a trade-off between amplitude accuracy and the power leakage to other frequency bins⁶. However, the general working principle is to dissolve the discontinuity issue by suppressing the signal amplitude at the beginning and end of the time series. A common choice for a window function is the *Hanning window* depicted in Figure 10.1.



(a) The Hanning window in the time domain. The tails are suppressing the signal amplitude solving the discontinuity issue.

(b) The Hanning window in the frequency domain. The power leakage to other frequency bins decreases with distance.

Figure 10.1: The Hanning window (taken from [133]).

Each window function defines a set of N weights w_m that are applied on the time series by multiplying them with the corresponding input value of same index. In the example of the Hanning window the weights are given by

$$w_m = \frac{1}{2} \left[1 - \cos \left(\frac{2\pi m}{N} \right) \right] \quad \text{with } m \in [0, N - 1] \quad (10.5)$$

In order to provide the correct scaling of the magnitudes of the complex DFT output values y_k , the applied window function needs to be taken into account. Also when converting spectra to spectral densities, the information about the used window function is required. The *Power*

⁵or the arithmetic mean depending on the chosen DFT/IDFT normalization convention

⁶The appendix of [133] contains a comprehensive collection of window functions and discusses their properties.

Spectrum (PS) and the Power Spectral Density (PSD) of the input signal are obtained via

$$\text{PS}(f_m) = \frac{2 \cdot |y_m|^2}{\left(\sum_{j=0}^{N-1} w_j\right)^2} \quad \text{PSD}(f_m) = \frac{2 \cdot |y_m|^2}{f_s \sum_{j=0}^{N-1} w_j^2} \quad (10.6)$$

whereas the according Linear Spectrum (LS) and Linear Spectral Density (LSD) are given by taking the square root of (10.6) respectively.

10.1.2 | Implementation and verification

The above described formalism is implemented in FAST following what is commonly referred to as Welch's method [135] based on splitting the original time series into smaller parts and averaging over the DFTs of these time slices. This helps to reduce the statistical fluctuations when estimating the spectrum. The individual steps are

1. *Split the time series in slices*
The length of the time slices depends on the desired frequency resolution, i.e. the frequency bin width of the target spectrum.
2. *Remove the DC offset*
The DC offset is subtracted from each input value. The offset is estimated individually for each time slice by calculating the arithmetic mean of the input values in the slice.
3. *Apply the window function*
Calculate the window function weights for the length of the time slices and apply them on each of them. By default the Hanning window is used, but also other choices such as *HFT116D*, *National Instruments flat-top* and the *Blackman-Harris* window are implemented.
4. *Compute the DFT non-redundant magnitudes*
For each time slice the non-redundant magnitudes⁷ are computed using the efficient Fast Fourier Transform of the FFTW package [131].
5. *Average spectrum*
Average the final spectrum from all time slices and apply the correct scaling depending on the used window function.

In order to verify the correct implementation and scaling of the method, a reference sample is provided in [133] allowing to easily test the FAST spectrum tools. A slightly adapted copy of the generating source code can be found in Appendix D. The reference sample contains two sinusoidal signals, one at 1234 Hz with 2.828 V amplitude, the other at 2500 Hz with 1 V amplitude sampled with a sampling frequency of $f_s = 10$ kHz. Further, digitization noise is simulated by rounding the sampled values to $U_{\text{LSB}} = 1$ mV precision at the least significant bit. The resulting spectrum estimated by FAST is shown in Figure 10.2 with the sinusoidal signal peaks clearly visible at the correct position. Further the digitization noise floor is estimated at correct level of $\tilde{U}_{\text{dig}} = 4.08 \mu\text{V}_{\text{rms}}/\sqrt{\text{Hz}}$ as in accordance with Eq. (9.5).

⁷cf. Eq. (10.3)

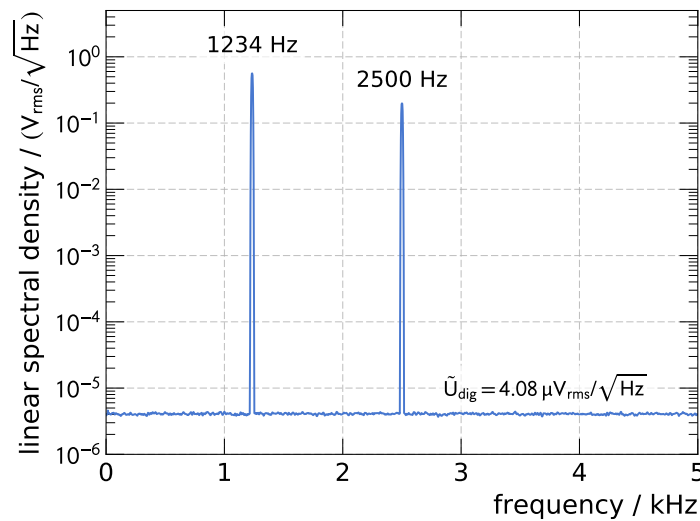


Figure 10.2: Linear spectral density of the test reference sample. The sinusoidal signals at 1234 Hz and 2500 Hz are clearly visible in the spectrum.

For the backward transformation, i.e. the Inverse Discrete Fourier Transform (IDFT), the verification of implementation is simply achieved by calculating the DFT of its output again and comparing the resulting spectrum with the original one.

Moreover, FAST implements an additional method built upon the IDFT that allows to generate random time domain samples following a given frequency spectrum. This is realized by drawing a random complex phase $\phi \in [-\pi, +\pi]$ for each frequency bin keeping its magnitude unaltered and subsequently applying the backward transformation. This way, it is possible to mimic (pseudo-) random noise contributions of a system once its frequency spectrum has been characterized.

10.2 | Simulation

The simulation part of FAST evolves around the generation of artificial TES acquired data in order to provide a handle on testing and optimizing analysis strategies by means of statistical Monte-Carlo methods. One of the main advantages over pure data driven techniques thereby is the availability of *truth information* allowing to directly compare the developed analysis algorithms with.

Unlike a *full* detector simulation — in the classical sense — from the particle interaction level to the readout electronics response, the concept of FAST utilizes a much simpler yet powerful approach exploiting the analytic pulse shape description derived in Section 7.2 and the characterization of the system noise response using the tools described in above. A full detector simulation in contrast would involve many unknown or simply unavailable parameters of the system such as thermal properties of the used materials within mK environments or detailed undisclosed insights into the SQUID readout circuitry. Ultimately, the additional knowledge gain of such simulation does not outweigh the efforts of a long and complicated development process.

10.2.1 | General simulation workflow

The core of the FAST simulation concept is the `Generator` class designed to perform the creation of `GeneratorRecord` instances. The latter one represents the basic entity of simulated data for a single event, i.e. a series of (virtual) ADC readings and all relevant metadata like for example the sampling frequency. Each `GeneratorRecord` is initialized by the `Generator` with a plain vector of preconfigured length filled with zeros. The `Generator` then subsequently applies so-called `Transformation` objects onto each record that alter the data vector following the desired user configuration.

Among the already built-in `Transformation` classes are simple operations such as scaling or shifting the values and even more complex procedures like the imprinting of one or more photon pulses. The list of built-in types is given in Table 10.1. Nonetheless, the user is encouraged to implement his/her own `Transformation` classes for special purposes.

Table 10.1: Implemented `Transformation` types acting on a `GeneratorRecord`.

<code>Transformation</code>	Description	Parameters
<code>AddScalar</code>	Add a scalar to all values, i.e. voltage offset	voltage offset
<code>Multiply</code>	Multiply all values with a scalar constant	factor
<code>TimeShift</code>	Shift the record horizontally i.e. time offset	time offset
<code>AddWhiteNoise</code>	Add a random number to each value obeying a gaussian distribution	std. deviation
<code>AddSpectralNoise</code>	Add a random number to each value obeying a given frequency spectrum	noise LSD
<code>AddPhotonPulse</code>	Add a photon pulse using the analytic description from the small signal theory (cf. Sec. 7.2)	amplitude, rise/fall time, time offset

Each `Transformation` requires one or more user-specified parameters. While these parameters are not necessarily tied to constant values, it is possible to specify random distributions, e.g. gaussian or flat distributions, or even user specified histograms, to randomly draw new parameter values for each `GeneratorRecord`. In any case, the `GeneratorRecord` class is designed to store the currently used values of all parameters during the application of the `Transformation` objects. Like for every Monte-Carlo application the most crucial component is the pseudo-random number generator. In the case of FAST the algorithm by [136] featuring a large repetition period of $2^{19937} - 1$ is used for this purpose. Figure 10.3 illustrates exemplarily the creation of a `GeneratorRecord` containing a photon pulse with random amplitude and time offset and additional gaussian noise.

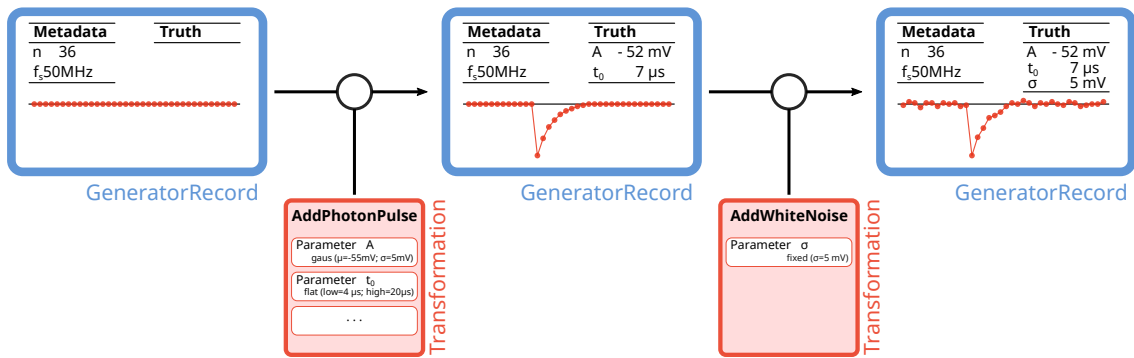


Figure 10.3: Example simulation chain demonstrating the principle of the FAST `Generator`. Every `GeneratorRecord` is initialized as plain vector of zeros and is subsequently altered by `Transformation` objects keeping track of the currently used parameter truth values.

10.2.2 | Simulation of photon events

In order to develop, test and optimize analysis methods for TES acquired data, the usage of simulated events is rewarding, as different conditions in terms of SNR, pulse position and multiple peaks can be well prepared, while the algorithmic results may immediately be compared to the underlying truth information. As already noted in the introduction of Section 10.2, the simulation concept of FAST utilizes the analytic pulse shape based on the TES small signal theory (see Sec. 7.2.1), which has been shown in [98] to be in excellent agreement with the observed pulse shape. Figure 10.4 exemplarily shows the typical pulse shape of a real photon event recorded with the TES.

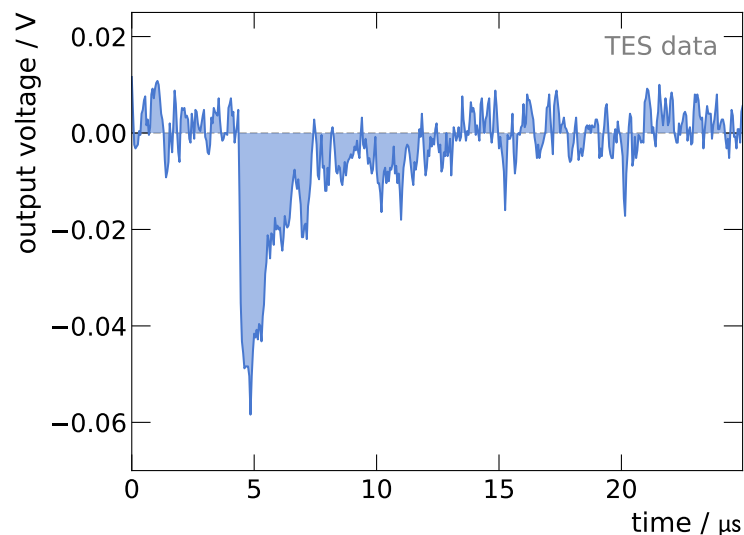


Figure 10.4: Example single photon event originating from a 1064 nm diode laser source, recorded by the TES during CD49. (Compare also with the theoretical TES response shown in Fig. 7.7)

For a realistic simulation of such photon events, a proper description of the systems baseline noise is inevitable. When looking at Figure 10.4, one might already expect that the assumption of solely white gaussian noise is not sustainable in the given case, which is why the FAST spectrum tools (cf. Sec.10.1) were used in order to characterize its actual frequency content. The resulting LSD is shown in Figure 10.5.

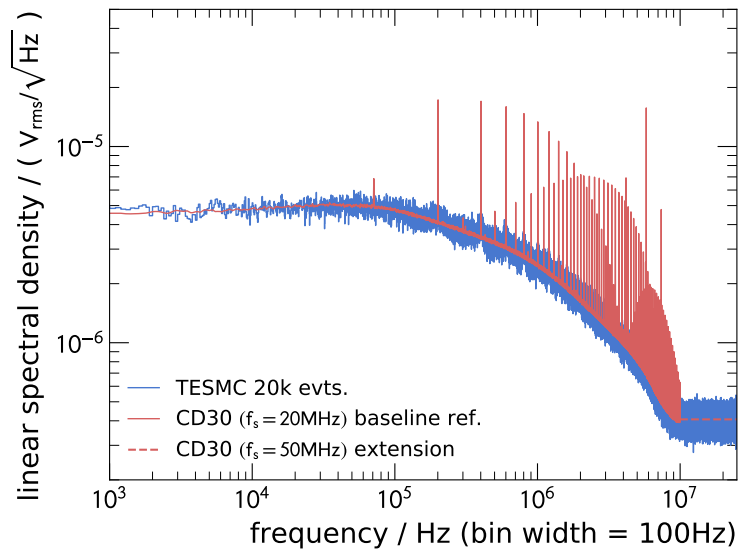


Figure 10.5: Linear Spectral Density from CD30 (solid red) data acquired at $f_s = 20$ MHz used as noise reference in TESMC simulations. The reference spectrum is extended (dashed red) in order to support higher sampling frequencies up to 50 MHz. The blue spectrum represents a closure test spectrum inferred from $2 \cdot 10^4$ pure noise events simulated with the reference noise spectrum.

The dataset used to infer this frequency spectrum is comprised of 40×1 s time series, recorded during CD30 using the oscilloscope at a sampling frequency of 20 MHz. This particular CoolDown has been chosen, as it was conducted without any optical fiber attached to the TES, hence the signal to be read was purely intrinsic system and electronics noise. The clearly visible regular peak structure occurring above 50 kHz in the noise spectrum has already been described by [98] where it was found to originate from the internals of the SQUID electronic readout system.

The obtained LSD is now used as reference spectrum to model the baseline noise, utilizing FAST's `AddSpectralNoise` transformation (cf. Tab. 10.1). However, as time series in legacy data, like CD30, where usually taken at a lower sampling frequency (20 MHz) than triggered photon events (50 MHz), the reference spectrum needs to be artificially extended in order to support the creation of noise samples at the sampling frequency of the latter⁸. Thereby, a flat noise floor above the Nyquist frequency has been conservatively assumed as indicated in Figure 10.5. A closure test, probing the self-consistency of the noise simulation has been performed using $2 \cdot 10^4$ generated pure noise events to estimate the (simulated) frequency content. Figure 10.5 shows the resulting spectrum and indicates a good agreement with the original spectrum.

⁸Note that once the detector is available again, the reference spectrum is remeasured using the new DAQ making this artificial extension obsolete.

10.3 | Analysis

Since the main purpose of the TES in ALPS II is that of a single photon detector, most of the built-in analysis routines of FAST are driven by the concept of event based data. As already mentioned in this Chapter's introduction, the underlying data type used throughout the framework is congruent with the output format of the new DAQ system (cf. Sec. 9.2), in the following simply denoted as *Record*.

The basic idea of processing and analyzing events in FAST revolves around the concept of a `ProcessingUnit`, acting on single Records, extracting information without altering them. The chain of different units strung together then states the analysis workflow. Each `ProcessingUnit` stores its event based result at a predefined location implementing a common interface⁹ for later data access. This way it is ensured, that even huge amounts of data can be efficiently processed by means of parallelization. If a `ProcessingUnit` relies on the result of a preceding unit, it is possible to link them in the event loop. Built-in units involve peak-finding, time-over-threshold, pulse-fitting, etc. discussed later in more detail where appropriate.

10.3.1 | Previously used analysis methods

There are effectively two main analysis strategies presented in previous works [98, 137], which are briefly summarized in this Section, before an alternative approach, newly developed during this work is presented in the following Section 10.3.2.

Height-Integral Analysis

The Height-Integral Analysis (HIA) is a pure numeric method based on two observables, i.e. the Pulse Height (PH) and Pulse Integral (PI). For a given event, those two quantities are defined as

$$\text{PH} = \min[\{U_i\}] \quad \text{PI} = \sum_i U_i \frac{1}{f_s} \quad (10.7)$$

where the index i runs over all data points in the event time window. Transferring this to Figure 10.4, the pulse integral states the blue shaded area between the voltage readings and the 0V line, whereas the pulse height refers to the lowest point occurring at about (5 μ s | -60 mV). Assuming a monochromatic photon source, the signal photons are forming a gaussian ellipse in the PI-PH plane, hence they can be identified by their position in this plane. Though the HIA method is fairly simple both to understand and implement, it also comes with some serious drawbacks. These are, the definition of PH is strongly biased towards smaller voltage values, and further, both observables are highly affected by noise fluctuations and baseline drifts, i.e. a DC offset. Beyond that, it is impossible to discriminate against other signal shapes¹⁰, like e.g. low-energy pileup events or noise glitches that are by chance exhibiting the same integral and height by means of (10.7).

⁹the `TreeLoggable` interface

¹⁰A summary of different pulse shapes observed in actual data is given in [98].

Pulse-Shape Analysis

The Pulse-Shape Analysis (PSA) in contrast is based on a template fit method using *the average* signal pulse shape. The according fit function is defined as

$$f(a, j) = a \cdot \text{avg}[j] \quad (10.8)$$

where a is a global scaling coefficient and $\text{avg}[j]$ denotes the average pulse template shifted by the (discrete) index j . The actual fitting procedure is then implemented by shifting the template within a range of $j = -50 \dots 50$ and for each case, optimizing a using the method of least squares. For a given event, the best matching combination of a and j is obtained and the resulting reduced χ^2 is calculated. Signal photons again manifest as a gaussian ellipse, this time in the a - χ_{red}^2 plane. While the scaling parameter a is equivalent to the pulse height allowing for an energy calibration, the χ_{red}^2 enables discrimination against different pulse shapes. However, the drawbacks of this method are the inherent dependency on the used pulse template and further the discretization of the time shift, i.e. during optimization, the template can only be shifted in discrete steps of $\Delta t = 1/f_s$.

10.3.2 | Pulse-Fitting Analysis

The remaining part of this Chapter is devoted to present a newly developed photon reconstruction strategy for TES acquired data, namely the Pulse-Fitting Analysis (PFA). Meanwhile the above introduced concepts of FAST's processing and analysis capabilities are recapitulated.

Working principle of the PFA

The basic idea of the PFA is to use the analytic TES response description Eq. (7.7), deduced from the *small signal theory* (see Sec. 7.2), and perform an actual least squares minimization fit to the event data. For this purpose, a simplified representation of (7.7) has been defined as follows¹¹

$$f(t) = \begin{cases} \frac{A}{\xi} \left(e^{-\frac{(t-t_0)}{\tau_+}} - e^{-\frac{(t-t_0)}{\tau_-}} \right) + c_0 & , t > t_0 \\ c_0 & , \text{else} \end{cases} \quad (10.9)$$

Here, all material and working point related constants have been encapsulated in the amplitude parameter A , whilst the parameter ξ has been defined as

$$\xi = \left(\frac{\tau_-}{\tau_+} \right)^{\frac{\tau_-}{\tau_+ - \tau_-}} - \left(\frac{\tau_-}{\tau_+} \right)^{\frac{\tau_+}{\tau_+ - \tau_-}} \quad (10.10)$$

This makes the pulse amplitude, independent of the time parameters τ_{\pm} and further allows to intuitively compare the *visual* pulse amplitude with the A parameter. In the original parameterization (7.7), the pulse height is correlated with the rise and fall times τ_{\pm} aggravating the minimization process in the least squares fit. The parameterization (10.9) in contrast exhibits no

¹¹The case differentiation in (10.9) is required as (7.7) is strictly only valid for positive times.

correlation between the amplitude A and the timing parameters, however due to the definition of ξ in (10.10) the correlation now occurs between τ_- and τ_+ , but is found to be easier to couple with for the minimization algorithm. The remaining two parameters t_0 and c_0 denote independent time and voltage offsets respectively. In total, this leaves five parameters to optimize in the least squares minimization (see also Fig. 7.7).

Peakfinding algorithms

The inevitable fact, that the fit function (10.9) is only piecewise defined, bears the problem of non-differentiability at the point $t = t_0$. While this is irrelevant for most applications, it can inherit complications when attempting to fit the function to data by means of the least squares method. Algorithms of this purpose in general utilize the fit functions derivatives during the minimization process, hence being non differentiable might lead to the fit not converging.

Assisting the minimizer¹² by providing a well estimated initial value for t_0 greatly helps to tackle this issue. In order to achieve this, a peakfinding algorithm is required, reliably identifying the pulse positions, including possible multi-pulse events, i.e. events with more than one photon pulse within the events time frame. Each point in time determined this way then states a seed for the actual pulse fit. Therefore the peakfinding algorithm has to be highly sensitive to signal pulses on one hand, while not falsely tagging noise glitches for real pulses on the other hand. Two such algorithms have been investigated so far, one based the first order time-derivative of the event data exploiting the steepness of the pulse's rising edge, and another one based on calculating the cross-correlation of the event data with the analytic pulse shape. The performance of both approaches will be discussed briefly.

The **derivative based peakfinding algorithm** utilizes the concept of *central finite differences* (see Cha. C in the appendix) to compute the first order derivative in time of the event data:

$$\frac{d}{dt}g(i) = \frac{g(i+1) - g(i-1)}{2 \Delta t} \quad (10.11)$$

Due to the steep rising edge of the pulse shape (cf. Fig. 10.4) this results in a large narrow peak in the derivative at the desired pulse position. Due to the inherent system noise, an additional Digital Signal Processor (DSP) low pass filter may be applied before actually computing the derivative¹³. Figure 10.6 shows an example of the derivative peakfinding algorithm on simulated data, with the peak position being correctly identified.

The **cross-correlation based peakfinding algorithm** calculates the cross-correlation coefficient between the event data and the analytic pulse shape (in this context called *kernel*). Illustratively spoken, this is like shifting the analytic pulse shape as template along the time axis, and evaluating its similarity with the event data. Mathematically, this is formulated as

$$(f \circ g)(m) = \sum_{i=-r}^r f(i) \cdot g(m+i) \quad (10.12)$$

¹²Minuit [138] in the case of FAST

¹³The DSP filters are provided to FAST by an external open-source library, that can be found at <https://github.com/vinniefalco/DSPFilters>

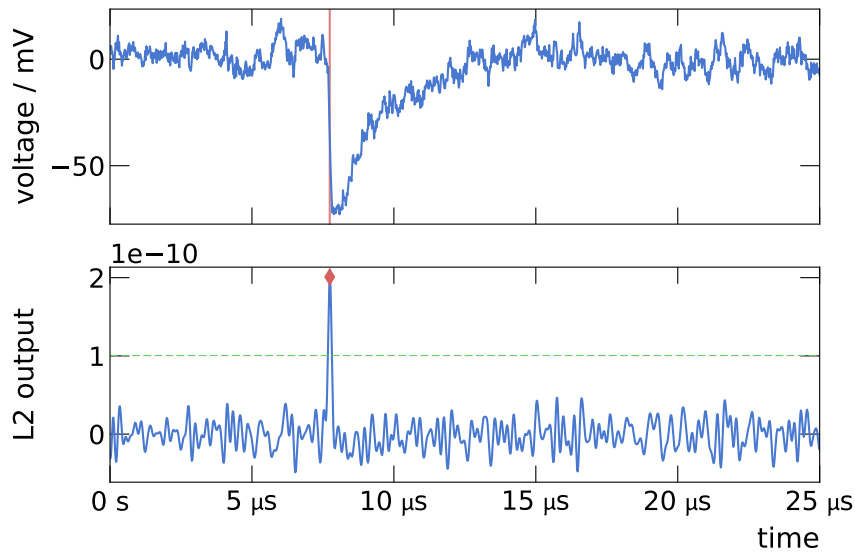


Figure 10.6: Example application of the derivative based peakfinding algorithm using a 5 MHz DSP low pass filter. The top pane shows the original event data frame while the bottom frame displays the output of the (filtered) derivative computation. The photon pulse at 7.5 μs is showing up in the peakfinding output as narrow peak.

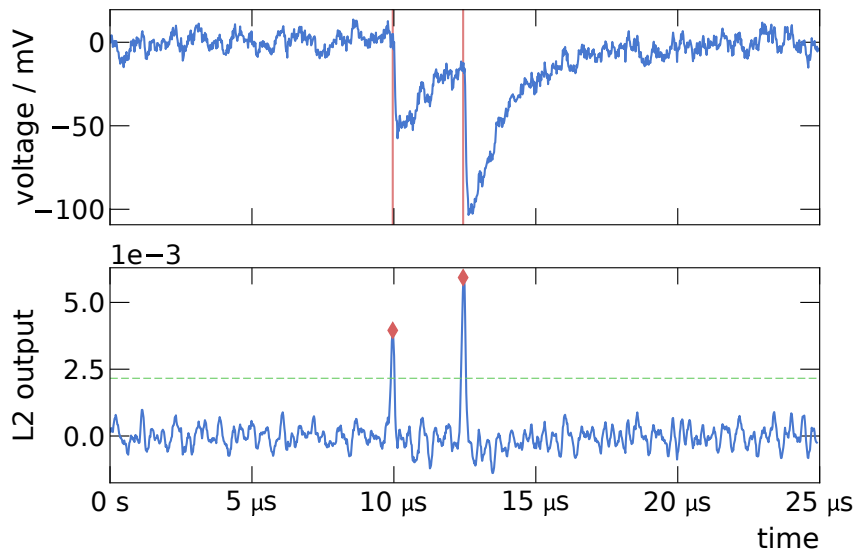
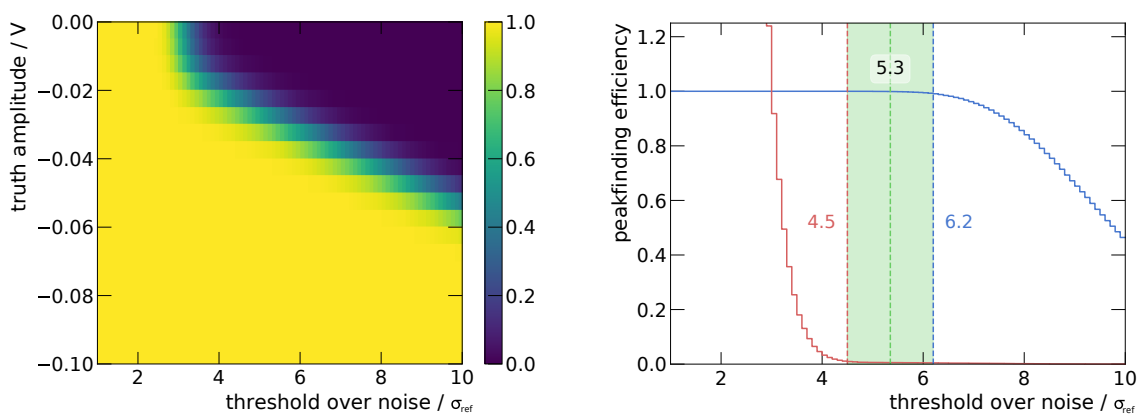


Figure 10.7: Example application of the cross-correlation based peakfinding algorithm using only the first μs of the analytic pulse description as kernel. The top pane shows the original event data frame while the bottom frame displays the output of the cross-correlation computation. Both photon pulses at 10 μs and 12.5 μs have been identified.

with f being the kernel of size $2r + 1$ and g being the original event data. When the kernel is *shifted* over a signal pulse in data, the sum in (10.12) is large, whereas it is small for different shaped patterns. The kernel size is specified by multiples of the analytic pulse shape minimum time, e.g. a kernel size of $1t_{\min}$ refers to the slice between t_0 and the (analytic) pulse minimum. Figure 10.7 shows a simulated pile-up event with the cross-correlation peakfinding algorithm applied.

Both peakfinding algorithms exhibit parameters to be chosen. In the derivative case, this is the cutoff frequency of the low pass filter, while in the cross-correlation case it is the size of the kernel. Both methods further require a threshold above which the local maxima in the peakfinding output is recognized as signal pulse (dashed green line in Fig. 10.6 and Fig. 10.7). This threshold is quantified in terms of standard deviations above the pure noise expectation (see Appendix E). In order to optimize both parameters of both methods with respect to a high signal sensitivity while keeping the chance for falsely identified noise peaks low, a Monte-Carlo sample with 100k events has been generated, featuring a flat pulse amplitude distribution, on which the algorithms are tested. Figure 10.8 exemplarily shows the results of such test for the cross-correlation algorithm with $0.75t_{\min}$ kernel size. The green shaped area in Figure 10.8b is



(a) Probability of correctly identifying the signal photon pulse position depending on its (true) amplitude and the used threshold on the peakfinding algorithm.

(b) 1D-Projection onto the amplitude region for 1064 nm photons. The blue line states the signal pulse identification efficiency, while the red lines represent the rate of additional falsely identified noise peaks.

Figure 10.8: Example results of the cross-correlation peakfinding algorithm with $0.75t_{\min}$ kernel size.

defined as the interval, where the signal pulse identification efficiency is above 99% and the fake noise peak rate is below 1%. The central value in this interval is then subsequently chosen as optimal threshold for this particular algorithm tune. Table 10.2 summarizes the test results for all investigated cases, which already excludes some of the parameter sets, because the algorithm did not exhibit an interval fulfilling the sensitivity criteria given above. In general, the cross-correlation algorithm turns out to be less robust against fake noise peak identification, hence the relatively large fallout ratio. On the derivative algorithm side, it seems that aggressive low pass filtering increases the algorithm's performance. However, care must be taken, as lowering the cutoff frequency progressively washes out features, e.g. a second close-by photon pulse could

Table 10.2: Peakfinding parameter optimization. Cases where $\sigma_{\text{opt}} = -$ do not feature a region matching the given efficiency / fake rate criteria. All $\sigma_{(\cdot)}$ in terms of σ_{ref} (cf. App. E).

(a) derivate				(b) cross-correlation			
$f_{\text{cutOff}}/\text{MHz}$	σ_{fake}	σ_{signal}	σ_{opt}	kern. size/ t_{min}	σ_{fake}	σ_{signal}	σ_{opt}
1	4.0	6.7	5.3	0.5	5.4	5.3	-
2	4.0	6.4	5.2	0.75	4.5	6.2	5.3
3	4.1	6.1	5.1	1.0	6.1	6.4	6.2
4	4.2	5.8	5.0	1.25	9.4	6.8	-
5	4.2	5.6	4.9	1.5	>10	6.8	-
6	4.3	5.3	4.8	2.0	>10	6.9	-
7	4.3	5.1	4.7	3.0	>10	6.9	-
8	4.3	5.0	4.7	4.0	9.5	6.0	-
9	4.4	4.9	4.7	5.0	6.9	4.7	-
∞	6.1	4.0	-	15.0	>10	6.0	-

remain undetected, as its rising edge merges with the first one. This effect can be observed in Figure 10.9, where for both extremes, i.e. low and high frequency cutoff, the efficiency to detect a second accompanying pileup photon is shown as a function of the second photon's amplitude and time difference relative to the occurrence of the first photon. As can be seen, the low cutoff frequency in Figure 10.9a effectively prevents close-by pileup photons from being identified.

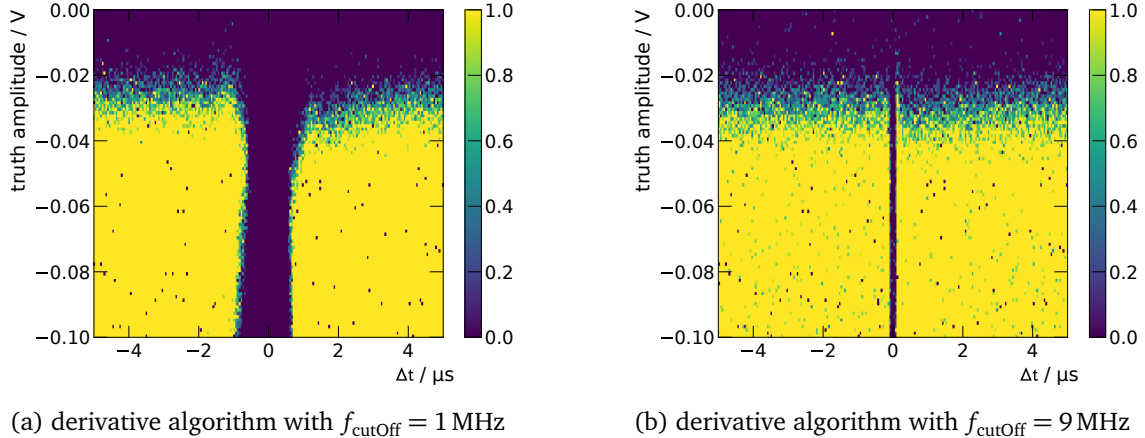


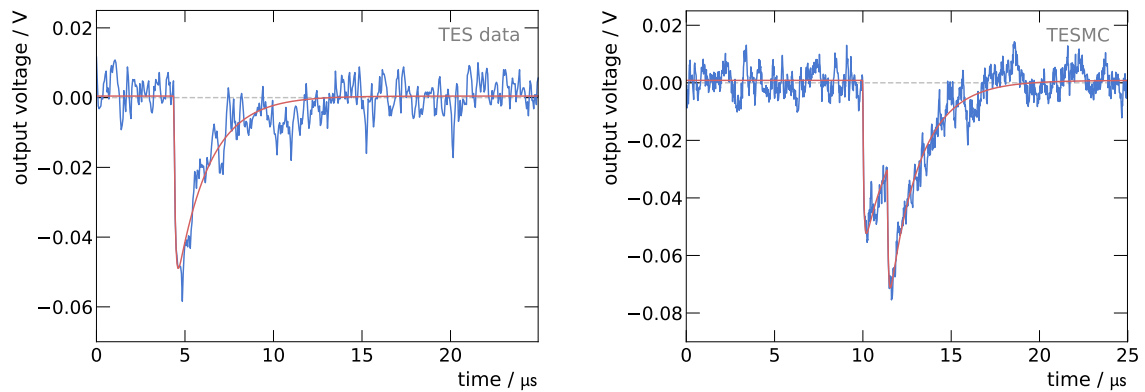
Figure 10.9: Efficiency to detect an accompanying pileup photon as a function of its amplitude and separation in time.

From these considerations, the derivative algorithm using a 5 MHz low pass filter has been chosen, to build the baseline for the further analysis. Note however, that this choice was motivated from the general use case for the identification of 1064 nm photon events. For specialized analysis purposes, the peakfinding algorithm might be optimized in a different way.

In the context of FAST the PFA represents an example of linked `ProcessingUnit` instances, i.e. a first one implementing the peakfinding algorithm (`DerivProcessor` or `XCorrProcessor`) linked to a second one, actually performing the minimization (`PulseFitProcessor`).

Control plots

Once the pulse positions are identified, the actual fitting procedure has everything at hand. The pulse fitting routine initializes an event specific fit function according to the number of identified pulses, using the particular timing position information acquired during peakfinding. Figure 10.10a shows the same event as used in the introduction (Fig. 10.4) overlaid with the fit result. Further Figure 10.10b shows an example of a simulated pileup event, successfully identified and fitted.



(a) Example fit a 1064 nm photon pulse acquired by the TES. (b) Simulated pileup event of two close-by photons.

Figure 10.10: Example resulting fits created using the PFA.

With the PFA in place, it possible to compare observable distributions between the FAST simulation and actual TES data. This is done in so called control plots as shown in Figure 10.11. The used dataset was acquired during CD28 featuring a 1064 nm diode laser as input to the TES and is comprised of 3315 events. The simulated sample instead consists of $1 \cdot 10^4$ events and has

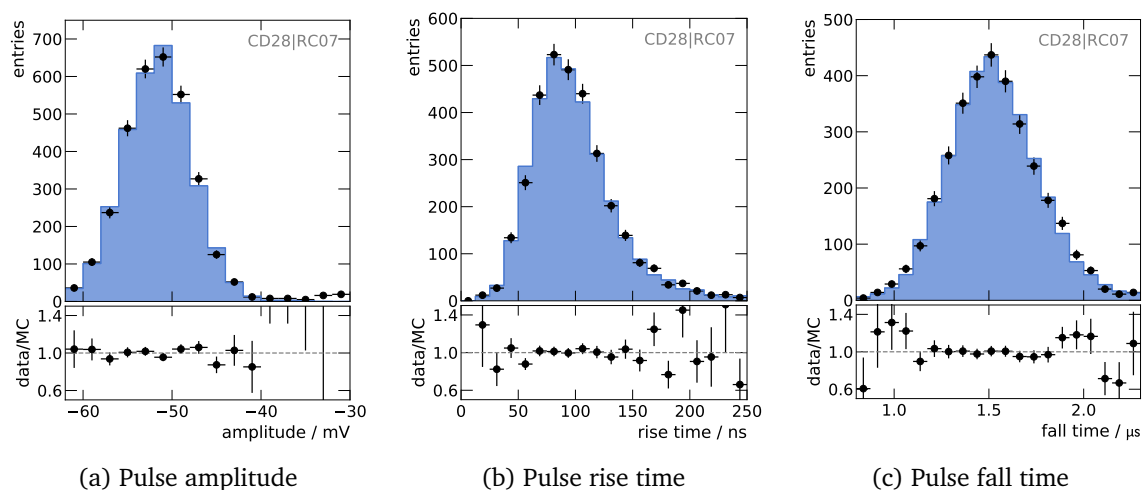


Figure 10.11: Control plots comparing observables between data and simulation, both measured by the PFA. The upper panels show the data (black) and simulation (blue) distributions, while the lower panel their ratio.

been scaled accordingly. As can be seen, all distributions show reasonable agreement between data and simulation in the signal region. Solely, the amplitude distribution shows a systematic deviation on the low energy side of the spectrum, where the data significantly overshoots the simulation expectation. However, these events can be identified with low energetic photons emerging from blackbody radiation just passing the trigger threshold (see also next paragraph).

PFA performance

In order to test the performance of the PFA, a signal sample simulating 1064 nm single photon events has been generated to be analyzed by the PFA. In analogy to the HIA method used in previous works, the pulse amplitude (in HIA called pulse *height*) and integral is determined and compared to the underlying truth value. Figure 10.12 shows the relative deviation of the estimated amplitudes and integrals side-by-side for both methods. It comes as no surprise

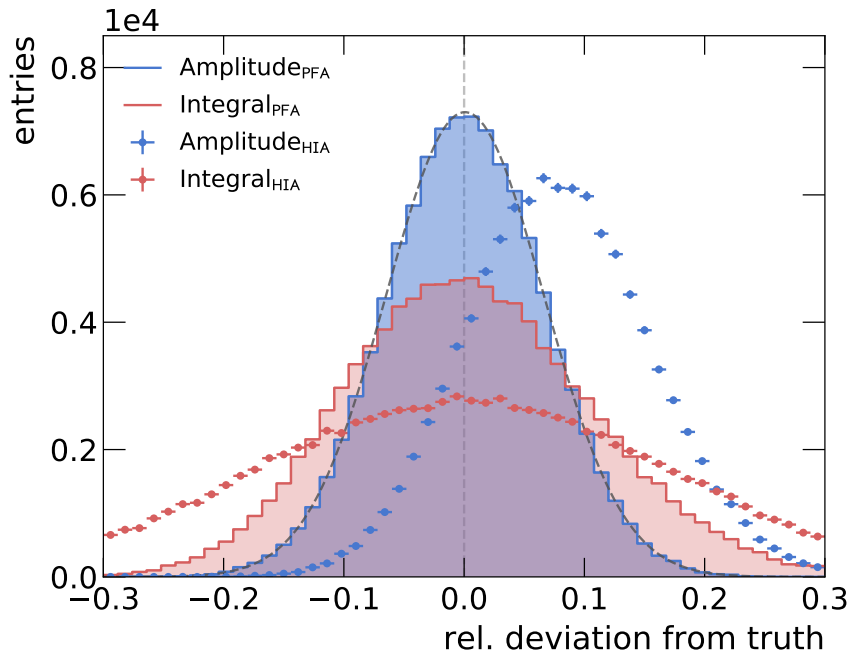


Figure 10.12: Relative deviation of the pulse amplitude and integral estimators of PFA (solid lines) and HIA (dots) from the simulated truth value.

when looking at its definition (10.7), that the amplitude estimator of HIA is biased towards larger values, whereas the corresponding PFA estimator in contrast is centered around the true value. Further it can be seen, that both distributions of the PFA in general have smaller variance compared to the HIA distributions. In the case of the amplitude estimator, this directly translates to the energy resolution. From fitting a gaussian distribution (dashed gray in Fig. 10.12) to the PFA's amplitude histogram, one obtains a relative energy resolution of

$$\left. \frac{\Delta E}{E} \right|_{1064 \text{ nm}}^{(\text{PFA})} \approx (6.5 \pm 0.1)\% \quad (10.13)$$

compared to $(7.1 \pm 0.3)\%$ for the HIA [98]. The PFA's relative energy resolution is compatible with that of the PSA reported in [98] using the somewhat similar template fit method. As opposed to this however, the PFA does not rely on a predefined average pulse, possibly introducing an artificial bias, and in addition yields the full parametric shape information.

In general, now for the first time, the PFA is able to cope with multiple pulses in a single event frame (cf. Fig. 10.9 and Fig. 10.10b), whereas in previous analysis methods, this kind of events has either lead to falsely estimated values, or has remained unseen. Moreover the PFA is able to distinguish different pulse shapes from the obtained time constants, which in future will help to reduce background contributions as being observed by [98]. There, two non-photon shaped populations have been seen, exposing vastly different time constants by 2–3 orders of magnitude. Figure 10.13 shows the distribution of the rise time constant of these types of events together with an example of each fitted by the PFA. The underlying dataset was extracted from

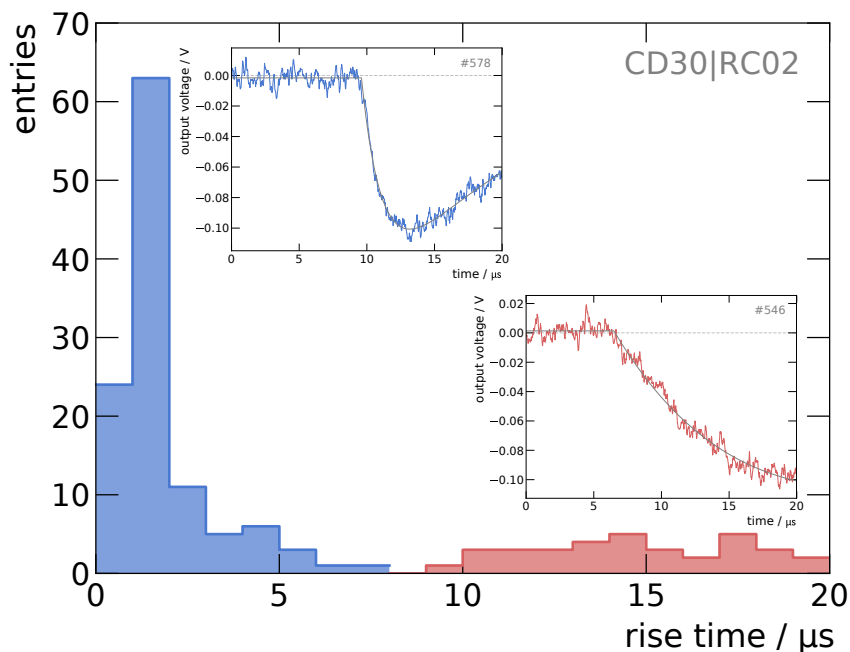


Figure 10.13: Distributions of the pulse rise time for both non-photon like background populations. The inset plots show an example event of each population fitted by the PFA.

legacy data (recorded using the oscilloscope based DAQ), which is why the event time window is not adequate to acquire the full pulse shape. While [98] suspects cosmic muon hits and events induced by ambient radioactivity, the origin of these populations still remains unclear.

Background contributions from low energy photons originating from blackbody radiation being gathered by the warm end of the fiber link have already been seen in [98] and also manifested in Figure 10.11a. However, two almost coincident blackbody photons could mimic a signal event, if their time of occurrence is small enough. This kind of background events will presumably also be tackled by the PFA approach, in particular when using the new DAQ system (cf. Sec. 9.2) exploiting its higher sampling frequency capabilities to disentangle close-by rising edges. In any case, for this particular issue, a filter bench residing inside the cryostat is

currently under evaluation [139], which effectively shields the detector from these background events.

As disadvantage of the PFA, one should quote the necessity of finding the pulse positions in advance to the actual fit, which clearly increases the complexity of the method in general. Further the PFA comes with another signal efficiency attached, though this has been optimized to be close to unity.

Results and prospects

The task is, not so much to see what no one has yet seen; but to think what nobody has yet thought, about that which everybody sees.

ERWIN SCHRÖDINGER

This chapter is devoted to briefly summarize the results of Part III and shows prospects of the development of ALPS II.

The ALPS II experiment is commonly recognized as *the next generation* of LSW type setups. The concept of two overlapping optical cavity modes on the production and regeneration side, drastically enhancing the photon-ALP conversion rate, has never been demonstrated before. Further the most significant impact factor on sensitivity — the magnetic length product — is tremendously enlarged by using the 100 m HERA dipole magnet strings on either side of the optical barrier. All these efforts will enable ALPS II to explore a huge area of the $g_{a\gamma\gamma}$ -mass parameter (see Fig. 7.4) space in a model independent way.

Since the ALPS II experiment is currently in the construction and commissioning phase, the presented work is widely covering technical topics, mostly devoted to the detection of reconverted photons. The novel detector concept of using a TES as micro-calorimeter for the detection of single photons was explored earlier [98], while it was this thesis' subject to develop and implement an integration strategy into the given ALPS II setup. Starting off with the interface between the detector and the Regeneration Cavity (cf. Cha. 8), not only the efficient coupling of signal photons to the optical link has been demonstrated, but also a laser beam diagnostics tool for the estimation of beam size and quality has been developed. Further, a new Data Acquisition system has been built and commissioned (cf. Cha. 9) covering the performant acquisition of TES data and the recording of (slow) environment related data within the framework of a Slow Control System. Lastly, an easy-extensible general purpose data analysis framework built on top of the DAQ system's data format has been implemented (cf. Cha. 10) featuring tools for spectral analysis, simulation and analysis of TES acquired data.

The full ALPS II setup is currently estimated being operational in 2019, mostly dependent on the progress of infrastructural preparations on the experimental site, while the small-scale development stage is expected to run by end of this year. Besides the presented work, the University of Florida is currently investigating an alternative detector concept based on a heterodyne detection scheme [140], that could possibly be integrated within the ALPS II setup complementary to the TES detector. An updated optical design is therefor under consideration allowing both detection concepts to be realized.

Part IV

Summary

Conclusion and outlook

Physical reality is consistent with universal laws. Where the laws do not operate, there is no reality.

SPOCK

The Axion, or more general ALPs, are a theoretically well motivated hypothetical new particles frequently arising in BSM extensions of the Standard Model (cf. Cha. 1). If existent, they could provide natural solutions to longstanding problems of the SM, including the strong CP-problem and the nature of dark matter. So far ALPs have evaded all attempts of detection, though various experiments are actively conducting searches most commonly exploiting the effective di-photon coupling inherit to all ALP models (cf. Cha. 2). The type of experiment subject to this thesis is the concept of LSW setups utilizing laser beams and strong magnetic fields in order to create and detect ALPs, namely OSQAR and ALPS II.

The OSQAR experiment based at CERN in Geneva utilizes the most basic concept of an LSW type setup, i.e. a laser beam propagating in a single pass through a magnetic dipole field, and further a single dipole magnet on the regeneration side equipped with a stock CCD for reconvered photon detection (cf. Cha. 4). Though relatively simple, due to the large magnetic length product provided by the used LHC dipoles, OSQAR gains significant sensitivity. In this thesis, the recent LSW data run conducted in 2014 was analyzed (cf. Cha. 5), and no significant signal excess over the background estimation could have been found. Hence, exclusion limits constraining the allowed parameter space have been derived (cf. Cha. 6) providing up until today the most stringent model-independent limits on ALPs. Near-future developments of OSQAR foresee the integration of an optical resonator on the production side in order to increase the circulating power.

The ALPS II experiment as successor of the pioneering ALPS I is currently being constructed at DESY in Hamburg. Its design incorporates advanced optical techniques enhancing the photon-ALP conversion rate/probability by two orders of magnitude compared to *single pass* setups (cf. Cha. 7). Further the installation of two large strings of HERA dipole magnets is providing a magnetic length product never achieved before. This thesis focused on the integration of the

novel TES detector concept into the experimental setup by means of establishing an efficient optical interface between the detector and the rest of the experiment (cf. Cha. 8), implementing a slow and fast data acquisition system (cf. Cha. 9) and the development of a simulation and analysis framework for the acquired data (cf. Cha. 10). The first full setup data run is expected to be conducted in 2019.

Besides the two presented experiments, further proposals have evolved providing complementary sensitivity in the ALP parameter space. The following list only provides a few selected examples:

- The probably most straightforward approach is envisioned by [141] and carries the working title ALPS III. The main differences compared to ALPS II thereby is the usage of Future Circular Collider (FCC) dipole magnets providing 13 T in a string of 426 m length. In combination with similar but slightly improved optics this would increase the sensitivity by a factor of 30 compared to ALPS II.
- The next generation of *helioscopes* (cf. Sec. 2.2) goes under the name of the International Axion Observatory (IAXO) [142]. The key concept here in contrast to its predecessor CAST is the design and development of a new toroidal superconducting magnet featuring eight bores with 20 m length and a peak magnetic field strength of 5.4 T. In total, the design sensitivity of IAXO will surpass the recent CAST sensitivity by about 1.0 to 1.5 orders of magnitude in $g_{a\gamma\gamma}$.
- A novel concept of so-called *dish antenna* experiments is proposed [143] fitting into the category of *haloscopes* (cf. Sec. 2.4). The basic idea thereby is fact that a magnetized mirror, i.e. a mirror within a magnetic field, emits photons originating from the conversion of ALPs from the galactic ALP/DM halo. Using a spherically curved mirror leads to focusing the reconverted photons onto the spheres center, where a broadband receiver resides. This way, the narrow mass band limitation of previous haloscope searches is removed while still providing a relatively high sensitivity on $g_{a\gamma\gamma}$.
- Also falling into the group of *haloscope searches* is the Cosmic Axion Spin Precession Experiment (CASPr) [144]. In this approach a pre-polarized insulating material is placed within an external magnetic field having an additional electric field applied perpendicular to that. The resulting magnetization precesses at an angle around the B-field with Larmor frequency if solely originating from the materials static electric dipole moment. However, due to the interaction of the materials nuclei with the galactic ALP/DM halo, the electric dipole moment alters, changing the magnetization precession. By means of precision magnetometry this change can be detected allowing to search for ALPs with masses below 10^{-9} eV in the proposed setup.

The field of Axion/ALP physics is gaining more and more interest in the recent years, especially as up until today no evidence of BSM physics has shown at the LHC. In this spirit, a notable spectrum of new experiments has either been proposed or is already on the way to explore what is possibly hiding at the low energy frontier.

Appendix



Heterodyne detection

Beside the TES single photon detector, the *heterodyne* detection scheme states an alternative approach for detecting the ultra low flux of the reconverted photons in ALPS II.

The main idea is to overlap the detectable signal of reconverted photons on the regeneration side with a *local oscillator* field of slightly different frequency. Due to the interference between both fields, an observable beat signal is created carrying amplitude and phase information of the photon signal to be detected. Since the frequency of the photon signal is precisely known (cf. Sec. 2.1), the amplitude information encoded in the beat note can be obtained by means of demodulation techniques.

One of the advantages thereby is, that the resulting beat note can be measured using a conventional photodetector. In the proposed realization, the photodetector is digitized via an ADC on-board an FPGA card for processing. The acquired signal is then multiplied separately by a sine and cosine of same frequency creating two observable quantities

$$I \propto A \sin \phi \quad Q \propto A \cos \phi \quad (\text{A.1})$$

where A is the desired signal amplitude of reconverted photons and ϕ a constant phase difference. Even though ϕ is not known, integrating I and Q and summing them in quadrature allows for a measurement of A . The quantity of interest thereby is defined as

$$\frac{\sqrt{\left(\sum_{n=1}^N I\right)^2 + \left(\sum_{n=1}^N Q\right)^2}}{\sqrt{N}} \quad (\text{A.2})$$

where N is the total number of acquired samples. If no coherent photon signal is present, i.e. $A = 0$, and only incoherent noise is contributing, this quantity is flat when plotted versus N . However, in case of $A \neq 0$, it can be shown that (A.2) is proportional to A and thus it rises with \sqrt{N} out of the flat noise floor.

This scheme is currently developed and tested at the University of Florida and an updated optical scheme for ALPS II is proposed to allow for both systems, i.e. TES and heterodyne detection, as complementary options.

B

DS18B20 calibration coefficients

The following table shows the calibration coefficients for all DS18B20 temperature sensors that were available during the calibration run using the climate chamber.

Table B.1: Calibration coefficients for the DS18B20 temperature sensors.

sensor ROM	linear	constant / °C
28-000067a3e79	1.013 ± 0.001	-0.207 ± 0.022
28-000067a4268	1.007 ± 0.001	0.016 ± 0.017
28-000067a7b22	1.009 ± 0.001	-0.095 ± 0.018
28-000067c0540	1.008 ± 0.001	-0.084 ± 0.022
28-000067c3014	1.017 ± 0.001	-0.288 ± 0.021
28-000067c4cef	1.005 ± 0.001	-0.062 ± 0.022
28-000067c6a3b	1.010 ± 0.001	-0.079 ± 0.021
28-000067cb521	1.011 ± 0.001	-0.131 ± 0.025

The coefficients are stored within the DOOCS device server and are automatically applied when a new temperature reading is acquired.

C

Finite differences

The mathematical concept of finite differences [145, 146] can be used to evaluate the derivative of a discrete series of data points by means of numerical approximation.

Let $x_i = i\Delta x$ with $i \in [0, N]$ be the sampling points with constant spacing Δx . Further let $u_i = u(x_i)$ be the value of the data point at position x_i (see Figure C.1).

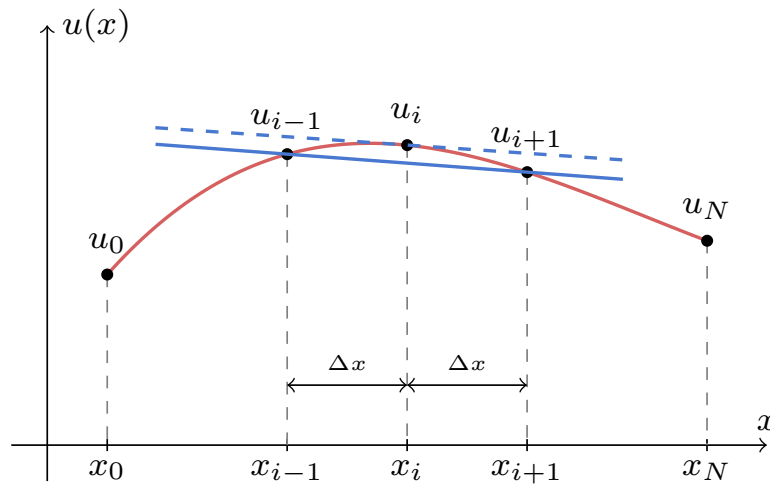


Figure C.1: Illustration of a central finite difference (solid blue) in comparison with the accurate derivative (dashed blue).

Assuming $u(x)$ to be differentiable, the first order derivative at point x by definition is given as

$$\frac{\partial u}{\partial x}(x) = \lim_{\Delta x \rightarrow 0} \frac{u(x + \Delta x) - u(x)}{\Delta x} = \lim_{\Delta x \rightarrow 0} \frac{u(x) - u(x - \Delta x)}{\Delta x} \quad (\text{C.1})$$

$$= \lim_{\Delta x \rightarrow 0} \frac{u(x + \Delta x) - u(x - \Delta x)}{2\Delta x} \quad (\text{C.2})$$

For discretely sampled data this can be approximated by the *central finite difference* (cf. Figure C.1

and compare the solid and dashed blue lines as example)

$$\left(\frac{\partial u}{\partial x}\right)_i \approx \frac{u_{i+1} - u_{i-1}}{2\Delta x} \quad (\text{C.3})$$

From the Taylor expansion $u(x) = \sum_{n=0}^{\infty} \frac{(x-x_i)^n}{n!} \left(\frac{\partial^n u}{\partial x^n}\right)_i$ it is possible to estimate the approximation error of the central finite difference, which is

$$\left(\frac{\partial u}{\partial x}\right)_i = \underbrace{\frac{u_{i+1} - u_{i-1}}{2\Delta x}}_{\text{central difference}} - \underbrace{\frac{(\Delta x)^2}{6} \left(\frac{\partial^3 u}{\partial x^3}\right)_i}_{\text{truncation error } \mathcal{O}(\Delta x)^2} + \dots \quad (\text{C.4})$$

In the limit of vanishing data point spacing Δx , the truncation error goes to zero and the accurate derivative is reproduced.

At the first and last data point of the discrete series, it is not possible to calculate the central finite difference, which is why here, the one-sided *forward* and *backward* differences are used instead:

$$\underbrace{\left(\frac{\partial u}{\partial x}\right)_0 \approx \frac{u_1 - u_0}{\Delta x} + \mathcal{O}(\Delta x)}_{\text{forward difference}} \quad \underbrace{\left(\frac{\partial u}{\partial x}\right)_N \approx \frac{u_{N-1} - u_N}{\Delta x} + \mathcal{O}(\Delta x)}_{\text{backward difference}} \quad (\text{C.5})$$

However, in these special cases, the truncation error scales linearly with the data point spacing Δx .



DFT reference sample code

The C++-code used to generate the DFT reference sample. Adapted from [133].

```
1  #include <stdio.h>
2  #include <math.h>
3  #include "TH1D.h"
4  #include "TFile.h"
5
6  #define TWOPI 6.28318530717959
7
8  void heinzel() {
9      double fs = 10000;           // sampling frequency [Hz]
10     double f1 = 1234;           // first signal frequency
11     double amp1 = 2.82842712474619; // 2 Vrms
12     double f2 = 2500.2157;     // second signal frequency
13     double amp2 = 1;           // 0.707 Vrms
14     double ulsb = 1e-3;        // value of 1 LSB in Volt
15     double N = 1000000;        // number of datapoints
16
17     TFile file("heinzel.root", "RECREATE");
18     TH1D sample("hHeinzel", "hHeinzel", N, 0, N/fs);
19
20     double t, u, ur;
21     for (int i = 0; i < N; i++) {
22         t = (double) i / fs;
23         u = amp1 * sin(TWOPI*f1*t) + amp2 * sin(TWOPI*f2*t);
24         ur = floor(u / ulsb + 0.5) * ulsb;
25         sample.SetBinContent(i+1, ur);
26     }
27
28     sample.Write();
29     file.Close();
30 }
```

E |

Peakfinding noise reference

The peakfinding algorithms used in FAST to locate signal pulses in time require a discrimination threshold above which the algorithms output is recognised as signal pulse candidate (see Section 10.3.2). This threshold is quantified in multiples of the standard deviation σ of the algorithms output on pure baseline noise.

Therefore, both algorithms have been applied on 1000 pure baseline noise events and the according output histograms have been fitted using a gaussian distribution function to estimate the standard deviation. Figure E.1 shows an example of the *derivative* based peakfinding algorithm applied on such pure noise event.

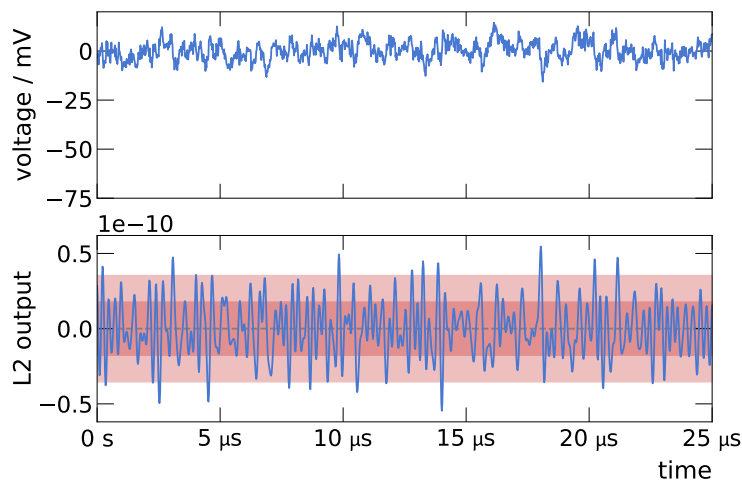


Figure E.1: Derivative based peakfinding algorithm using a 5 MHz cutoff frequency applied on a pure noise event. The upper panel shows the original (noise) data while the lower panel shows the output of the algorithm. The red bands indicate the 1σ and 2σ bands of the output.

For each configuration of both algorithms the standard deviation from noise events is calculated and serves as reference for all later applications of the peakfinding algorithms. Table E.1 summarizes the resulting values.

Table E.1: Peakfinding algorithm standard deviation references from pure noise events.

(a) derivative based peakfinding

$f_{\text{cutOff}}/\text{MHz}$	$\sigma_{\text{ref}} @ f_s = 20 \text{ MHz}$	$\sigma_{\text{ref}} @ f_s = 50 \text{ MHz}$
1	0.2431e-10	0.3924e-11
2	0.4950e-10	0.8197e-11
3	0.6965e-10	1.1682e-11
4	0.8550e-10	1.4856e-11
5	0.9763e-10	1.7696e-11
6	1.0618e-10	2.0171e-11
7	1.1139e-10	2.2236e-11
8	1.1365e-10	2.3841e-11
9	1.1442e-10	2.5157e-11
∞	1.1456e-10	3.6225e-11

(b) cross-correlation based peakfinding

kern. size/ t_{min}	$\sigma_{\text{ref}} @ f_s = 20 \text{ MHz}$	$\sigma_{\text{ref}} @ f_s = 50 \text{ MHz}$
0.5	0.1074e-3	0.1217e-3
0.75	0.1074e-3	0.2836e-3
1.0	0.1930e-3	0.3485e-3
1.25	0.1930e-3	0.4418e-3
1.5	0.2424e-3	0.4719e-3
2.0	0.2651e-3	0.5153e-3
3.0	0.2729e-3	0.5213e-3
4.0	0.2926e-3	0.5885e-3
5.0	0.3447e-3	0.7900e-3
15.0	1.4288e-3	3.6508e-3

Acronyms

ADC	Analog/Digital-Converter
ADR	Adiabatic Demagnetization Refrigerator
ADU	Analog Digital Unit
ALP	Axion-Like Particle
ALPS	Any Light Particle Search
AOM	Acousto-Optic Modulator
API	Application Programming Interface
BSM	Beyond Standard Model
CASPr	Cosmic Axion Spin Precession Experiment
CAST	CERN Axion Solar Telescope
CCD	Charge-Coupled Device
CD	CoolDown
CDF	Cumulative Distribution Function
CDM	Cold Dark Matter
CERN	Conseil Européen pour la Recherche Nucléaire
CPU	Central Processing Unit
DAQ	Data Acquisition
DC	Direct Current
DESY	Deutsches Elektron-Synchrotron
DFT	Discrete Fourier Transform
DHCP	Dynamic Host Configuration Protocol
DM	Dark Matter
DMA	Direct Memory Access
DNS	Domain Name System
DOOCS	Distributed Object-Oriented Control System
DSP	Digital Signal Processor
DWS	Differential Wavefront Sensing
EBL	Extragalactic Background Light

ENS	Equipment Name Server
EOM	Electro-Optic Modulator
FAA	Ferric Ammonium Alum
FAST	Framework for Analysis and Simulation of Transition edge sensors
FCC	Future Circular Collider
FFT	Fast Fourier Transform
FIFO	First In First Out
FPGA	Field Programmable Gate Array
GGC	Galactic Globular Cluster
GGG	Gadolinium Gallium Garnet
GUI	Graphical User Interface
HDD	Hard Disk Drive
HEP	High Energy Physics
HERA	Hadron Elektron Ringanlage
HIA	Height-Integral Analysis
HP	Hidden Photon
IAXO	International Axion Observatory
IC	Integrated Circuit
IDFT	Inverse Discrete Fourier Transform
LAN	Local Area Network
LHC	Large Hadron Collider
LS	Linear Spectrum
LSD	Linear Spectral Density
LSW	Light Shining through a Wall
LVTTL	Low Voltage Transistor-Transistor Logic
MCMC	Markov Chain Monte-Carlo
MOSFET	Metal-Oxide-Semiconductor Field-Effect Transistor
MLE	Maximum Likelihood Estimator
NIM	Nuclear Instrumentation Standards
NIST	National Institute of Standards and Technology
NTP	Network Time Protocol
OSQAR	Optical Search for QED vacuum birefringence, Axions and photon Regeneration
OWFS	1-Wire Filesystem
PC	Production Cavity

PCB	Printed-Circuit-Board
PDG	Particle Data Group
PDH	Pound-Drever-Hall
PFA	Pulse-Fitting Analysis
PH	Pulse Height
PI	Pulse Integral
PS	Power Spectrum
PSA	Pulse-Shape Analysis
PSD	Power Spectral Density
PTB	Physikalisch-Technische Bundesanstalt
RAM	Random Access Memory
RC	Regeneration Cavity
RH	Relative Humidity
RPC	Remote Procedure Call
SCS	Slow Control System
SHG	Second Harmonic Generation
SM	Standard Model
SMF	Single Mode Fiber
SNR	Signal-to-Noise Ratio
SQUID	Superconducting Quantum Interference Device
SUSY	Supersymmetry
TDR	Technical Design Report
TES	Transition Edge Sensor
TESMC	TES Monte-Carlo
QCD	Quantum Chromodynamics
QED	Quantum Electrodynamics
QFT	Quantum Field Theory
QPD	Quadrant Photodiode
USB	Universal Serial Bus
USS	United Starship
VEV	Vacuum Expectation Value
VMB	Vacuum Magnetic Birefringence
WISP	Weakly Interacting Slim Particle

List of Figures

2.1	Relevant feynman diagrams for LSW experiments.	12
2.2	Eigenmodes of the Production Cavity (PC) and Regeneration Cavity (RC) for the resonantly enhanced ALP-photon conversion.	13
2.3	Solar ALP flux assuming a coupling constant of $g_{a\gamma\gamma} = 1 \cdot 10^{-10} \text{ GeV}^{-1}$ calculated using a modern solar model from 2004 and an older model from 1982.	15
2.4	Principle of heterodyne detection of small birefringence and dichroism signals.	15
2.5	Summary of Axion-Like Particle exclusion limits created with the ALPlot web application.	18
4.1	OSQAR experimental site located in the SM18 magnet test facility hall at CERN.	24
4.2	Schematic cross-section of the LHC dipole magnets.	24
4.3	Representation of a single run in the HDF5 format.	26
5.1	Signal region inference from beam position frames.	28
5.2	Baseline correction weight map for the second frame of Run 90.	31
5.3	Cosmic ray hits on a long-exposed frame of Run 90.	31
5.4	Background distribution and signal yield of Run 90.	32
5.5	Consistency check of the full analysis workflow including all corrections and statistical methods.	34
5.6	Posterior distributions of the signal count rate.	35
5.7	Exclusion limits at the 95 % level for scalar and pseudoscalar ALPs.	36
7.1	Schematic view of the ALPS I setup.	42
7.2	Schematic cross-section of a standard HERA dipole magnet.	43
7.3	Simplified schematic of the ALPS II optics concept including control loops. . .	44
7.4	Expected sensitivity of ALPS II in the ALP parameter space.	46
7.5	Illustrative plot of the <i>transition edge</i> of the TES.	47
7.6	Equivalent representations of the electric circuit used to operate a TES in biased mode.	48
7.7	TES current response as given by Eq. (7.7).	50
7.8	Optical stack of the NIST TES optimized for the transmission of 1064 nm photons.	51
7.9	TES detector module assembly.	51
7.10	Schematic cross-section of the Adiabatic Demagnetization Refrigerator from Entropy.	52
8.1	Gaussian beam profile and propagation.	55

8.2	Examples of higher order modes in the Hermite-Gauss and the Laguerre-Gauss set of modes.	55
8.3	Cross-section and mode field distribution of a step-index SMF.	56
8.4	Plot of an exemplary power distribution for a perfect gaussian beam.	57
8.5	Render view of the Knife-Edge beam profiling device. The red arrows indicate the possible directions of motion.	58
8.6	Screenshots of the Knife-Edge acquisition and control software GUI.	59
8.7	Calibration of the Thorlabs MTS50 motorized stage correcting the internal scale for the actual position.	60
8.8	Comparison measurement between the Knife-Edge device and a commercial beam profiler (WinCam).	60
8.9	Theoretical coupling efficiency for various effects of degradation.	62
8.10	Schematic view of the free space to fiber coupling setup.	63
9.1	Concpetual design of the DOOCS architecture.	67
9.2	Packaging options and deployment example of the DS18B20 temperature sensor.	69
9.3	Hardware wiring for the software designed 1-wire master requiring only a pas- sive pull-up resistor.	70
9.4	Rising flank on the 1-wire bus at the end of a “0 bit” for different realizations of the pull-up resistor.	71
9.5	Schematics of the 1-wire master using the DS2482–100 bridge device and an external MOSFET for strong pull-up.	72
9.6	1-wire master hardware shield mounted on a Raspberry Pi.	72
9.7	Example calibration of a DS18B20 temperature sensor against the high precision temperature probe.	73
9.8	ALPS climate board for relative air humidity and temperature monitoring com- pliant with the 1-wire bus system.	74
9.9	ALPSnet network infrastructure.	75
9.10	DOOCS status panel visualizing the current temperature and humidity readings from the 1-wire bus system.	77
9.11	Schematic working principle (simplified) of the DAQ framework.	78
9.12	A 10 Hz test signal recorded by the ATS9626 in <i>continuous mode</i> sampling with 20 MHz.	81
9.13	Schematic view of the NIM crate used as external trigger to record TES events with the ATS9626 data acquisition card.	82
9.14	Trigger efficiency of the external NIM trigger.	83
9.15	Baseline noise spectra of the ATS9626 compared to the previously used oscillo- scope.	84
10.1	The Hanning window.	87
10.2	Linear spectral density of the test reference sample.	89
10.3	Example simulation chain demonstrating the principle of the FAST Generator	91
10.4	Example single photon event originating from a 1064 nm diode laser source, recorded by the TES during CD49.	91

10.5	Linear Spectral Density from CD30 data acquired at $f_s = 20$ MHz used as noise reference in TESMC simulations.	92
10.6	Example application of the derivative based peakfinding algorithm using a 5 MHz DSP low pass filter.	96
10.7	Example application of the cross-correlation based peakfinding algorithm using only the first μ s of the analytic pulse description as kernel.	96
10.8	Example results of the cross-correlation peakfinding algorithm with $0.75t_{\min}$ kernel size.	97
10.9	Efficiency to detect an accompanying pileup photon as a function of its amplitude and separation in time.	98
10.10	Example resulting fits created using the PFA.	99
10.11	Control plots comparing observables between data and simulation, both measured by the PFA.	99
10.12	Relative deviation of the pulse amplitude and integral estimators of PFA and HIA from the simulated truth value.	100
10.13	Distributions of the pulse rise time for both non-photon like background populations.	101
C.1	Illustration of a central finite difference in comparison with the accurate derivative.	113
E.1	Derivative based peakfinding algorithm using a 5 MHz cutoff frequency applied on a pure noise event.	116

List of Tables

1.1	Gauge groups of the Standard Model and the according vector bosons.	5
5.1	Reasons to exclude runs from the analysis.	33
5.2	Excluded rates of reconverted photons for (pseudo-) scalar ALPs.	36
7.1	Sensitivity gain of ALPS II due the optics related changes compared to ALPS I. .	45
9.1	Devices integrated into the SCS and the according tasks performed by the DOOCS device servers.	76
9.2	Characteristics of the Alazar ATS9626 waveform digitizer card used for TES data acquisition.	78
9.3	Estimated parameters of the trigger efficiency turn-on curve fit.	83
10.1	Implemented Transformation types acting on a GeneratorRecord	90
10.2	Peakfinding parameter optimization.	98
B.1	Calibration coefficients for the DS18B20 temperature sensors.	112
E.1	Peakfinding algorithm standard deviation references from pure noise events. . .	117

Bibliography

- [1] Sheldon L. Glashow. “Partial-symmetries of weak interactions”. In: *Nuclear Physics* 22.4 (1961), pp. 579–588. ISSN: 0029-5582. DOI: [http://dx.doi.org/10.1016/0029-5582\(61\)90469-2](http://dx.doi.org/10.1016/0029-5582(61)90469-2).
- [2] Steven Weinberg. “A Model of Leptons”. In: *Phys. Rev. Lett.* 19 (21 Nov. 1967), pp. 1264–1266. DOI: [10.1103/PhysRevLett.19.1264](https://doi.org/10.1103/PhysRevLett.19.1264).
- [3] A. Salam and J.C. Ward. “Electromagnetic and weak interactions”. In: *Physics Letters* 13.2 (1964), pp. 168–171. ISSN: 0031-9163. DOI: [http://dx.doi.org/10.1016/0031-9163\(64\)90711-5](http://dx.doi.org/10.1016/0031-9163(64)90711-5).
- [4] C. Patrignani et al. “Review of Particle Physics”. In: *Chin. Phys.* C40.10 (2016). DOI: [10.1088/1674-1137/40/10/100001](https://doi.org/10.1088/1674-1137/40/10/100001).
- [5] Richard P Feynman. “The Behavior of Hadron Collisions at Extreme Energies”. In: *High Energy Collisions: Third International Conference at Stony Brook* (1969), pp. 237–249.
- [6] Reinhard Alkofer and J. Greensite. “Quark Confinement: The Hard Problem of Hadron Physics”. In: *J. Phys.* G34 (2007), S3. DOI: [10.1088/0954-3899/34/7/S02](https://doi.org/10.1088/0954-3899/34/7/S02). arXiv: [hep-ph/0610365](https://arxiv.org/abs/hep-ph/0610365) [[hep-ph](#)].
- [7] Hermann Minkowski. “Die Grundgleichungen für die elektromagnetischen Vorgänge in bewegten Körpern”. In: *Nachrichten von der Gesellschaft der Wissenschaften zu Göttingen Math-phys. Klasse* (1907), pp. 53–111.
- [8] Noether E. “Invariante Variationsprobleme”. In: *Nachr. D. König. Gesellsch. D. Wiss. Zu Göttingen Math-phys. Klasse* (1918), pp. 235–257.
- [9] H. Georgi. “Lie Algebras In Particle Physics. From Isospin To Unified Theories”. In: *Front. Phys.* 54 (1982), pp. 1–255.
- [10] David Griffiths. *Introduction to Elementary Particles*. second. Wiley-VCH, Aug. 2008.
- [11] C. N. Yang and R. L. Mills. “Conservation of Isotopic Spin and Isotopic Gauge Invariance”. In: *Phys. Rev.* 96 (1 Oct. 1954), pp. 191–195. DOI: [10.1103/PhysRev.96.191](https://doi.org/10.1103/PhysRev.96.191).
- [12] Ivo van Vulpen. *The Standard Model Higgs Boson*. Part of the Lecture Particle Physics II, UvA. Oct. 2013.
- [13] Peter W. Higgs. “Broken Symmetries and the Masses of Gauge Bosons”. In: *Phys. Rev. Lett.* 13 (1964), pp. 508–509. DOI: [10.1103/PhysRevLett.13.508](https://doi.org/10.1103/PhysRevLett.13.508).
- [14] F. Englert and R. Brout. “Broken Symmetry and the Mass of Gauge Vector Mesons”. In: *Phys. Rev. Lett.* 13 (1964), pp. 321–323. DOI: [10.1103/PhysRevLett.13.321](https://doi.org/10.1103/PhysRevLett.13.321).

- [15] G. S. Guralnik, C. R. Hagen, and T. W. B. Kibble. “Global Conservation Laws and Massless Particles”. In: *Phys. Rev. Lett.* 13 (1964), pp. 585–587. DOI: 10.1103/PhysRevLett.13.585.
- [16] A. O. Sushkov et al. “New Experimental Limits on Non-Newtonian Forces in the Micrometer Range”. In: *Phys. Rev. Lett.* 107 (17 Oct. 2011), p. 171101. DOI: 10.1103/PhysRevLett.107.171101.
- [17] Edvige Corbelli and Paolo Salucci. “The Extended Rotation Curve and the Dark Matter Halo of M33”. In: *Mon. Not. Roy. Astron. Soc.* 311 (2000), pp. 441–447. DOI: 10.1046/j.1365-8711.2000.03075.x. arXiv: astro-ph/9909252 [[astro-ph](#)].
- [18] Alexandre Refregier. “Weak gravitational lensing by large scale structure”. In: *Ann. Rev. Astron. Astrophys.* 41 (2003), pp. 645–668. DOI: 10.1146/annurev.astro.41.111302.102207. arXiv: astro-ph/0307212 [[astro-ph](#)].
- [19] P. A. R. Ade et al. “Planck 2015 results. XIII. Cosmological parameters”. In: *Astron. Astrophys.* 594 (2016), A13. DOI: 10.1051/0004-6361/201525830. arXiv: 1502.01589 [[astro-ph.CO](#)].
- [20] P. J. E. Peebles and Bharat Ratra. “The cosmological constant and dark energy”. In: *Rev. Mod. Phys.* 75 (2 Apr. 2003), pp. 559–606. DOI: 10.1103/RevModPhys.75.559.
- [21] Laurent Canetti, Marco Drewes, and Mikhail Shaposhnikov. “Matter and Antimatter in the Universe”. In: *New J. Phys.* 14 (2012), p. 095012. DOI: 10.1088/1367-2630/14/9/095012. arXiv: 1204.4186 [[hep-ph](#)].
- [22] Georges Aad et al. “Observation of a new particle in the search for the Standard Model Higgs boson with the ATLAS detector at the LHC”. In: *Phys. Lett.* B716 (2012), pp. 1–29. DOI: 10.1016/j.physletb.2012.08.020. arXiv: 1207.7214 [[hep-ex](#)].
- [23] Serguei Chatrchyan et al. “Observation of a new boson at a mass of 125 GeV with the CMS experiment at the LHC”. In: *Phys. Lett.* B716 (2012), pp. 30–61. DOI: 10.1016/j.physletb.2012.08.021. arXiv: 1207.7235 [[hep-ex](#)].
- [24] Steven Weinberg. “Implications of Dynamical Symmetry Breaking”. In: *Phys. Rev.* D13 (1976), pp. 974–996. DOI: 10.1103/PhysRevD.13.974.
- [25] E. Gildener. “Gauge-symmetry hierarchies”. In: *Phys. Rev. D* 14 (Sept. 1976), pp. 1667–1672. DOI: 10.1103/PhysRevD.14.1667.
- [26] L. Susskind. “Dynamics of spontaneous symmetry breaking in the Weinberg-Salam theory”. In: *Phys. Rev. D* 20 (10 Nov. 1979), pp. 2619–2625. DOI: 10.1103/PhysRevD.20.2619.
- [27] G. ’t Hooft. “Symmetry Breaking through Bell-Jackiw Anomalies”. In: *Phys. Rev. Lett.* 37 (1 July 1976), pp. 8–11. DOI: 10.1103/PhysRevLett.37.8.
- [28] G. ’t Hooft. “Computation of the quantum effects due to a four-dimensional pseudoparticle”. In: *Phys. Rev. D* 14 (12 Dec. 1976), pp. 3432–3450. DOI: 10.1103/PhysRevD.14.3432.

- [29] J. M. Pendlebury et al. “Revised experimental upper limit on the electric dipole moment of the neutron”. In: *Phys. Rev. D* 92.9 (2015), p. 092003. DOI: 10.1103/PhysRevD.92.092003. arXiv: 1509.04411 [hep-ex].
- [30] Varouzhan Baluni. “CP”. In: *Phys. Rev. D* 19 (7 Apr. 1979), pp. 2227–2230. DOI: 10.1103/PhysRevD.19.2227.
- [31] R. J. Crewther et al. “Chiral Estimate of the Electric Dipole Moment of the Neutron in Quantum Chromodynamics”. In: *Phys. Lett.* 88B (1979), p. 123. DOI: 10.1016/0370-2693(80)91025-4, 10.1016/0370-2693(79)90128-X.
- [32] G. ’t Hooft. “Naturalness, Chiral Symmetry, and Spontaneous Chiral Symmetry Breaking”. In: *Recent Developments in Gauge Theories*. Ed. by G. ’t Hooft et al. Boston, MA: Springer US, 1980, pp. 135–157. ISBN: 978-1-4684-7571-5. DOI: 10.1007/978-1-4684-7571-5_9.
- [33] R. D. Peccei and Helen R. Quinn. “CP”. In: *Phys. Rev. Lett.* 38 (25 June 1977), pp. 1440–1443. DOI: 10.1103/PhysRevLett.38.1440.
- [34] J. Wess and B. Zumino. “Supergauge Transformations in Four-Dimensions”. In: *Nucl. Phys.* B70 (1974), pp. 39–50. DOI: 10.1016/0550-3213(74)90355-1.
- [35] Abdus Salam and J. A. Strathdee. “Supergauge Transformations”. In: *Nucl. Phys.* B76 (1974), pp. 477–482. DOI: 10.1016/0550-3213(74)90537-9.
- [36] Lisa Randall and Raman Sundrum. “A Large mass hierarchy from a small extra dimension”. In: *Phys. Rev. Lett.* 83 (1999), pp. 3370–3373. DOI: 10.1103/PhysRevLett.83.3370. arXiv: hep-ph/9905221 [hep-ph].
- [37] R. D. Peccei and Helen R. Quinn. “Constraints imposed by CP conservation in the presence of pseudoparticles”. In: *Phys. Rev. D* 16 (6 Sept. 1977), pp. 1791–1797. DOI: 10.1103/PhysRevD.16.1791.
- [38] Jeffrey Goldstone, Abdus Salam, and Steven Weinberg. “Broken Symmetries”. In: *Phys. Rev.* 127 (3 Aug. 1962), pp. 965–970. DOI: 10.1103/PhysRev.127.965.
- [39] Gerard ’t Hooft. “Computation of the Quantum Effects Due to a Four-Dimensional Pseudoparticle”. In: *Phys. Rev. D* 14 (1976), pp. 3432–3450. DOI: 10.1103/PhysRevD.14.3432, 10.1103/PhysRevD.14.3432.
- [40] Steven Weinberg. “A New Light Boson?” In: *Phys. Rev. Lett.* 40 (4 Jan. 1978), pp. 223–226. DOI: 10.1103/PhysRevLett.40.223.
- [41] Frank Wilczek. “Problem of Strong p and t Invariance in the Presence of Instantons”. In: *Phys. Rev. Lett.* 40 (1978), pp. 279–282. DOI: 10.1103/PhysRevLett.40.279.
- [42] Y. Asano et al. “Search for a rare decay mode $K^+ \rightarrow \pi^+ \nu \bar{\nu}$ and axion”. In: *Physics Letters B* 107.1 (1981), pp. 159–162. ISSN: 0370-2693. DOI: http://dx.doi.org/10.1016/0370-2693(81)91172-2.
- [43] Michael Dine, Willy Fischler, and Mark Srednicki. “A simple solution to the strong CP problem with a harmless axion”. In: *Physics Letters B* 104.3 (1981), pp. 199–202. ISSN: 0370-2693. DOI: http://dx.doi.org/10.1016/0370-2693(81)90590-6.

- [44] Mikhail A. Shifman, A. I. Vainshtein, and Valentin I. Zakharov. “Can Confinement Ensure Natural CP Invariance of Strong Interactions?” In: *Nucl. Phys.* B166 (1980), pp. 493–506. DOI: 10.1016/0550-3213(80)90209-6.
- [45] A. Ringwald. “Axions and Axion-Like Particles”. In: *Proceedings, 49th Rencontres de Moriond on Electroweak Interactions and Unified Theories: La Thuile, Italy, March 15-22, 2014*. 2014, pp. 223–230. arXiv: 1407.0546 [hep-ph].
- [46] P. Sikivie. “Experimental Tests of the Invisible Axion”. In: *Phys. Rev. Lett.* 51 (1983). [Erratum: *Phys. Rev. Lett.* 52, 695 (1984)], pp. 1415–1417. DOI: 10.1103/PhysRevLett.51.1415, 10.1103/PhysRevLett.52.695.2.
- [47] A. A. Anselm. “Experimental test for axion \leftrightarrow photon oscillations in a homogeneous constant magnetic field”. In: *Phys. Rev. D* 37 (7 Apr. 1988), pp. 2001–2004. DOI: 10.1103/PhysRevD.37.2001.
- [48] K. Van Bibber et al. “Proposed experiment to produce and detect light pseudoscalars”. In: *Phys. Rev. Lett.* 59 (7 Aug. 1987), pp. 759–762. DOI: 10.1103/PhysRevLett.59.759.
- [49] Stephen J. Asztalos et al. “Experimental constraints on the axion dark matter halo density”. In: *Astrophys. J.* 571 (2002), pp. L27–L30. DOI: 10.1086/341130. arXiv: astro-ph/0104200 [astro-ph].
- [50] Paola Arias et al. “Optimizing Light-Shining-through-a-Wall Experiments for Axion and other WISP Searches”. In: *Phys. Rev. D* 82 (2010), p. 115018. DOI: 10.1103/PhysRevD.82.115018. arXiv: 1009.4875 [hep-ph].
- [51] F. Hoogeveen and T. Ziegenhagen. “Production and detection of light bosons using optical resonators”. In: *Nuclear Physics B* 358.1 (1991), pp. 3–26. ISSN: 0550-3213. DOI: http://dx.doi.org/10.1016/0550-3213(91)90528-6.
- [52] P. Sikivie, D. B. Tanner, and Karl van Bibber. “Resonantly Enhanced Axion-Photon Regeneration”. In: *Phys. Rev. Lett.* 98 (17 Apr. 2007), p. 172002. DOI: 10.1103/PhysRevLett.98.172002.
- [53] Reza Hodajerdi. “Production Cavity and Central Optics for a Light Shining through a Wall Experiment”. OA; Universität Hamburg, Diss., 2015. Dr. Hamburg: Universität Hamburg, 2015, p. 145. DOI: 10.3204/DESY-THESIS-2015-005.
- [54] Robin Bähre et al. “Any light particle search II — Technical Design Report”. In: *JINST* 8 (2013), T09001. DOI: 10.1088/1748-0221/8/09/T09001. arXiv: 1302.5647 [physics.ins-det].
- [55] Klaus Ehret et al. “New ALPS results on hidden-sector lightweights”. In: *Physics Letters B* 689.4–5 (2010), pp. 149–155. ISSN: 0370-2693. DOI: http://dx.doi.org/10.1016/j.physletb.2010.04.066.
- [56] Georg G. Raffelt. “Astrophysical axion bounds diminished by screening effects”. In: *Phys. Rev. D* 33 (4 Feb. 1986), pp. 897–909. DOI: 10.1103/PhysRevD.33.897.
- [57] S. Andriamonje et al. “An Improved limit on the axion-photon coupling from the CAST experiment”. In: *JCAP* 0704 (2007), p. 010. DOI: 10.1088/1475-7516/2007/04/010. arXiv: hep-ex/0702006 [hep-ex].

- [58] M Kuster et al. “The X-ray mirror telescope and the pn-CCD detector of CAST”. In: *Proc. SPIE* 5500 (2004), pp. 139–146.
- [59] P Abbon et al. “The Micromegas detector of the CAST experiment”. In: *New Journal of Physics* 9.6 (2007), p. 170.
- [60] M. et al. Arik. “New solar axion search using the CERN Axion Solar Telescope with ^4He filling”. In: *Phys. Rev. D* 92 (2 July 2015), p. 021101. DOI: 10.1103/PhysRevD.92.021101.
- [61] W. Heisenberg and H. Euler. “Folgerungen aus der Diracschen Theorie des Positrons”. In: *Zeitschrift für Physik* 98.11 (1936), pp. 714–732. ISSN: 0044-3328. DOI: 10.1007/BF01343663.
- [62] R. et al. Cameron. “Search for nearly massless, weakly coupled particles by optical techniques”. In: *Phys. Rev. D* 47 (9 May 1993), pp. 3707–3725. DOI: 10.1103/PhysRevD.47.3707.
- [63] E. et al. Zavattini. “New PVLAS results and limits on magnetically induced optical rotation and ellipticity in vacuum”. In: *Phys. Rev. D* 77 (3 Feb. 2008), p. 032006. DOI: 10.1103/PhysRevD.77.032006.
- [64] F Della Valle et al. “Measurements of vacuum magnetic birefringence using permanent dipole magnets: the PVLAS experiment”. In: *New Journal of Physics* 15.5 (2013).
- [65] Giovanni Cantatore. “Recent Results from the PVLAS Experiment on the Magnetized Vacuum”. In: *Axions: Theory, Cosmology, and Experimental Searches*. Ed. by Markus Kuster, Georg Raffelt, and Berta Beltrán. Berlin, Heidelberg: Springer Berlin Heidelberg, 2008, pp. 157–197. ISBN: 978-3-540-73518-2. DOI: 10.1007/978-3-540-73518-2_9.
- [66] F Della Valle et al. “First results from the new PVLAS apparatus: A new limit on vacuum magnetic birefringence”. In: *Phys. Rev. D* 90 (9 Nov. 2014), p. 092003. DOI: 10.1103/PhysRevD.90.092003.
- [67] Evalyn I. Gates, Geza Gyuk, and Michael S. Turner. “The Local Halo Density”. In: *The Astrophysical Journal Letters* 449.2 (1995), p. L123.
- [68] John Preskill, Mark B. Wise, and Frank Wilczek. “Cosmology of the Invisible Axion”. In: *Phys. Lett.* B120 (1983), pp. 127–132. DOI: 10.1016/0370-2693(83)90637-8.
- [69] L. F. Abbott and P. Sikivie. “A Cosmological Bound on the Invisible Axion”. In: *Phys. Lett.* B120 (1983), pp. 133–136. DOI: 10.1016/0370-2693(83)90638-X.
- [70] Michael Dine and Willy Fischler. “The Not So Harmless Axion”. In: *Phys. Lett.* B120 (1983), pp. 137–141. DOI: 10.1016/0370-2693(83)90639-1.
- [71] J. Hoskins et al. “Search for nonvirialized axionic dark matter”. In: *Phys. Rev. D* 84 (12 Dec. 2011), p. 121302. DOI: 10.1103/PhysRevD.84.121302.
- [72] S. J. Asztalos et al. “Improved rf cavity search for halo axions”. In: *Phys. Rev. D* 69 (1 Jan. 2004), p. 011101. DOI: 10.1103/PhysRevD.69.011101.
- [73] Jack W. Brockway, Eric D. Carlson, and Georg G. Raffelt. “SN1987A gamma-ray limits on the conversion of pseudoscalars”. In: *Phys. Lett.* B383 (1996), pp. 439–443. DOI: 10.1016/0370-2693(96)00778-2. arXiv: astro-ph/9605197 [astro-ph].

- [74] J. A. Grifols, E. Masso, and R. Toldra. “Gamma-rays from SN1987A due to pseudoscalar conversion”. In: *Phys. Rev. Lett.* 77 (1996), pp. 2372–2375. arXiv: astro-ph/9606028 [[astro-ph](#)].
- [75] Alexandre Payez et al. “Revisiting the SN1987A gamma-ray limit on ultralight axion-like particles”. In: *JCAP* 1502.02 (2015), p. 006. DOI: 10.1088/1475-7516/2015/02/006. arXiv: 1410.3747 [[astro-ph.HE](#)].
- [76] D. Horns and M. Meyer. “Indications for a pair-production anomaly from the propagation of VHE gamma-rays”. In: *JCAP* 1202 (2012), p. 033. DOI: 10.1088/1475-7516/2012/02/033. arXiv: 1201.4711 [[astro-ph.CO](#)].
- [77] Jonathan Biteau and David A. Williams. “The extragalactic background light, the Hubble constant, and anomalies: conclusions from 20 years of TeV gamma-ray observations”. In: *Astrophys. J.* 812.1 (2015), p. 60. DOI: 10.1088/0004-637X/812/1/60. arXiv: 1502.04166 [[astro-ph.CO](#)].
- [78] Adrian Ayala et al. “Revisiting the Bound on Axion-Photon Coupling from Globular Clusters”. In: *Phys. Rev. Lett.* 113 (19 Nov. 2014), p. 191302. DOI: 10.1103/PhysRevLett.113.191302.
- [79] P Pugnât et al. *OSQAR Status Report: Progress in the Photon Regeneration Experiment*. Tech. rep. CERN-SPSC-2010-036. SPSC-SR-074. Geneva: CERN, Nov. 2010.
- [80] Lyndon Evans and Philip Bryant. “LHC Machine”. In: *Journal of Instrumentation* 3.08 (2008), S08001.
- [81] P Pugnât et al. *Optical Search for QED vacuum magnetic birefringence, Axions and photon Regeneration*. Tech. rep. SPSC-P-331. CERN-SPSC-2006-035. revised version submitted on 2006-11-22 13:27:12. Geneva: CERN, Nov. 2006.
- [82] O Dunkel, P Legrand, and P Sievers. “A Warm Bore Anticryostat for Series Magnetic Measurements of LHC Superconducting Dipole and Short Straight Section Magnets”. In: *AIP Conf. Proc.* 710.LHC-Project-Report-685. CERN-LHC-Project-Report-685 (Jan. 2004), 494–504. 9 p.
- [83] The HDF Group. *Hierarchical Data Format, ver. 5*. <http://www.hdfgroup.org/HDF5/>. 1997-2017.
- [84] Giulio D. Agostini. *Bayesian Reasoning in Data Analysis: A Critical Introduction*. World Scientific Publishing Company, 2003.
- [85] Andrew Gelman et al. *Bayesian Data Analysis*. second. Chapman and Hall/CRC, 2003.
- [86] Dani Gamerman and Hedibert F. Lopes. *Markov Chain Monte Carlo: Stochastic Simulation for Bayesian Inference*. second. Chapman and Hall/CRC, 2006.
- [87] Anand Patil, David Huard, and Christopher Fonnesbeck. “PyMC: Bayesian Stochastic Modelling in Python”. In: *Journal of Statistical Software* 35.1 (2010), pp. 1–81. ISSN: 1548-7660. DOI: 10.18637/jss.v035.i04.
- [88] Miroslav Sulc et al. *OSQAR detection sensitivity*. Internal Communication. 2014.

- [89] R. Ballou et al. “New exclusion limits on scalar and pseudoscalar axionlike particles from light shining through a wall”. In: *Phys. Rev. D* 92.9 (2015), p. 092002. DOI: 10.1103/PhysRevD.92.092002. arXiv: 1506.08082 [hep-ex].
- [90] P Pugnât. *OSQAR Annual Report 2016*. Tech. rep. CERN-SPSC-2016-037. SPSC-SR-196. Geneva: CERN, Oct. 2016.
- [91] Dieter Trines. *Operating straightened HERA dipole magnets*. Internal Communication, ALPS II collaboration. 2013.
- [92] Eric D. Black. “An introduction to Pound–Drever–Hall laser frequency stabilization”. In: *American Journal of Physics* 69.1 (2001), pp. 79–87. DOI: 10.1119/1.1286663. eprint: <http://dx.doi.org/10.1119/1.1286663>.
- [93] Euan Morrison et al. “Automatic alignment of optical interferometers”. In: *Appl. Opt.* 33.22 (Aug. 1994), pp. 5041–5049. DOI: 10.1364/AO.33.005041.
- [94] Aaron D. Spector et al. “Characterization of optical systems for the ALPS II experiment”. In: *Opt. Express* 24.25 (Dec. 2016), pp. 29237–29245. DOI: 10.1364/OE.24.029237.
- [95] Bob Holdom. “Two U(1)’s and Epsilon Charge Shifts”. In: *Phys. Lett.* B166 (1986), pp. 196–198. DOI: 10.1016/0370-2693(86)91377-8.
- [96] S. A. Abel et al. “Kinetic Mixing of the Photon with Hidden U(1)s in String Phenomenology”. In: *JHEP* 07 (2008), p. 124. DOI: 10.1088/1126-6708/2008/07/124. arXiv: 0803.1449 [hep-ph].
- [97] Michele Cicoli et al. “Testing String Vacua in the Lab: From a Hidden CMB to Dark Forces in Flux Compactifications”. In: *JHEP* 07 (2011), p. 114. DOI: 10.1007/JHEP07(2011)114. arXiv: 1103.3705 [hep-th].
- [98] Jan Dreyling-Eschweiler. “A superconducting microcalorimeter for low-flux detection of near-infrared single photons”. PhD thesis. U. Hamburg, Dept. Phys., 2014. DOI: 10.3204/DESY-THESIS-2014-016.
- [99] G.C. Hilton K.D. Irwin. “Cryogenic Particle Detection”. In: first. Vol. 99. Topics in Applied Physics. Springer-Verlag Berlin Heidelberg, 2005. Chap. Transition-Edge Sensors.
- [100] J. Bardeen, L. N. Cooper, and J. R. Schrieffer. “Theory of Superconductivity”. In: *Phys. Rev.* 108 (5 Dec. 1957), pp. 1175–1204. DOI: 10.1103/PhysRev.108.1175.
- [101] H. Helmholtz. “Über einige Gesetze der Vertheilung elektrischer Ströme in körperlichen Leitern mit Anwendung auf die thierisch-elektrischen Versuche”. In: *Annalen der Physik und Chemie* 6.89 (1853), pp. 211–233.
- [102] R. C. Jaklevic et al. “Quantum Interference Effects in Josephson Tunneling”. In: *Phys. Rev. Lett.* 12 (7 Feb. 1964), pp. 159–160. DOI: 10.1103/PhysRevLett.12.159.
- [103] A. E. Lita et al. “Superconducting transition-edge sensors optimized for high-efficiency photon-number resolving detectors”. In: *SPIE*. Ed. by Mark A. Itzler and Joe C. Campbell. Vol. 7681. Apr. 2010. DOI: 10.1117/12.852221.
- [104] Aaron J. Miller et al. “Compact cryogenic self-aligning fiber-to-detector coupling with losses below one percent”. In: *Optics Express* 19.10 (May 2011), pp. 9102–9110. DOI: 10.1364/OE.19.009102.

- [105] D. Drung et al. “Highly sensitive and easy-to-use SQUID sensors”. In: *IEEE Transactions on Applied Superconductivity* 17.2 (2007), pp. 699–704. ISSN: 10518223. DOI: 10.1109/TASC.2007.897403.
- [106] Anders Smith et al. “Materials Challenges for High Performance Magnetocaloric Refrigeration Devices”. In: *Advanced Energy Materials* 2.11 (2012), pp. 1288–1318. ISSN: 1614-6840. DOI: 10.1002/aenm.201200167.
- [107] Bahaa E A Saleh and Malvin Carl Teich. *Fundamentals of photonics; 2nd ed.* Wiley series in pure and applied optics. New York, NY: Wiley, 2007.
- [108] J. A. Buck. *Fundamentals of Optical Fibers.* second. Wiley, May 2004.
- [109] A. E. Siegman, M. W. Sasnett, and T. F. Johnston. “Choice of clip levels for beam width measurements using knife-edge techniques”. In: *IEEE Journal of Quantum Electronics* 27.4 (Apr. 1991), pp. 1098–1104.
- [110] J. F. Bartlett et al. “The EPICS System: An Overview”. In: *FERMILAB-TM-1244.* 1984.
- [111] P Duval. “TINE: An integrated control system for HERA”. In: *Conference Proceedings C991004* (1999), pp. 526–528.
- [112] J. M. Chaize et al. “TANGO - an object oriented control system based on CORBA”. In: *Conf. Proc. C991004* (1999), pp. 475–479.
- [113] D. A. Edwards. *TESLA Test Facility Linac: Design report. Version 1.0, March 1, 1995.* 1995.
- [114] R. Abela et al. *XFEL: The European X-Ray Free-Electron Laser - Technical Design Report.* Hamburg: DESY, 2006. ISBN: 978-3-935702-17-1. DOI: 10.3204/DESY_06-097.
- [115] Bjarne Stroustrup. “What Is Object-Oriented Programming?” In: *IEEE Softw.* 5.3 (May 1988), pp. 10–20. ISSN: 0740-7459. DOI: 10.1109/52.2020.
- [116] DESY MCS4. *DOOCS Home Page.* Sept. 2016. URL: <http://tesla.desy.de/doocs/doocs.html>.
- [117] “IEEE Standard for Ethernet”. In: *IEEE Std 802.3-2012 (Revision to IEEE Std 802.3-2008)* (Dec. 2012), pp. 1–3747. DOI: 10.1109/IEEESTD.2012.6419735.
- [118] Ubuntu community Canonical Foundation. *Ubuntu.* Apr. 2017. URL: <https://www.ubuntu.com/>.
- [119] Mike Thompson and Peter Green. *Raspbian.* Apr. 2017. URL: <https://www.raspbian.org>.
- [120] Apple Inc. *macOS.* Apr. 2017. URL: <https://www.apple.com/macOS/>.
- [121] Oracle. *Solaris.* Apr. 2017. URL: <https://www.oracle.com/solaris/solaris11/index.html>.
- [122] Microsoft Corporation. *Microsoft Windows.* Apr. 2017. URL: <https://www.microsoft.com/de-de/windows>.
- [123] *Programmable Resolution 1-Wire Digital Thermometer.* Rev 4. 1/15. Maxim Integrated Products, Inc. 2015.

- [124] *Comparison of the DS18B20 and DS18S20 1-Wire® Digital Thermometers*. APPLICATION NOTE 4377. Maxim Integrated Products, Inc. Mar. 2009.
- [125] *Single-Channel 1-Wire Master*. Rev 10. 1/15. Maxim Integrated Products, Inc. 2015.
- [126] *HIH-5030/5031 Series Low Voltage Humidity Sensors*. Honeywell International, Inc. Mar. 2010.
- [127] Anthony Williams. *C++ Concurrency in Action: Practical Multithreading*. first. Manning Publications, Feb. 2012.
- [128] R. Brun and F. Rademakers. “ROOT: An object oriented data analysis framework”. In: *Nucl. Instrum. Meth.* A389 (1997), pp. 81–86. DOI: 10.1016/S0168-9002(97)00048-X.
- [129] William R. Leo. *Techniques for Nuclear and Particle Physics Experiments*. second. Springer-Verlag Berlin Heidelberg, 1994.
- [130] Intel Corporation. *Intel Xeon Processor E5-1620 v2*. May 2017. URL: https://ark.intel.com/de/products/75779/Intel-Xeon-Processor-E5-1620-v2-10M-Cache-3_70-GHz.
- [131] Matteo Frigo and Steven G. Johnson. “The Design and Implementation of FFTW3”. In: *Proceedings of the IEEE* 93.2 (2005). Special issue on “Program Generation, Optimization, and Platform Adaptation”, pp. 216–231.
- [132] W. R. Bennett. “Spectra of Quantized Signals”. In: *Bell System Technical Journal* 27.3 (1948), pp. 446–472. ISSN: 1538-7305. DOI: 10.1002/j.1538-7305.1948.tb01340.x.
- [133] Gerhard Heinzel et al. *Spectrum and spectral density estimation by the Discrete Fourier transform (DFT), including a comprehensive list of window functions and some new flat-top*. Tech. rep. 2002, pp. 1–84.
- [134] C. E. Shannon. “Communication in the Presence of Noise”. In: *Proc. Institute of Radio Engineers* 37.1 (1949), pp. 10–21.
- [135] P. Welch. “The use of fast Fourier transform for the estimation of power spectra: A method based on time averaging over short, modified periodograms”. In: *IEEE Transactions on Audio and Electroacoustics* 15.2 (June 1967), pp. 70–73. ISSN: 0018-9278. DOI: 10.1109/TAU.1967.1161901.
- [136] Makoto Matsumoto and Takuji Nishimura. “Mersenne Twister: A 623-dimensionally Equidistributed Uniform Pseudo-random Number Generator”. In: *ACM Trans. Model. Comput. Simul.* 8.1 (Jan. 1998), pp. 3–30. ISSN: 1049-3301. DOI: 10.1145/272991.272995.
- [137] Jan Dreyling-Eschweiler et al. “Characterization, 1064 nm photon signals and background events of a tungsten TES detector for the ALPS experiment”. In: *J. Mod. Opt.* 62.14 (2015), pp. 1132–1140. DOI: 10.1080/09500340.2015.1021723. arXiv: 1502.07878 [physics.ins-det].
- [138] F. James. “MINUIT Function Minimization and Error Analysis: Reference Manual Version 94.1”. In: (1994).

- [139] Klaus Zenker. *A filter bench in the cold*. ALPS II collaboration, Internal Communication. 2016.
- [140] Zachary Bush, Simon Barke, and Guido Mueller. *Double-demodulation Scheme ALPS-IIc Heterodyne Detector*. ALPS II collaboration meeting talk. 2017.
- [141] Axel Lindner, Benno Willke, and Herman Ten Kate. *Future options for searching axion-like particles through light-shining-through-a-wall experiments*. Physics Beyond Colliders Workshop. 2016.
- [142] E. Armengaud et al. “Conceptual Design of the International Axion Observatory (IAXO)”. In: *JINST* 9 (2014), T05002. DOI: 10.1088/1748-0221/9/05/T05002. arXiv: 1401.3233 [[physics.ins-det](#)].
- [143] Dieter Horns et al. “Searching for WISPy Cold Dark Matter with a Dish Antenna”. In: *JCAP* 1304 (2013), p. 016. DOI: 10.1088/1475-7516/2013/04/016. arXiv: 1212.2970 [[hep-ph](#)].
- [144] D. Budker et al. “Proposal for a Cosmic Axion Spin Precession Experiment (CASPEr)”. In: *Phys. Rev. X* 4.2 (2014), p. 021030. DOI: 10.1103/PhysRevX.4.021030. arXiv: 1306.6089 [[hep-ph](#)].
- [145] Peter Olver. *Introduction to Partial Differential Equations*. p. 182. Springer International Publishing, 2014.
- [146] Paul Wilmott. *The Mathematics of Financial Derivatives: A Student Introduction*. p. 137. Cambridge University Press, Nov. 1995.

Acknowledgements

Most of all, I would like to thank my beloved wife [REDACTED]: For your endless love and patience, for always raising me up when I grew desperate, for your infinite support and understanding, and especially, for always making me feel home when I traveled back to Mainz during the two years in Hamburg.

Undoubtedly, I like to thank my supervisor [REDACTED]: Thank you for your constant backing and encouraging advice. It was your confidence in me and my work together with your efficient ability to remove obstacles from the path, that has created a fruitful and motivating working atmosphere. Thank you a lot for all discussions, questions and guidance that helped me stay on track during this endeavour.

Special thanks to all present and past members of the Lichtenberg group in Mainz. I pretty much enjoyed all the time we spent together in the office, during coffee breaks, at Lasertag or Paintball, and of course on *every* Pizza-Friday. Due to your warmhearted and open attitude it was always fun for me to come to work.

No less thanks go to the members of the ALPS group at DESY. Thank you all for welcoming me, when I arrived in Hamburg and for making these two years a rewarding and mind broadening experience to me. In particular, I would like to thank [REDACTED] for his persistent supervision, guidance and his boundless optimism. Further, many thanks to [REDACTED], [REDACTED], [REDACTED] and [REDACTED] (actually from CMS, but almost ALPS member), for our precious discussions, effective teamwork, your always open doors, and all the fun we had.

I would especially like to thank [REDACTED] as he has introduced me to the exciting and beautiful universe of science. Thank you so much for your inspiring reports, for hiring me as research assistant (notwithstanding that I was not even an undergraduate student), and your unabated support that lasts till today.

Finally, I would like to say “Thank you” to my family; to my parents and grandparents, to my brothers and aunt. Thank you for supporting me in all my belongings, for your esteem and pride, even though you may had a hard time understanding what I was talking about.

To all of you, I would like to say

Live long and prosper!